

Flutter of a Wind Turbine Airfoil

A Parametric Study of High-Amplitude Limit Cycle Oscillations by means of Numerical Simulations

MASTER OF SCIENCE THESIS

For obtaining the degree of Master of Science in Engineering Wind
Energy at Technical University of Denmark and in Aerospace
Engineering at Delft University of Technology.

B.S. Lof

May 21, 2015

European Wind Energy Master - EWEM
DUWIND - Delft University of Technology
Risø - Denmark Technical University



Risø DTU



Copyright © B.S. Lof
All rights reserved.

EUROPEAN WIND ENERGY MASTER - EWEM
OF
ROTORDESIGN TRACK

The undersigned hereby certify that they have read and recommend to the European Wind Energy Master - EWEM for acceptance a thesis entitled **“Flutter of a Wind Turbine Airfoil”** by **B.S. Lof** in partial fulfillment of the requirements for the degree of **Master of Science**.

Dated: May 21, 2015

Professor: _____
prof.dr. G.J.W. van Bussel of Delft University of Technology

Supervisor: _____
dr. ir. A.H. van Zuijlen of Delft University of Technology

Supervisor: _____
dr.ir. M.H. Hansen of Denmark Technical University

Supervisor: _____
ir. R.S.W. Broers of XANT nv

Reader: _____
ir. T. Gillebaart of Delft University of Technology

Summary

In order to be more competitive with conventional, polluting energy resources, the levelised cost of energy (LCoE) of wind turbines has to decrease significantly [1]. A method to achieve this goal is to reduce the amount of parts in a wind turbine and more specifically avoid the use of expensive and failure-prone pitch systems. Using blades which passively deform under high aerodynamic loading and effectively reduce the peak, design-driving loads on the turbine structure might offer an interesting alternative to the pitch system. However, the conventional material for construction of blades, glass-fibre reinforced plastics, does not allow for such large deformations during normal operating conditions. Prior to this project, a study to incorporate more flexible materials has been carried out in the design of the current XANT-21 wind turbine in order to increase the flexibility of the blades. However, introducing a high degree of flexibility in the wind turbine blades might increase the risk of aeroelastic instabilities. These aeroelastic instabilities often result, in combination with a non-linearity in the aerodynamics or structure, in limit cycle oscillations (LCOs). The need to identify the key structural parameters which play a role in the initiation of the aeroelastic instabilities has led to the objective of this thesis:

Investigate the influence of the critical structural parameters on the onset velocity and the behaviour of high-amplitude limit cycle oscillations of a wind turbine airfoil by means of numerical simulations.

In order to study the effects of the critical structural parameters, two numerical models have been developed: an engineering model with the MATLAB software package [2] and a Reynolds Averaged Navier-Stokes (RANS) model within the OpenFOAM framework [3]. In the former, an aerodynamic solver is coupled with a structural solver. The aerodynamic part consists of the Risø dynamic stall model from Hansen [4] with an additional LEV contribution to the lift from Larsen et al. [5] and the structural solver consists of the equations of motion of a rigid 2D airfoil in two degrees of freedom. The latter numerically solves the unsteady, incompressible Navier-Stokes (NS) equations using a finite volume approach and performs fluid-structure interaction (FSI) simulations on a 2D airfoil.

In the validation of both numerical models, their capabilities to perform aeroelastic simulations on an airfoil in an efficient, accurate and stable fashion have been assessed. The engineering model was found to accurately reproduce the critical onset velocity at which LCOs are observed for the first time. The RANS model is capable of accurately obtaining the final pitch amplitude of the LCOs as compared to experimental data, while the capability of the engineering model to predict the final amplitude is highly sensitive to the structural damping coefficient. The RANS model has an improved capability of accurately describing the contribution of the leading edge vortex (LEV) which plays an important role in the non-linearities of the flow. When both models are assessed on their efficiency, the engineering model clearly is advantageous as a typical aeroelastic simulation is of the order 20 000 faster than the RANS model. For this reason, the engineering model was assessed to be the most suitable model to perform the parametric study on the wind turbine airfoil and was used in the investigation of the research objective.

The parametric study is performed on a wind turbine airfoil which is located at 75% blade radius of the XANT-21 wind turbine. The aeroelastic simulations with the engineering model on the current airfoil design yielded the result that classical flutter would occur at around 2 times the maximum operating relative wind speed. Afterwards, the aeroelastic analyses have been performed on four conceptual designs of the airfoil with varying structural properties. It was assessed that two designs, which replace the material of the skin with the new flexible material, are highly exposed to the risk of aeroelastic instabilities resulting in LCOs. These analyses have offered valuable insight in the critical structural parameters related to the onset of aeroelastic instabilities. A structured, parametric study has been carried out in order to quantify the effect of these critical structural parameters. The following parameters were found to play a significant role in the onset of aeroelastic instabilities: the torsional stiffness, the natural frequency ratio, which is the ratio between the heaving- and torsional natural frequency, and the location of the centre of gravity. The heave stiffness was found to be of minor importance. Introducing a structural angle of attack, thus artificially creating an airfoil operating close to or in stall, decreases the critical onset velocity significantly. The onset of the instabilities seen at higher structural angles is characterised as stall flutter and involves a different process of initiation than seen in classical flutter: no coalescence of the frequencies in two degrees of freedom is observed. Despite this difference in process of initiation, the critical structural parameters involved are similar for both types.

In order to limit the risk of initiation of aerodynamic instabilities potentially leading to high-amplitude LCOs in the design of an airfoil, it is recommended to limit the reduction of torsional stiffness to 25% of the wind turbine airfoil of the XANT-21 wind turbine without severely compromising the safety limit between operating wind speeds and critical wind speeds. In order to increase the aeroelastic stability of the airfoil, the location of the centre of gravity ought to be shifted as much as possible towards the leading edge. This can be done by increasing the mass of the spar caps or by adding mass to the leading edge.

Acknowledgements

This master thesis is the final milestone for obtaining my Aerospace Engineering degree from TU Delft and Wind Energy degree from DTU. It may be considered as a personal *Opus Magnus* in this regard, but many important, decisive years have served before as a preparation for this moment. Working on this master thesis so intensively for the past year, makes me almost forget all other experiences, knowledge and personal growth I have gained through my study period since 2007: Living in the Hague with my closest friends, playing football with the 1-0 Repers, postponing my holiday in order to take a resit for Space 1 in order to obtain my ‘Propedeuse’ in one year and obtain the four flight lessons as a reward, moving to Delft with the Balbotsboys, all the gymming-tanning-laundry activities, my Minor Economics & Business at the UvA, especially the happy-hours between classes were always an inspiring start of the week, doing my Master partially in Denmark which broadened my horizons and encouraged my travel aspirations, chucking wine in the Atmosfeer, the Wispo’s with ‘Kamer Paars’ which were life-bonding experiences and many more. All of these wonderful, challenging and instructive experiences, have led me to the brink of finally graduating.

The completion of my thesis, despite being a one man’s job, has not been possible without several people. I would like to thank all my supervisors, Thijs Gillebaart, Sander van Zuylen, Morten Hansen and Roland Broers, for their excellent guidance and expertise which greatly helped me in bringing this thesis to a successful end. The weekly or bi-weekly meetings with Thijs and Sander were always a great source of new insights and good spirit: when I sometimes thought I was completely lost, they helped me to draw a map and pointed me into the right direction. I hope that you both can continue to transfer your enthusiasm for the wonderful world of aerodynamics in the way you have been doing this to me. Thijs, thank you very much for all your time and effort you put into my project; especially by introducing OpenFOAM, creating the case-specific solvers, defining the project approach in the beginning, all difficulties and frustrations with validating the engineering model and dealing with some of my brain-failures. In the field of aerodynamics, I must acknowledge your superiority, however, in the football field this is likely to be the other way around (1-0 Repers > Flamingo’s & Vitesse > Ajax (for the past 3 years) ;)). Good luck with completing your doctorate and future

endeavours. I furthermore would like to express my thanks to all of my colleagues at XANT, in particular Roland who was always very eager to provide help on any kind of subject or part of my project. Working every day at a small wind turbine production company like XANT has been a very instructive and interesting experience and I wish XANT all the best and great success with your continued attempt to beating the Betz-limit and even greater breakthroughs. Furthermore I also want to acknowledge Morten for his inputs during our Skype-meetings and his expertise knowledge on the subject. Lastly, I would like to thank Prof. van Bussel for his time and advice in the final phase of my thesis.

On the non-academic side: my friends, I would like to thank my room-mates, the Wispo-boys, the VGB's, the Arnhemsche boys, the Aristoni and the rotor design bastards with whom I was able to spend my spare time and who forced me to take my mind off my thesis for an evening or a weekend. There have been a few people who deserve some special attention for their time, help, presence, motivational speeches and just simply being who they are. First of all, Lukas; your optimism, drive and enthusiasm have served as a great inspiration throughout the last year and the years before. Especially, helping to get my *off course* wind turbines back on track with all the fruitful conversations, brainstorm-sessions, out-of-the-box thinking and your thorough 'question-everything' attitude while checking my thesis. Thanks for keeping me reminded of the importance of celebrating the 'little victories' (especially in Supersonic ;)). Thank you, Twanne, for your help in checking spelling errors, your attempts to try to understand any of my frustrations/epiphanies during my thesis and especially for being there on Saturdays when even my task manager was not responding. Furthermore, the quotes on your poster really kept me motivated during my thesis and made the early rises out of bed definitely more bearable: *Success trains, failure complains*. I would like to thank Simon Reijniers for all the discussions regarding the bumps in the road during our theses and the amusing lunches in Brussels with a 'Lapino met een balleke'. I am sorry my friend, I have to recall the bet we made and it appears that you have lost. The perk of completing your thesis later than me, is that you can look forward to your free night of drinking beer! Thank you, Tom and Maarten, for respectively the coffee- and the beer breaks and both for your help and input!

Last but not least, I would like to express my gratitude to my girlfriend Esmeralda and my family. Esmeralda, you have always been a great source of creativity, love and passion. Thank you for your effort to memorise the title of my thesis, for your sincere interest in the subject and for all the support and sympathy during break-troughs and setbacks. Finally, my family: my parents Bert & Wieneke and my brother Sanne, who are like a warm, welcoming, compassionate bath in the oasis of calm in the east. Despite the fact that sometimes all of us were on a different continent, you have always managed to give me a very comforting feeling of support during my whole study. This continuous support has made me feel relaxed with all the decisions I have made over time. My family: *A pillar of stability ;)* [6].

Contents

Summary	v
Acknowledgements	vii
List of Figures	xvi
List of Tables	xvii
Nomenclature	xix
1 Introduction	1
1.1 Motivation	1
1.2 Research Questions	2
1.3 Thesis Outline	3
2 Research Introduction	5
2.1 Aeroelasticity	6
2.1.1 Definition of Aeroelasticity	6
2.1.2 Types of Aeroelasticity	6
2.1.3 Aeroelasticity of Wind Turbines	8
2.2 Aeroelastic Flutter	8
2.2.1 Classical Flutter	9
2.2.2 Stall Flutter	11
2.2.3 Limit Cycle Oscillations	15
2.3 Dynamic Stall	16
2.4 Methodology	18
2.4.1 Approach of the Project	19
2.4.2 Work Breakdown Structure of the Project	20

2.4.3	Structural Modelling of a 2D Airfoil	21
2.5	High-Amplitude LCO Experiments	22
2.5.1	Stall Flutter Experiment from Li [7]	22
2.5.2	Coalescence Flutter Experiment from Veilleux [8]	26
3	Engineering Model	29
3.1	Aerodynamic Part	29
3.2	Structural Part	33
3.3	Obtaining the Semi-Empirical Coefficients	34
3.4	Validation of the Aerodynamic Part	35
3.4.1	Prescribed Motion at $U_\infty = 3.9$ [m/s] - Decaying Case	35
3.4.2	Prescribed Motion at $U_\infty = 12.9$ [m/s] - Oscillating Case	37
3.4.3	Conclusions of Aerodynamic Validation	37
3.5	Validation of the Structural Part	38
3.5.1	Obtaining the unknown Structural Parameters	39
3.5.2	Comparison with Wind-off Experimental Results	41
3.5.3	Conclusions of the Structural Validation	43
3.6	Summary	44
4	RANS Model	45
4.1	Theory	45
4.1.1	Navier-Stokes Equations	46
4.1.2	Discretisation	46
4.1.3	Turbulence	48
4.1.4	Boundary Layer	52
4.2	Grid Convergence Study	54
4.2.1	Initial Cell Height Determination with y^+	54
4.2.2	Parameter Variation	54
4.2.3	Grid Convergence Results	55
4.3	Time Step Study	58
4.3.1	Time Step Study Set-up	58
4.3.2	Time Step Study Results	60
4.4	FSI Solver Set-up	61
4.5	Summary	63

5	Aeroelastic Simulations	65
5.1	Engineering- and RANS model Prescribed Motion Comparison	65
5.1.1	Prescribed Motion Results of Engineering Model	66
5.1.2	Prescribed Motion Results of RANS Model	68
5.2	Aeroelastic Results of NACA-0012 from Li [7]	71
5.2.1	Results with original Non-Linear Damping	71
5.2.2	Results with adapted Non-Linear Damping	74
5.2.3	Discussion	74
5.3	Aeroelastic Results of NACA-0012 from Veilleux [8]	75
5.3.1	Structural Parameters	76
5.3.2	Aeroelastic Results Comparison	76
5.3.3	Aeroelastic Responses over Time	79
5.3.4	Discussion	81
5.4	Summary	81
6	Parametric Study	85
6.1	The Wind Turbine Airfoil	86
6.2	Baseline Results	87
6.3	Conceptual Designs	88
6.3.1	Structural Design	89
6.3.2	Results of the Conceptual Designs	90
6.3.3	Discussion of the Results of the Conceptual Designs	91
6.4	Parametric Study	91
6.4.1	Effect of Pitch- and Heave Damping Coefficient	92
6.4.2	Varying the Pitch- and Heave Stiffness	92
6.4.3	Parametrisation of the Mass Distribution	93
6.4.4	Parametric Study of the Mass Distribution on Flutter Stability	94
6.5	Structural Angles of Attack Study	97
6.5.1	Results	97
6.5.2	Sensitivity Analysis of the Pitch- and Heave Stiffness	101
6.5.3	Sensitivity Analysis of the Mass Distribution	103
6.6	Summary	104
7	Conclusions & Recommendations	107
7.1	Conclusions	107
7.2	Recommendations	110
	References	113
A	Classical Flutter Analysis	119
B	Dynamic Experimental Motion and Force Coefficients for all Wind Speeds from Li [7].	123

C Sensitivity Analysis of the Viscous Lag Coefficient.	127
D Engineering Model Flowchart.	129
E OpenFOAM Algorithms	131
E.1 SIMPLE-algorithm	131
E.2 PISO-algorithm	132
E.3 PIMPLE-algorithm	132
F Parameters of the k-ω SST Turbulence Model	133
G RANS Time Step Study Results.	135

List of Figures

2.1	Research Introduction Flowchart.	5
2.2	Collar’s aeroelastic triangle from Collar [9].	6
2.3	Flutter Diagram of a typical Airfoil Section from Veilleux [8].	9
2.4	Airfoil Section subjected to a sudden Gust from Holierhoek [10].	12
2.5	Pitch Response Amplitudes versus Airspeed for several Static Angles of Attack from Razak et al. [11]	13
2.6	Qualitative Illustration of the development of LCOs. Veilleux [8]	16
2.7	Comparison of Steady-State and Dynamic Stall Lift Curve Characteristics from Amanullah Choudhry [12].	17
2.8	Flow Topologies around an Airfoil undergoing Dynamic Stall from Amanullah Choudhry [12]	18
2.9	Work Breakdown Structure of the Project	20
2.10	A Schematic Representation of a 2D Airfoil Section. Bichiou et al. [13]	21
2.11	Experimental Model mounted on the Flexible Support System from Li [7].	23
2.12	Static Lift-, Drag- and Moment Coefficients at $U_\infty = 13$ [m/s] and $U_\infty = 26$ [m/s] from Li [7].	24
2.13	Dynamic Pitch Angle and Lift- and Moment Coefficients at different Wind Speeds from Li [7].	25
2.14	Mean Amplitudes and Frequencies of LCOs for Different Wind Speeds from Experiment of Li [7].	25
2.15	Pitch- and Heave Amplitudes and Reduced Frequencies of LCOs as function of Reynolds number from Experiment of Poirel and Mendes, Veilleux [14, 15].	26
3.1	The trailing edge separation point, f^{st} , on a flat plate defined in a potential Kirchhoff flow. Hansen et al. [16]	31
3.2	Motion at $U_\infty = 3.9$ [m/s] for validation of the Semi-Empirical Model from Li [7].	36

3.3	Comparison of Lift- and Moment Coefficients at $U_\infty = 3.9$ [m/s] of Semi-Empirical Model and Experimental Results from Li [7].	36
3.4	Motion at $U_\infty = 12.9$ [m/s] for validation of the Semi-Empirical Dynamic Stall Model from Li [7].	37
3.5	Comparison of Lift- and Moment Coefficients at $U_\infty = 12.9$ [m/s] of Semi-Empirical Dynamic Stall Model and Experimental Results from Li [7].	38
3.6	Pitch- and Plunge Motion and Velocity Response at Wind-off Conditions of Spring 2 Configuration of Experimental Results from Li [7].	40
3.7	Damping- Ratios and Coefficients in Pitch and Heave of Spring 2 Configuration of Experimental Results from Li [7].	41
3.8	Wind-off Responses with Non-linear Damping compared to Experimental Response from Li [7].	42
4.1	Turbulent Boundary Layer. [17]	52
4.2	Boundary Layer Wall Treatment. [18]	52
4.3	Plots of a typical Steady-State Converged Case	55
4.4	Grid Convergence Study: Results	56
4.5	Richardson Extrapolation performed on the Results of the $n_a = 250$ Grids.	57
4.6	Simulation Time for the different Grids for $n_a = 250$	57
4.7	Mesh of the NACA-0012	58
4.8	Prescribed Motion at $U_\infty = 12.9$ [m/s] for Time Step Study compared with Experimental Motion from Li [7].	59
4.9	Time Step Study Results compared to Data from Li [7]	60
4.10	Flowchart of the FSI-Solver.	62
5.1	Force Coefficients Responses obtained with the Engineering- and RANS Model on a prescribed Motion compared with Experimental Data from Li [7].	66
5.2	Force Coefficients Contributions obtained with Engineering Model compared with Experimental Data from Li [7].	67
5.3	Dynamic TE Separation Contribution to the Lift Coefficient vs. Time.	68
5.4	Prescribed Motion Results obtained with the RANS Model at $U_\infty = 12.9$ [m/s].	70
5.5	Velocity Vector Plots on the Pressure, Velocity & Vorticity Fields at $t^* = 0.12$	70
5.6	Motion Response at $U_\infty = 0$ [m/s] obtained with Engineering- and RANS Model compared with Experimental Data from Li [7].	72
5.7	Motion Response and Force Coefficients at $U_\infty = 3.9$ [m/s] obtained with the Engineering- and RANS Model compared to Experimental Data from Li [7].	72
5.8	Motion Response and Force Coefficients at $U_\infty = 12.9$ [m/s] obtained with the Engineering- and RANS Model compared to Experimental Data from Li [7].	72
5.9	Motion Response and Force Coefficients at $U_\infty = 16.3$ [m/s] obtained with the Engineering- and RANS Model compared to Experimental Data from Li [7].	73

5.10	Motion Response and Force Coefficients of the Engineering Model with adapted Non-linear Damping compared to Experimental Data from Li [7].	75
5.11	Bifurcation Diagram and Frequencies for different Wind Speeds obtained with the Engineering Model with modified Non-linear Damping compared to Experimental Data from Li [7].	76
5.12	Pitch Amplitudes of LCOs obtained with Engineering- and RANS Model compared with Data from Thesis and Experiment from Veilleux [8].	78
5.13	Pitch- and Heave Motion Responses obtained with the Engineering- and RANS Model	79
5.14	Lift Coefficient Response obtained with the Engineering- and RANS Model at $Re = 70\,000$.	80
5.15	Lift Coefficients over Pitch Angle obtained with the RANS Model at Different Reynolds Numbers.	81
6.1	Airfoil Contours	86
6.2	Pitch- and Heave Amplitudes and Reduced Frequency of LCOs of the XANT Airfoil obtained with the Engineering Model at Three Different Initial Conditions.	87
6.3	Pitch- and Heave Frequency of the Decaying and Oscillating Cases versus Relative Wind Speed of the Baseline Airfoil.	88
6.4	Structural Overview of the XANT-21 Airfoil.	89
6.5	Pitch- and Heave Amplitudes and Reduced Frequency of LCOs of Conceptual Designs of the XANT Airfoil.	90
6.6	Contributions of different Terms in the Equations of Motion in Pitch- and Heave Direction at $U_{rel} = 87.5$ [m/s].	92
6.7	The Effect of varying the Pitch- and Heave Stiffness on the critical onset Velocity and Frequency Ratio.	93
6.8	Critical Onset Velocities for different Mass-Contributions.	95
6.9	Flutter Diagram for different Mass-Combinations at $k_{\theta} = 100\%$.	96
6.10	Flutter Diagram for different Mass-Combinations at $k_{\theta} = 75\%$.	96
6.11	Pitch- and Heave Amplitudes and Reduced Frequency of LCOs for different Structural Angles of Attack of the Baseline Airfoil.	98
6.12	Pitch- and Heave Motion, Force Coefficients and Dynamic Separation Point at $\theta_{geom} = 15^{\circ}$ and $U_{rel} = 50$ [m/s].	99
6.13	Pitch- and Heave Motion at the $U_{cr} = 87.5$ m/s of $\theta_{geom} = 5^{\circ}$	100
6.14	Pitch- and Heave Motion at the $U_{cr} = 55$ m/s of $\theta_{geom} = 15^{\circ}$	100
6.15	Pitch- and Heave Frequencies versus Wind Speeds at different θ_{geom}	101
6.16	Critical Onset Velocity for different Pitch- and Heave Stiffness at different Structural Angles of Attack.	102
6.17	Critical Onset Velocity for different Mass Distributions and varying Pitch- and Heave Stiffness at $\theta_{geom} = 12.5^{\circ}$.	103
B.1	Pitch Angle and Lift- and Moment Coefficients for all Wind Speeds from Li [7]	125
C.1	Sensitivity Analysis of the Viscous Lag Coefficient, T_f , on the prescribed Motion as explained in Section 3.3.	127

D.1	Flowchart of the Engineering Model	129
G.1	Instantaneous Time Step Study Results: Velocity, U	135
G.2	Instantaneous Time Step Study Results: Pressure, p	136
G.3	Instantaneous Time Step Study Results: Turbulent Kinetic Energy, k	136
G.4	Instantaneous Time Step Study Results: Turbulent Specific Dissipation, ω	137
G.5	Instantaneous Time Step Study Results: Turbulence Eddy Viscosity, ν_t	137

List of Tables

2.1	Experiment Structural Parameters from Li [7]	23
3.1	Semi-Empirical Parameters for a NACA 0012 Airfoil for different Mach Numbers from Bauchau [19]	35
3.2	Semi-Empirical Parameters of a NACA 0012 Airfoil at moderate Reynolds Numbers.	35
3.3	Two-term Exponential Fit Coefficients for the Damping Coefficients in Pitch and Heave.	41
3.4	Numerical and Theoretical Frequencies at Wind-Off Conditions compared to Experimental Observed Frequency from Li [7].	43
3.5	Experiment Structural Parameters from Li [7].	43
4.1	Key Parameters for Grid Convergence Study	54
4.2	Variation of Parameters in Grid Convergence Study	55
4.3	Final Mesh Set-up	57
4.4	Time Steps used in the Time Step Study	59
4.5	FSI Coupling Properties	62
5.1	Experiment Structural Parameters from Veilleux [8]	77
5.2	Simulation Time of the Engineering- and RANS model of 10 [s] Real Time Response.	78
6.1	Semi-Empirical Parameters of the XANT-21 Airfoil.	86
6.2	Structural Parameters of the XANT-21 Airfoil.	87
6.3	Percentual Difference of Structural Parameters of the Conceptual Designs with the Baseline XANT Airfoil.	90
6.4	Critical Onset Velocities of the Conceptual Designs compared to Baseline Design.	91
6.5	Effect of the Mass Contributions Changes on other Structural Parameters.	94

Nomenclature

Latin Symbols

A	Cross-sectional Area	$[m^2]$
a	Axial Induction Factor	$[-]$
a_h	Non-dimensional Distance from Airfoil Mid-chord to Elastic Axis	$[-]$
b	Airfoil Semi-chord	$[m]$
c	Airfoil Chord	$[m]$
C_d	Drag Coefficient	$[-]$
C_{DA}	Linear Aerodynamic Damping Coefficient	$[-]$
C'_d	Derivative of Drag Coefficient	$[-]$
C_E	Energy Transfer Coefficient	$[-]$
C_f	Skin Friction Coefficient	$[-]$
C_l	Lift Coefficient	$[-]$
C'_l	Derivative of Lift Coefficient	$[-]$
C_m	Moment Coefficient	$[-]$
C_{m0}	Static Moment Coefficient	$[-]$
C_N	Normal Coefficient	$[-]$
c_θ	Heaving Damping Coefficient	$[-]$
c_y	Heaving Damping Coefficient	$[-]$
Co	Courant Number	$[-]$
D	Domain Size of Mesh	$[c]$
dH	Initial Cell Height	$[m]$
dS	General Grid Point Spacing on Airfoil	$[m]$

ds	Grid Point Spacing towards L.E. and T.E. on Airfoil	$[m]$
e	Distance between Aerodynamic Centre and Rotational Center	$[m]$
\mathbf{F}	External Forces on the Fluid	$[N/m^3]$
f	Frequency	$[Hz]$
f^{st}	Steady Separation Point	$[-]$
f_v	Vortex Shedding Frequency	$[Hz]$
GR	Growth Rate of Mesh	$[-]$
I	Turbulence Intensity	$[-]$
k	Turbulent Kinetic Energy	$[m^2/s^2]$
k_r	Reduced Frequency	$[-]$
l	Non-dimensional Distance from the Center of Gravity to the Rotational Center	$[-]$
M	Mach Number	$[-]$
\mathbf{p}	Pressure	$[N/m^2]$
p_c	Grid Convergence Order	$[-]$
q	Dynamic Pressure	$[N/m^2]$
r_α	Radius of Gyration about the Elastic Axis	$[-]$
r_{fsi}	FSI Residual	$[-]$
Re	Reynolds Number	$[-]$
RF	Relaxation Factor	$[-]$
S	Static Imbalance	$[kgm]$
S_w	Wing's Surface	$[m^2]$
St	Strouhal Number	$[-]$
T	Period of Oscillation	$[s]$
t	Time	$[s]$
t^*	Non-Dimensional Time	$[-]$
U_{cr}	Critical Stall Flutter Speed	$[m/s]$
U_∞	Freestream Wind Velocity	$[m/s]$
U_{rel}	Relative Wind Velocity	$[m/s]$
u_τ	Friction Velocity	$[m/s]$
\mathbf{v}	Flow Velocity Vector	$[m/s]$
x_{cg}	Non-dimensional Distance from the Leading Edge to the Center of Gravity	$[-]$
x_{rc}	Non-dimensional Distance from the Leading Edge to the Center of Rotation	$[-]$
y^+	Dimensionless Wall Distance	$[-]$

Greek Symbols

α	Angle of Attack	$[^\circ]$
----------	-----------------	------------

α_d	Dynamic Angle of Attack	[°]
$\dot{\alpha}$	Derivative of Angle of Attack	[deg/s]
α_{init}	Initial Angle of Attack	[°]
α_m	Mean Angle of Attack	[°]
α_{ss}	Steady State Angle of Attack	[°]
α_0	Angle of Attack with Zero Lift Coefficient	[°]
β	Angle between the Direction of Vibration and y-axis	[°]
$\Delta\alpha$	Amplitude of Angle of Attack	[°]
ΔU_{cr}	Change in Critical Flutter Speed	[m/s]
ζ	Pitch Damping Ratio	[–]
μ	Airfoil/air Mass Ratio	[–]
ν	Kinematic Viscosity	[m ² /s]
ν_t	Turbulence Eddy Viscosity	[m ² /s]
ω	Specific Turbulence Dissipation	[1/s]
ω_θ	Pitching Natural Frequency	[Hz]
ω_h	Plunging Natural Frequency	[Hz]
$\bar{\omega}$	Natural Frequency Ratio	[–]
ϕ_m	Phase Angle between the Pitching Moment and the Motion	[rad]
ρ	Density	[kg/m ³]
θ	Pitch Angle	[°]

Subscripts

cr	Critical
div	Divergence
ff	Farfield Boundary Condition
max	Maximum
min	Minimum
NL	Non-Linear
w	Wall Boundary Condition

Abbreviations

ALE	Arbitrary Lagrangian Eulerian
AR	Aspect Ratio
BEM	Blade Element Momentum
CFD	Computational Fluid Dynamics

CV	Control Volume
DES	Detached Eddy Simulations
DNS	Direct Numerical Simulations
DOF	Degrees of Freedom
DVS	Dynamic Stall Vortex
FEM	Finite Element Model
FSI	Fluid Structure Interaction
FVM	Finite Volume Method
LCoE	Levelised Cost of Energy
LCOs	Limit Cycle Oscillations
LES	Large Eddy Simulations
LEV	Leading Edge Vortex
LE	Leading Edge
NACA	National Advisory Committee for Aeronautics
ODE	Ordinary Differential Equation
ONERA	Office National d'Etudes et de Recherches Aéropatiales
PISO	Pressure Implicit with Splitting of Operators
PIV	Particle Image Velocimetry
RANS	Reynolds Averaged Navier-Stokes
RPM	Rounds Per Minute
SIMPLE	Semi-Implicit Method for Pressure-Linked Equations
SIV	Stall-Induced Vibrations
SST	Shear Stress Transport
TEV	Trailing Edge Vortex
TE	Trailing Edge
UD	Uni-Directional

Chapter 1

Introduction

This introductory chapter provides the background of the thesis. Firstly, the motivation for the subject of the thesis and its relevance is discussed in Section 1.1. Secondly, Section 1.2 presents the objective of the thesis, defines the research questions and describes the tasks which have to be performed in order to complete the objective and find answers to the research questions. Lastly, a detailed overview of the structure of the report is given in Section 1.3.

1.1 Motivation

In the transition from the conventional energy resources, such as oil, coal and gas, to renewable resources, wind energy has become a clean and promising alternative. The levelised cost of energy (LCoE) of wind has greatly declined throughout years of research, development and experience in constructing, maintaining and exploiting wind turbines and wind farms according to [Lantz et al. \[20\]](#). Wind turbines with ever increasing diameters, aerodynamic tailoring, improved materials, better wind resource assessment and many other inventions have led to this significant decrease. However, the future of wind energy greatly depends on the ability and motivation of the government, industry and universities to continue to reduce costs and eventually achieve grid parity in a wide spectrum of context and locations. Thus, in order to become more competitive with traditional energy resources, it is of utmost importance to reduce the levelised cost of energy of wind.

One way to approach this is to reduce the amount of parts in a wind turbine without compromising the reliability nor the energy production of the wind turbine. For mid-size wind turbines that want to avoid the use of expensive and failure-prone pitch systems the ‘lure’ of compliant blades is a very attractive one: blades which passively deform due to the high aerodynamic loads and effectively reduce the peak, design-driving loads on the turbine structure. This passive deformation might be achieved by increasing the flexibility of the blade by using materials with different characteristics or alternative material lay-up. However, increasing the flexibility and modifying the material characteristics

and structure layup also leads to different aeroelastic behaviour of the blade. In order to ensure an efficient and reliable wind turbine design, great in-depth knowledge of the aeroelastic behaviour of the blades of the wind turbine in a variety of operating conditions should be acquired.

The field of aeroelasticity has been a topic of interest since even before the Wright brothers' first flight. In 1903, an attempt made by Professor Samuel P. Langley of the Smithsonian Institution to fly his monoplane resulted in a failure as described in [Bisplinghoff et al. \[21\]](#). His aircraft crashed into the Potomac River due to an aeroelastic event called wing torsional divergence. Initially, the study on aeroelasticity was mainly focussed on aircraft, but throughout the years it has become an important design parameter in a lot of devices and structures: such as bridges, transmission lines and of course wind turbines. The strong coupling between aerodynamics and structural dynamics may lead to aeroelastic instabilities such as flutter. Aeroelastic instability is becoming a critical issue in the design. With increasing rotor diameters and increased flexibility of the blades it might occur that under certain conditions the energy from the aerodynamics added to the system becomes so high that the blade can deform until failure.

In this thesis, the effect of creating a more flexible blade on the aeroelastic stability is studied. This is done by studying the onset of an aeroelastic instability of a 2D airfoil by means of a parametric study with two numerical models: an engineering model developed with the MATLAB software package [2] and a RANS model within the OpenFOAM framework [3]. The velocity at which an aeroelastic instability is observed is called the critical onset velocity. The engineering model implements a coupling between an aerodynamic part and a structural solver. The aerodynamic part consists of the Risø dynamic stall model from [Hansen \[4\]](#) with an additional LEV contribution to the lift from [Larsen et al. \[5\]](#) and the structural solver consists of the equations of motion of a rigid 2D airfoil in two degrees of freedom. The RANS model numerically solves the unsteady, incompressible Navier-Stokes equations using a finite volume approach and performs the aeroelastic stability analysis on a 2D airfoil by means of FSI simulations.

After both models are validated, a comparison is made in which their performances are assessed based on accuracy, efficiency and reliability. The most suitable model is chosen to perform the parametric study on the wind turbine airfoil from the XANT-21 wind turbine. A parametric space is defined and the effect of varying these structural parameters on the onset and response of the high-amplitude LCOs are investigated. The critical parameters are identified and recommendations on a range of structural parameters without the risk of self-excited LCOs are made.

1.2 Research Questions

This topic of the current study is related to the need to incorporate flexible blade in the design of the XANT-21 wind turbine in order to reduce the levelised cost of energy. The focus lies in studying the effect of using flexible blades on the aeroelastic stability. This

has lead to the following main objective of this thesis:

Investigate the influence of the critical structural parameters on the onset velocity and the behaviour of high-amplitude limit cycle oscillations of a wind turbine airfoil by means of numerical simulations.

Furthermore, the ability of different numerical methods to simulate the onset and process of flutter behaviour of an airfoil are investigated. These numerical methods include an engineering model which combines the Risø dynamic stall model with the structural equations of motion and RANS FSI simulations in OpenFOAM. In order to ensure a profound study on this subject, the following research questions are defined and are answered during the thesis:

1. *Which numerical models are able to predict the critical onset velocity and the behaviour of self-exciting high-amplitude limit cycle oscillations of an airfoil?*
2. *Which key parameters of a wind turbine airfoil affect the critical onset velocity leading to limit cycle oscillations?*
3. *How can the risk of self-exciting high-amplitude limit cycle oscillations of a wind turbine airfoil be reduced?*

The main objective of the thesis is divided in several tasks which are performed in order to provide answers to the research questions. These tasks are listed below:

1. Design a suitable engineering model including a dynamic stall model, which is able to numerically simulate aeroelastic behaviour of an airfoil.
2. Design a reliable, accurate and efficient RANS model in OpenFOAM which is able to numerically simulate aeroelastic behaviour of an airfoil.
3. Validate the models with experimental data of self-exciting high-amplitude limit cycle oscillations.
4. Compare the efficiency, reliability and accuracy of the numerical models.
5. Perform a parametric study on a wind turbine airfoil with the aim of identifying the critical parameters which affect the self-exciting high-amplitude limit cycle oscillations onset and response.

1.3 Thesis Outline

This section provides an overview of the steps taken to provide answers to the research questions in a structural way. The thesis consists of the following seven chapters:

- **Chapter 1:** Provides an introduction to and the motivation for the project and defines the thesis objective and research questions.
- **Chapter 2:** This chapter gives an overview of the state-of-the-art research in the field of aeroelasticity in wind turbines and explains the relevant theories and physical principles behind the most relevant aeroelastic instabilities for wind turbines. Based on the findings done in the research, the methodology for the thesis is developed and presented.
- **Chapter 3:** This chapter describes the aerodynamic- and structural part of the engineering model as well as their validation. Preliminary results are presented which offer some interesting insight in the ability of the model to predict the high-amplitude LCOs.
- **Chapter 4:** Firstly, the theories behind RANS simulations including turbulence and boundary layer are given in this chapter. Secondly, the method and results of the grid- and time independence study are presented in order to ensure a reliable and efficient simulation.
- **Chapter 5:** In this chapter, aeroelastic simulations are performed with the engineering- and RANS model and are validated with experimental data. The two models are compared and their ability to simulate the high-amplitude limit cycle oscillations in an accurate, reliable and efficient manner is discussed.
- **Chapter 6:** This chapter deals with the parametric investigation of the wind turbine airfoil. Several key parameters are varied and their influence on the onset and behaviour of the high-amplitude limit cycle oscillations are investigated.
- **Chapter 7:** The conclusions drawn during the study are summarised in this final chapter and the objective and research question are reviewed. Recommendations for further improvement or potential continuation of the study are offered as well.

Research Introduction

This chapter provides an introduction to the concepts and theories in the field of aeroelasticity of wind turbines. State of the art research regarding the numerical- and experimental study of aeroelasticity in general and aeroelasticity relevant for wind turbines are revised. This research will be used to justify the chosen methodology of the project. The chapter starts out with an introduction to the concept of aeroelasticity and how this is related to wind turbines in Section 2.1. In Section 2.2, a more detailed explanation of the aeroelastic instabilities relevant for wind turbines and their experimental- and numerical study in literature are presented. Section 2.3 describes the physical principles behind dynamic stall, which is an important non-linear aerodynamic phenomenon associated with aeroelastic instabilities and plays an essential role in the development of LCOs. The methodology of the project is described in Section 2.4. To conclude this chapter, the experiments from which the data is used for validation of the numerical models are discussed in Section 2.5. A graphical overview of the approach of this chapter is given in Figure 2.1.

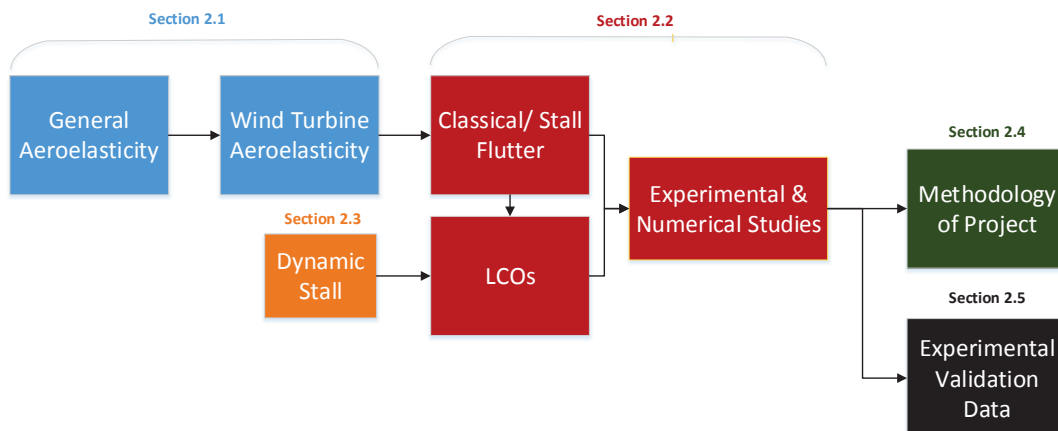


Figure 2.1: Research Introduction Flowchart.

2.1 Aeroelasticity

This first section starts out with a general definition of aeroelasticity in its widest sense. Afterwards, the different types of aeroelasticity are defined. To conclude this section, the types of aeroelasticity relevant for wind turbines are briefly discussed.

2.1.1 Definition of Aeroelasticity

The concept of aeroelasticity can be explained as the interaction between structural, aerodynamic and inertia forces. Aeroelasticity is defined by Bisplinghoff et al. [21] as:

"Aeroelasticity is the phenomena which exhibits appreciable reciprocal interactions (static or dynamic) between aerodynamic forces and the deformations induced in the structure."

Interaction of the forces means that a change of one force has an effect on the other. For example, a change in shape implies a change in the aerodynamic forces on it. In turn, the new aerodynamic forces impose a new structural deflection. This interacting feedback process may lead to 'flutter' which is a self-excited, potential destructive phenomenon, wherein energy is added from the airflow to the structure.

2.1.2 Types of Aeroelasticity

An important distinction to be made in aeroelasticity is between static and dynamic aeroelasticity. A clear overview of the relationship and interaction of aerodynamic, elastic and inertial forces has been created by Collar [9] in 1946 and is called the 'Aeroelastic Triangle' depicted in figure 2.2.

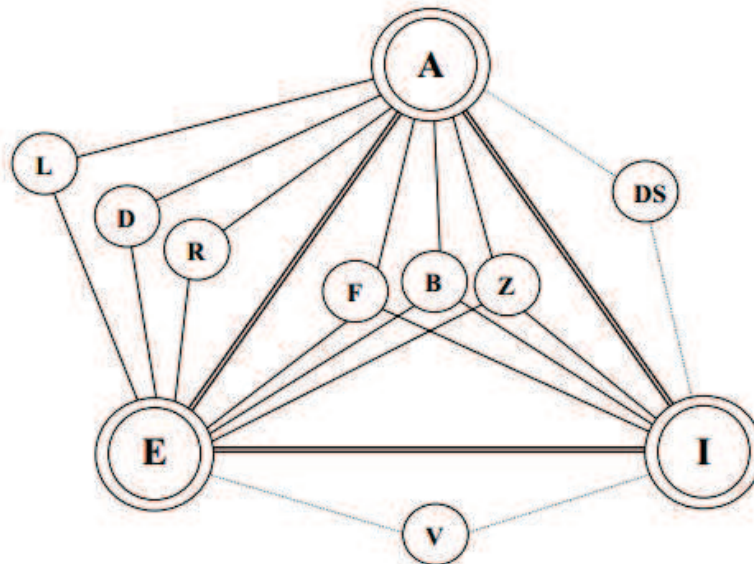


Figure 2.2: Collar's aeroelastic triangle from Collar [9].

The meaning of the three apexes are explained as:

- **A:** The aerodynamic forces
- **E:** The elastic forces
- **I:** The inertia forces

The meaning of the letters are explained as:

- **Dynamic Aeroelasticity:**

B - Buffeting. High-frequency, transient vibration caused by airflow separation or shock wave oscillations from one object striking another.

F - Flutter. Dynamic instability of an elastic structure caused by a positive feedback between a structure's deflection and the force exerted by the flow.

Z - Dynamic Response. Transient response of structural components produced by rapidly applied loads due to gusts, landing reactions, abrupt control motions and moving shock waves.

- **Static Aeroelasticity (Aerodynamic-Elastic Interaction):**

D - Divergence. A static instability of a lifting surface, at a speed called the divergence speed, where the lifting surface deflects under an aerodynamic load such that the applied load increases in turn increasing the twisting effect on the structure.

L - Load Distribution. Influence of elastic deformations of the structure on the distribution of aerodynamic pressures over the structure.

R - Control Reversal. At the control reversal speed, the intended effect of displacing a given component of the control system are completely nullified or opposite by elastic deformations of the structure.

- **Elastic-Inertia Interaction:**

V - Mechanical Vibrations. A periodic process of oscillations with respect to an equilibrium point.

- **Aerodynamic-Inertia Interaction:**

DS - Rigid-body Aerodynamic Stability. Represents flight dynamics.

Although the definition of the various aeroelastic types by means of connection of the vertices and solid lines, as seen in Figure 2.2, is widely accepted, in real life applications these precise limits are more difficult to define. Now the different types of aeroelastic behaviour have been identified and described, the relevant types observed in wind turbine applications are discussed.

2.1.3 Aeroelasticity of Wind Turbines

Aeroelasticity has become a critical design consideration for wind turbines due to longer, slender and more flexible blades. Several aerodynamic instabilities may arise during the normal- and extreme operating conditions of the wind turbine. Wind turbines have in general low structural damping which may become critical under certain operating conditions according to Hansen et al. [22]. What increases the complexity is the fact that the damping of composite structures varies with the ambient temperature and it degrades over time. A review of Hansen [4] postulates that two aeroelastic instabilities are most likely to occur for modern, commercial wind turbines: *stall-induced vibrations* and *classical flutter*, where the first is better known as *stall flutter*.

Both instabilities fall under the **F**-vertex in the Collar Diagram in Figure 2.2, which represents the aeroelastic flutter type, and thus are a result of the interaction between aerodynamic-, elastic- and inertia forces. The two types of instabilities are respectively linked to stall-regulated turbines and pitch-regulated, variable-speed turbines. The blades of stall-regulated turbines operate most of the time in separated flow conditions. The non-linear aerodynamic nature of separated flow can lead to negative aerodynamic damping. Pitch-regulated turbines do not operate in stall, so the risk of stall-induced vibrations is not very likely, however at standstill and around rated wind speeds for turbines with high-performance rotors operating close to stall it may occur. Classical flutter is a two dimensional instability where the coupling of flapwise- and torsional blade modes may lead to a diverging oscillating motion of the blade.

Bichiou et al. [13] states that flutter rarely has been associated with wind turbine blades, but that it is expected that with larger and more flexible blades it becomes more relevant. Great challenges lie ahead in modelling the coupled aerodynamic loads and structural responses in order to predict the aeroelastic response of wind turbine blades.

Now the relevant types of aeroelastic instabilities for wind turbines have been classified, a more elaborate explanation of the concerning instabilities, classical flutter and stall flutter, is done in the next section.

2.2 Aeroelastic Flutter

This section covers the two relevant types of aeroelastic instabilities for wind turbines, which are: classical flutter and stall flutter. At first, in Section 2.2.1, the necessary background to understand classical flutter as well as several methods to numerically predict classical flutter behaviour are given. Secondly, in Section 2.2.2, the aeroelastic phenomenon of stall flutter is described. Finally, Section 2.2.3 describes how the onset of these types of flutter can lead to limit cycle oscillations.

2.2.1 Classical Flutter

Classical flutter relies on the energy transfer from the flow to the structure by coupling of the flapwise- and torsional modes resulting in a rapid growth of the flapwise and torsional amplitudes of motion after an external perturbation of some kind [8, 23, 24, 25]. The loss of stability can be explained with the concept of aerodynamic damping. Increasing the freestream velocity, U_∞ , results initially in an increase of aerodynamic damping. At a certain U_∞ , the aerodynamic damping decreases until a U_{cr} is reached where the aerodynamic damping is equal to zero. Any increase in U_∞ will lead to a negative aerodynamic damping and means that with an external perturbation, the equilibrium position is disturbed and the aerodynamic forces are such that the motion is not damped. This often leads to structural failure.

An illustrative typical flutter diagram for an airfoil is shown in Figure 2.3. The imaginary part of p represents the frequency of the two modes and the real part of p represents the aerodynamic damping which are both a function of the freestream velocity. Flutter occurs in case of negative aerodynamic damping. As can be seen from the figure, the frequencies of both modes tend to merge as the critical flutter velocity is approached. That is why this type of flutter is often referred to as *coalescence flutter*.

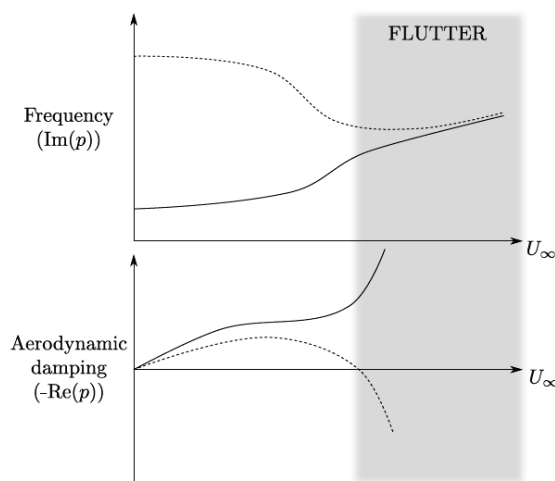


Figure 2.3: Flutter Diagram of a typical Airfoil Section from Veilleux [8].

The fact that classical flutter is usually restricted to an oscillatory instability observed in a potential flow as explained by Veilleux [8], implies that no non-linearities are apparent in the flow or at least do not play a significant role in the physical instability. One-degree-of-freedom classical flutter has been observed, although in general usage of the term *classical flutter* refers to a two-degree-of-freedom coupling as the phase shift of the motions are key parameters in the instability.

Determining Classical Flutter

As the classical flutter problem is a linear problem, the mechanism of this instability can be understood by following the explanation of Hansen [4] or the formulation from de Breuker [26]. This method to determine the linear classical flutter speed of a 2D airfoil with a steady aerodynamic model gives valuable insight in the mechanism behind the classical flutter phenomenon and is therefore further explained in Appendix A. However, it is based on a linear aerodynamic model and is therefore a too simple representation to accurately obtain the critical onset velocity for classical flutter for a 2D airfoil.

Other methods to determine the critical onset velocity for classical flutter, also known as the flutter point, use a more advanced representation for unsteady aerodynamics based on the Theodorsen's theory as described in Theodorsen [27]. These methods include the k method and the p - k method, which assume that only harmonic aerodynamic data is available and can predict the flutter points. Another method is the p method which is also able to predict the response of the airfoil, but is in practice less accurate in predicting the flutter point than the other methods. Their formulations can be found in de Breuker [26]. Politakis et al. [25] determines the flutter point by means of coupling a Blade Element Momentum (BEM) model to a 2D structural model. This proves to be a simple, yet effective method to obtain the flutter point and to gain in sight in the behaviour of the airfoil.

The previous methods apply for a 2D airfoil section, but classical flutter can also be determined on a complete wind turbine blade in 3D as has been done by Baran [24] and Lobitz [28]. Lobitz [28] determined the flutter limit of a large wind turbine blade using quasi-steady and unsteady aerodynamics and showed that the flutter point of the blade using quasi-steady aerodynamics was lower than the flutter point obtained with the unsteady aerodynamics. However, as this thesis focusses on performing a parametric study, it is not desired to perform the analysis in 3D as it would increase the modelling procedure and simulation time. So, the 3D study of flutter is disregarded during the remaining part of the thesis.

Characteristics of Classical Flutter

Following the observations made in Baran [24], Lobitz [28], Hansen [4] and Veilleux [8] about classical flutter, an overview of the characteristics and important parameters of this aeroelastic instability is given:

- Classical flutter is a result of negative aerodynamic damping where a torsional mode couples with a heaving mode through the aerodynamic forces.
- The concerning coupling of modes may lead to violent diverging oscillations in a classical flutter event.
- The flow over the airfoil must be attached, ($\frac{\delta C_l}{\delta \theta} > 0$), in order for classical flutter to occur.

- The static imbalance, $S = ml$, which is the mass of the airfoil multiplied with the distance between the centre of gravity and the rotational centre, is an important parameter in onset of flutter. When the centre of gravity lies ahead of the rotational centre, no flutter occurs. Increasing this parameter decreases the critical flutter speed, U_{cr} .
- The ratio of uncoupled natural frequencies, $\frac{\omega_h}{\omega_\theta}$, has a large impact on the onset of flutter. When these are close to one, merging of the frequencies happens faster and flutter occurs at lower velocities. This ratio is related to the following parameters: k_h , k_θ , m & I_{rc} as follows:

$$\frac{\omega_h}{\omega_\theta} = \frac{\sqrt{k_h/m}}{\sqrt{k_\theta/I_{rc}}} \quad (2.1)$$

where k_h and k_θ are respectively the stiffness in heave- and torsional direction and I_{rc} is the mass moment of inertia around the centre of rotation.

- Increasing the pitching- and heaving structural damping, c_θ and c_y , helps preventing or delaying the occurrence of flutter.
- The relative wind speed, U_{rel} , (which for wind turbines is the magnitude of the freestream velocity and rotational speed, $U_{rel} = \sqrt{U_\infty^2 + (r\Omega)^2}$) has to be high enough for flutter to occur. Where r [m] is the radial position of the airfoil on the wind turbine blade and Ω [rpm] is the angular velocity of the wind turbine blade.

2.2.2 Stall Flutter

Stall flutter may be experienced in a wide variety of applications - from venetian blind slats, air deflectors and automobile spoilers to helicopter rotors, turbomachinery blades and wind turbine blades. Stall flutter may occur during separation of the airflow around the structure at high angles of attack. Operating at high angles of attack may significantly reduce the critical flutter point as observed by [Halfman et al. \[29\]](#). It was first observed during World War I at which stall flutter occurred during sharp pull-up manoeuvres of aircrafts in combat.

The mechanism of stall flutter is clearly explained by [Holierhoek \[10\]](#). Stall flutter is a phenomenon that occurs when the flow separates from and reattaches to the surface of the wing in a cyclic manner. A gust increases the angle of attack, as shown in Figure 2.4, while the blade is operating in stall conditions. An increase in the angle of attack in the stall region will lead to a reduction of the aerodynamic forces acting on the airfoil. Assuming the aerodynamic centre is located in front of the elastic axis, the smaller forces will result in a nose down torsional deformation. This reduces the angle of attack which in turn, as it is still operating in stall, will increase the aerodynamic forces resulting in a cycle that may become unstable. For helicopters, this instability may occur during high speed flight and manoeuvring. Furthermore, this aerodynamic instability should be especially taken into account for stall controlled wind turbines which operate partially in stall

during high wind speeds. In practice this instability will result in a limit cycle oscillation in both wind turbines and helicopters due to the associated non-linear aerodynamics.

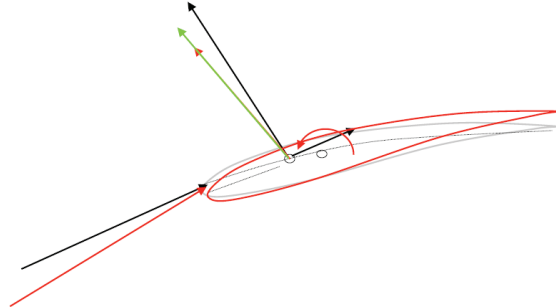


Figure 2.4: Airfoil Section subjected to a sudden Gust from Holierhoek [10].

Stall flutter may occur in partial or complete separation of the flow around an airfoil as stated by Dowell et al. [23]. In contrary to classical flutter, which is initiated in attached flow, the mechanism of energy transfer from the airflow to the oscillating airfoil does not rely on elastic and/or aerodynamic coupling between two modes, nor upon a phase lag between the aerodynamic forces and the airfoil's displacement. For these latter effects, the positive aerodynamic work added to a vibrating wing needs to operate in a linear system. For stall flutter, it is essential that the aerodynamic reaction to the motion of the airfoil/structure is non-linear and it may occur in a single degree of freedom. Some level of coupling between the two degrees-of-freedom as well as a phase lag between the motions may be apparent, but are not essential features of stall flutter. It is a self-excited and self-sustaining instability where fluctuating aerodynamic loads are created by an oscillating wing and these loads on their own maintain the oscillation by adding energy to the airfoil and thus often lead to self-sustained limit cycle oscillations. The fluctuating aerodynamic loads are characterised as the dynamic stall phenomenon which leads to the following definition of stall flutter as described by Li [7]:

Stall flutter is an aeroelastic phenomenon that emerges from an energy transfer between a fluid and an elastic system undergoing dynamic stall which may result in limit cycle- or diverging oscillations.

Determining Stall Flutter

Contrary to classical flutter, stall flutter can not be captured in a potential aerodynamic theory due to the non-linear characteristics involved within the concerning phenomenon. The theories on aeroelastic behaviour do not include non-linear force prediction in case of separation of the flow and thus are per definition not able to predict stall flutter as stated by Razak et al. [30]. This means that stall flutter has to be studied by numerical simulations or experimental studies. Numerical methods include solving the aerodynamics by means of Computational Fluid Dynamics (CFD) simulations or by means of the so-called semi-empirical dynamic stall models (such as the models described in Larsen et al., Hansen et al., Leishman and Beddoes, Tran and Petot [5, 16, 31, 32]). These

dynamic stall models provide a fast and efficient way of capturing the aerodynamics at hand. However, these models require semi-empirical, often airfoil-dependent, coefficients as an input which are usually obtained through experiments. Fluid-structure interaction simulations which includes coupling between the fluid mechanics and the structure would also provide the non-linear aerodynamics necessary for stall flutter prediction.

Experiments on a rectangular wing with a NACA 0018 profile with a plunge and pitch degree of freedom with the aim of investigating how stall flutter is generated and to determine its relationship to classical flutter have been performed by means of pressure-, acceleration and particle image velocimetry (PIV) measurements by Razak et al. [11]. The static angle of attack and the wind-tunnel airspeed were varied during the experiments and the Reynolds numbers ranged from 2.6×10^5 to 6.3×10^5 . The amplitude in pitch of the LCOs versus the airspeed for different mean angles of attack is displayed in Figure 2.5.

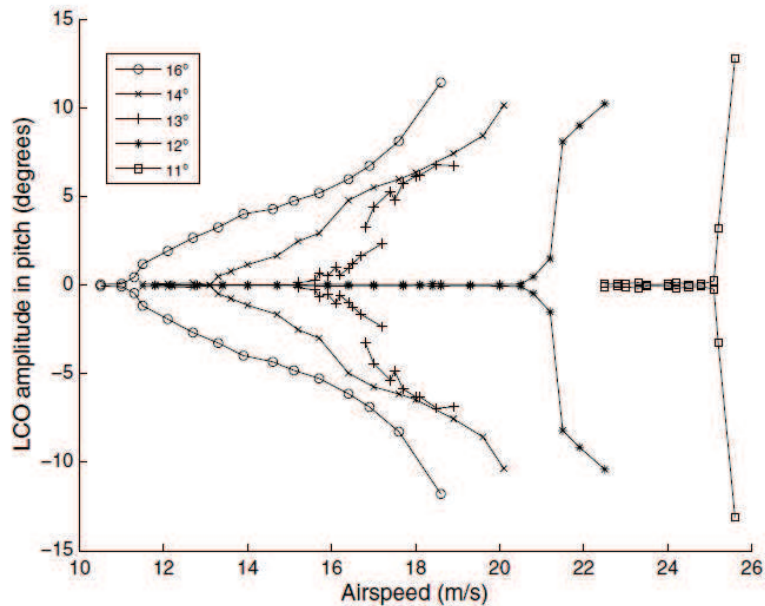


Figure 2.5: Pitch Response Amplitudes versus Airspeed for several Static Angles of Attack from Razak et al. [11]

The figure clearly shows a *bifurcation*, which is the intersection of two or more of a system's solution branches, in the responses. The intersection of a steady solution's branch with a branch of dynamic solutions is usually called a *Hopf bifurcation* which would be the correct term in this case. At a static angle of attack of 11° , a typical classical flutter event is shown: a steady response until, at a critical air speed, the pitch- and heave modes coalesce and the response becomes oscillatory with a rapidly growing amplitude. Beyond the critical airspeed, the amplitudes of the oscillations tend to grow in time. In the cases of an increase in angle of attack, the critical onset velocity becomes lower and post-critical behaviour is very different. The growth of the amplitude of the oscillations over an increasing air speed is slower. The frequencies in pitch and heave do not merge and the pitch frequency is observed to be the most dominant. These self-induced LCOs

with finite amplitude at higher mean angles of attack are classified to be due to stall flutter.

Self-sustained cyclic motions of limited amplitude of a wing caused by stall flutter have also been experimentally observed by Li, Razak et al., Arena et al. [7, 30, 33]. They concluded that the cyclic motion with limited amplitude was a result of non-linear behaviour of the aerodynamic forces on the structure and that this non-linearity was caused by periodic separation and reattachment of the flow. In the case of permanent separation of the flow, such as on a bluff body, the aerodynamic instability is called galloping as postulated in Dowell et al. [23]. The experiment performed by Li [7] will be covered more into detail in Section 2.5 as it was found to be a suitable validation case for the numerical models. The dynamic stall phenomenon, which is the main actor in stall flutter will be described in Section 2.3.

In 2002, Beedy et al. [34] performed a non-linear analysis of stall flutter with one of the aforementioned dynamic stall models: the ONERA-model from Tran and Petot [32]. Their goal was to explore the non-linear aerodynamics at high angle of attack stall flutter while attempting to develop a simple non-linear method of flutter analysis. They concluded that the flutter calculations were qualitative satisfactory in predicting the velocity and frequency of the onset of flutter of a NACA 0012. Other studies on stall flutter with the ONERA-model on a NACA 0012 have been performed by Sarkar and Bijl [35] and Sarkar et al. [36]. Studies on stall flutter who use different dynamic stall models include Galvanetto et al. [37], Shao et al. [38] and Li and Fleeter [39] where the first two use the *Beddoes-Leishman* model and the latter the *Gormont* model. Despite the fact that these studies had different objectives and methods in studying the stall flutter phenomenon, they clearly showed that the semi-empirical dynamic stall models are capable of numerically obtaining stall flutter onset and behaviour. The majority of these studies use the NACA 0012 airfoil as the subject of interest. No stall flutter studies on a wind turbine airfoil with one of the semi-empirical dynamic stall have been performed yet to the author's knowledge.

In 1989, Wu et al. [40] coupled a Navier-Stokes solver for 2D airfoils with a structural dynamic model. They predicted stall flutter and classical flutter of a NACA 0012 and a NACA 64A010 at a Reynolds number of $\sim 10^6$. Stall flutter was obtained at a mean incidence angle of 15° . For angles equal to and lower than 10° , no stall flutter was encountered at any airspeed. This study has been an important confirmation that it is possible to simulate the stall flutter phenomenon numerically with a Navier-Stokes solver.

In 2012, an attempt was made by Yabili et al. [41] to obtain similar stall flutter onset speeds numerically with *OpenFOAM* as the experimental results of the NACA 0012 from Li [7]. A solver was developed to compute large amplitude motion of two-dimensional rigid configurations. The $k-\omega$ SST turbulence model was applied. An O-topology domain with a 971×200 grid and a diameter of 60 times the chord was used. The lift- and moment coefficients over time are compared with the experimental data at an airspeed of $U_\infty = 13$ [m/s]. The results did not match exactly, however the trend, amplitude and frequency of oscillation are very well captured. The predicted amplitude at one airspeed was in very

good agreement with the experimental data. Unfortunately, they limited their study to only one particular airspeed. This study shows that it is possible to predict stall flutter behaviour by means of RANS simulations in *OpenFOAM*.

Summary of Stall Flutter

The several observations made by studying state-of-the-art research on the topic stall flutter results in a summarised overview of the particular aeroelastic instability. Stall flutter is a phenomenon where flow separation and reattachment to the surface of a wing occurs in a continuous cyclic manner. The non-linearities involved in the stall flutter phenomenon result in the fact that its initiation and response can not be captured by linear potential theory as seen in classical flutter. Therefore, stall flutter must be studied experimentally or by means of numerical simulations which can cope with non-linearities in the aerodynamics. Several experiments have been carried out through the years on stall flutter. However, this was mostly done on a NACA 0012 profile which in general has different aerodynamic characteristics compared to wind turbine airfoils. No experiments on stall flutter of a wind turbine profiled wing or blade has been performed yet. It has been shown by [Wu et al. \[40\]](#) that numerical simulations of stall flutter by means of CFD computations are possible and this would be a suitable approach to perform the parametric study on flutter behaviour of a wind turbine airfoil. A semi-empirical dynamic stall model, which captures the non-linearities in the aerodynamics, coupled with a structural solver would technically also provide a method of studying the stall flutter behaviour as seen previously in this section.

2.2.3 Limit Cycle Oscillations

After an airfoil is excited due to initiation of an aeroelastic instability, the resulting behaviour might lead to limit cycle oscillations. Limit cycle oscillations are self-sustained cyclic oscillations of a constant and limited amplitude according to [Li \[7\]](#). A qualitative illustration of a typical dynamically unstable system which, as a result of a perturbation, reaches a state of self-sustained LCOs is depicted in Figure 2.6. Initially, the system is at rest in a static equilibrium. At a certain point, the airfoil might be subjected to an aeroelastic instability, such as classical- or stall flutter, and the stable, neutral position of the airfoil is disturbed which results in an exponential growth in amplitude in the transient regime. With a growing amplitude, the effect of the non-linearities in the system becomes more significant and eventually limits the growth of the amplitude until a constant amplitude is reached and LCOs are observed. This is denoted by the LCO regime in the figure. As discussed before, these non-linearities may arise from large separations of the flow and are characterised by the dynamic stall phenomenon. Other non-linearities, such as non-linear material deformation or freeplay in control surfaces might also limit the exponential growth of a fluttering airfoil's amplitude of motion as stated by [Dowell et al. \[23\]](#) and [Arena et al. \[33\]](#).

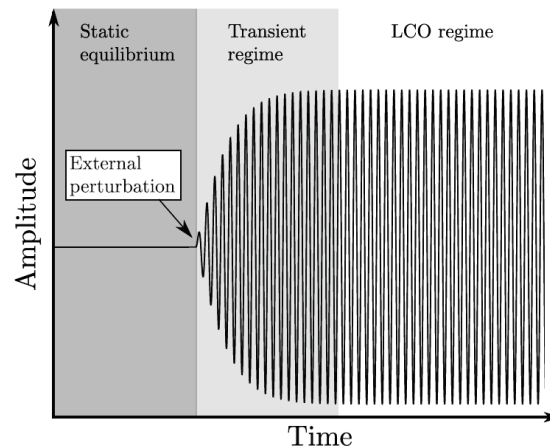


Figure 2.6: Qualitative Illustration of the development of LCOs. Veilleux [8]

The principles behind and methods of studying the two aeroelastic instabilities relevant for wind turbines and how this might lead to LCOs have been discussed in this section. The next section provides an in-depth explanation of an important phenomenon associated with the aeroelastic instabilities and LCOs: i.e. the dynamic stall phenomenon.

2.3 Dynamic Stall

A phenomenon which occurs when airfoils are subjected to pitching motions is a different stalling behaviour than stalling at fixed angles of attack: this is called dynamic stall. In dynamic stall, the shear layer near the leading edge rolls up to form a leading-edge vortex which provides additional suction over the upper airfoil surface as it convects downstream. After a temporary gain in lift and delay in stall, the LEV quickly becomes unstable and detaches from the airfoil. This detachment yields a dramatic decrease in lift and sudden increase in pitching moment which can lead to violent vibrations and dangerously high loads leading to fatigue and structural failure. The process of dynamic stall is depicted in Figure 2.7 and in Figure 2.8 obtained from Amanullah Choudhry [12] and can be summarised as follows:

1. At the onset of rotation, the lift produced at zero angle of attack is slightly higher for the unsteady case than during steady state operation. This is primarily due to the effects of a starting vortex that induces additional circulation near the airfoil leading edge.
2. As the angle of attack increases, the lift curve slope of the airfoil starts to decrease continuously and a slight curvature is observed in the so-called linear regime of the lift curve. This behaviour can be explained due to the apparent thickening of the boundary layer on the suction side of the airfoil. The thickening results from the passage of the starting vortex that leaves a region of reversed flow in its wake. However, due to the inertia of the fluid and low pressure zones, created by the motion of the airfoil, near the trailing edge (TE), the mean flow still follows the

contours of the airfoil. Hence, the thickening of the boundary layer results in the increase of apparent camber and apparent thickness of the airfoil. The combined effect results in the slight curvature of the lift curve.

3. A sudden plateau is observed in the lift curve that, to some extent, can be considered as partial flow separation. The plateau occurs after the starting vortex has merged with the trailing edge vortex. Due to the expansion between the trailing edge vortex and the airfoil, the regions of reversed flow near the trailing edge start to grow swiftly and the separation point steadily moves towards the leading edge of the airfoil. At the same time, a bubble region is formed near the leading edge. Instantaneously, the majority of the flow is separated from the airfoil surface and, therefore, the slight kink is observed.
4. With a further increase in the angle of attack, the lift curve slope is observed to increase. The increase in the lift slope is principally due to the formation of the LEV which appears when the reverse flow accumulation from the trailing edge finally forces the shear layer at the leading edge to be pushed away from the airfoil surface. This is the stage at which the primary leading edge vortex is observed which leads to the large increase of suction pressures on the surface of the airfoil.
5. Finally the maximum lift is achieved as the LEV convects to approximately the mid-chord of the airfoil. The maximum lift during the dynamic stall process can attain values up to 3 times the steady-state maximum lift coefficient. However, this substantial increase is also accompanied by an equivalent increase in the drag presumably due to the large angle.
6. Afterwards, a sudden drop in lift coefficient is observed and the airfoil goes into a state of deep stall. The resultant flow separation occurs due to the detachment of the LEV and was found to be more severe compared to the steady state case. The airfoil continues to generate lift beyond dynamic stall if pitching is continued. The post-stall lift characteristics during the airfoil rotation are still superior compared to the steady-state lift characters. The behaviour shows resemblance with the behaviour of a rotating flat plate. Therefore, a pitching airfoil during post stall behaves similarly to a pitching flat plate that exhibits a clear parabolic trend in the lift curve.

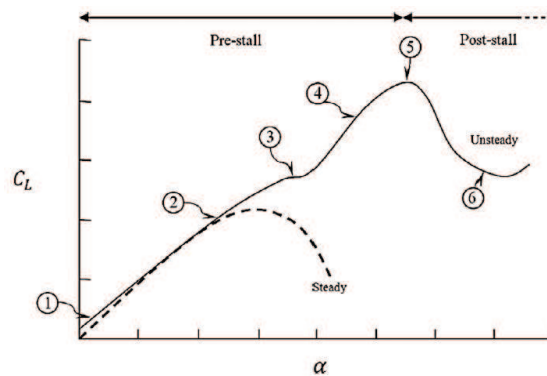


Figure 2.7: Comparison of Steady-State and Dynamic Stall Lift Curve Characteristics from Amanullah Choudhry [12].

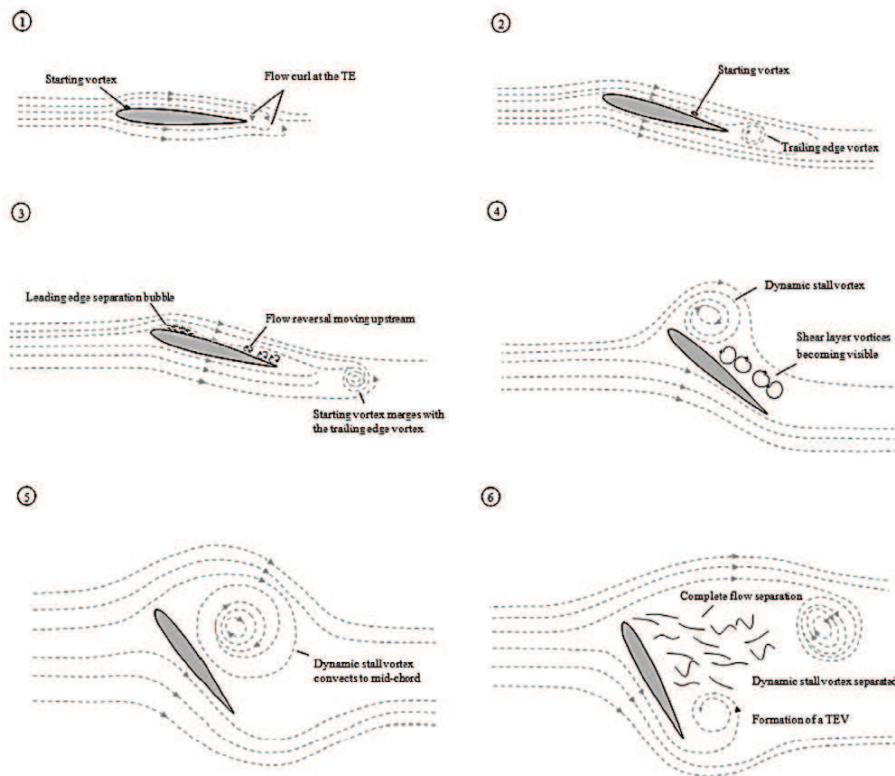


Figure 2.8: Flow Topologies around an Airfoil undergoing Dynamic Stall from Amanullah Choudhry [12]

This section has provided a qualitative description of the dynamic stall phenomenon observed with a rapid increasing angle of attack. The substantial effect of the creation and detachment of the LEV on the lift coefficient during a dynamically moving airfoil create the need to accurately describe this phenomenon with numerical models. Therefore, in studying the aeroelastic instabilities of a 2D airfoil, it is of utmost importance to use models who are capable of simulating the dynamic stall phenomenon and the associated force coefficients.

2.4 Methodology

This section discusses the methodology for the thesis investigation based upon the physical concepts and experimental studies discussed earlier. As seen in literature, two aeroelastic instabilities play a critical role in the design of wind turbine blades: classical- and stall flutter. As the XANT-21 wind turbine is a stall controlled wind turbine, it is believed that stall flutter is the most relevant aeroelastic instability type for the expected range of operating conditions. However, it is believed that studying the classical flutter phenomenon as well provides useful insights in the onset and behaviour of the aeroelastic instability. Increasing the flexibility of the XANT-21 wind turbine blades has an effect on the aeroelastic stability of the blades as critical structural parameters are modified in the new design. In order to study the effect of the critical structural parameters of a

wind turbine airfoil on the onset of such an aeroelastic instability and how this leads to high-amplitude limit cycle oscillations, a numerical model which is able to perform 2D non-linear aeroelastic simulations is required. As seen in the previous sections, the semi-empirical dynamic stall models as well as Navier-Stokes solvers coupled with a structural solver are able to deal with these kind of simulations. In this project, aeroelastic simulations with both models are performed as their capabilities have not often been assessed and evaluated at high-amplitude limited cycle oscillations. This section is divided in three subsections: first the approach of the project is given, afterwards a work breakdown structure of the project is discussed and lastly the structural modelling of a 2D airfoil used by both numerical models are presented.

2.4.1 Approach of the Project

Two numerical models are used in the aeroelastic simulations of a 2D airfoil: an engineering model which uses one of the aforementioned semi-empirical dynamic stall models and a RANS model. Selecting a suitable dynamic stall model depends on the type of airfoil to be studied, the semi-empirical coefficients publicly available, the accuracy and the ease of implementation of the models. [Larsen et al. \[5\]](#) provides a comparison of several dynamic stall models and concludes that only their model, the Risø model and the Beddoes-Leishman model are capable of accurately reproducing experimental results at fully attached flow as well as in the stall regime. The Beddoes-Leishman model, however, needs twelve coefficients as an input compared to respectively seven and six of the first two models. It is decided to use the semi-empirical dynamic stall model from [Hansen et al. \[16\]](#) to calculate the transient aerodynamic forces in the engineering model. This model has proven to be a simple, yet accurate model in predicting the forces in dynamic stall of especially wind turbine airfoils. The Risø dynamic stall model is covered into more detail in Section 3.1. The other numerical model is a RANS solver which is coupled with a structural solver within OpenFOAM. The main reasons to perform the simulations in OpenFOAM are that OpenFOAM is open source software (so no expensive licenses are required), knowledge about OpenFOAM is abundant within TU Delft and solvers can be modified to fit case specific requirements.

In order to ensure that the numerical models are capable to accurately and efficiently obtain the onset of aeroelastic instabilities and the behaviour of high-amplitude limit cycle oscillations, they have to be validated. This is done by comparison of their capabilities with data from experiments. Two experiments have been selected as suitable datasets to validate the models with: the stall flutter experiment from [Li \[7\]](#) and a classical (or also referred to as coalescence) flutter experiment described in [Veilleux \[8\]](#). The experimental set-up and results are elaborated upon in the Section 2.5. Especially, the stall flutter experiment provides valuable data about the force coefficients on high-amplitude cyclic motions. However, the aeroelastic behaviour in this experiment, in hindsight, proved to be difficult to reproduce due to the uncertainty in and lack of known structural parameters. The data presented in [Veilleux \[8\]](#) is used to validate the aeroelastic simulations of the two models.

After both models are validated, a comparison is made in which their performances are assessed based on accuracy, efficiency and reliability. The most suitable model is chosen to perform the parametric study on the wind turbine airfoil from the XANT-21 wind turbine. A parametric space is defined and the effect of varying these structural parameters on the onset and response of the high-amplitude limit cycle oscillations are investigated. The critical parameters are identified and recommendations on a range of structural parameters without the risk of self-excited LCOs are made.

2.4.2 Work Breakdown Structure of the Project

An overview of the tasks performed to complete the thesis is shown in a work breakdown structure shown in Figure 2.9. The work breakdown structure shows six columns, which correspond chronologically to Chapter 2 to Chapter 7. The first column focusses on the available literature, attempts to provide insight in the physics at play and the project approach is designed here. The second column deals with the design and validation of the engineering model. The third column show the work done in order to obtain a suitable and reliable RANS model. In the fourth column, the main task is to assess the capabilities of the engineering- and the RANS model and provide a comparison. The fifth column describes the tasks performed for the parametric aeroelastic study on the wind turbine airfoil and is related to the main objective of this thesis. The last column consists of drawing conclusions and provide recommendations for further improvement or continuation of the research.

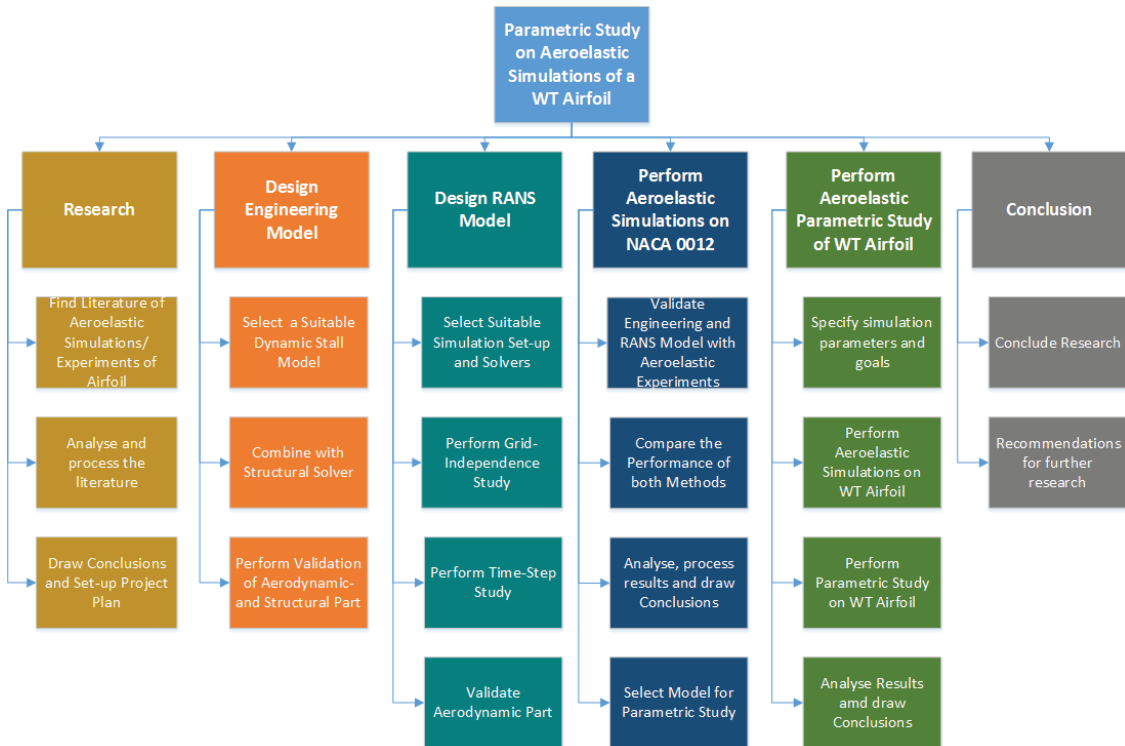


Figure 2.9: Work Breakdown Structure of the Project

2.4.3 Structural Modelling of a 2D Airfoil

The wind turbine blade is simplified and modelled as a 2D cross section as shown in Figure 2.10. The airfoil is free to move in two degrees-of-freedom; pitch around the z -axis and heave along the y -axis. Motions in other directions or around any other axis is not possible. The airfoil is free to rotate around the rotational centre, x_{rc} , and the heaving motion is applied at this specific location as well. Two artificial springs in the two degrees of motion are attached to the rotational centre with the following properties: stiffness and damping coefficient. The centre of gravity of the airfoil is located at x_{cg} . It is assumed that the lift and moment on the airfoil act in the aerodynamic centre (assumed to be equal to the centre of pressure) which is located at quarter-chord position.

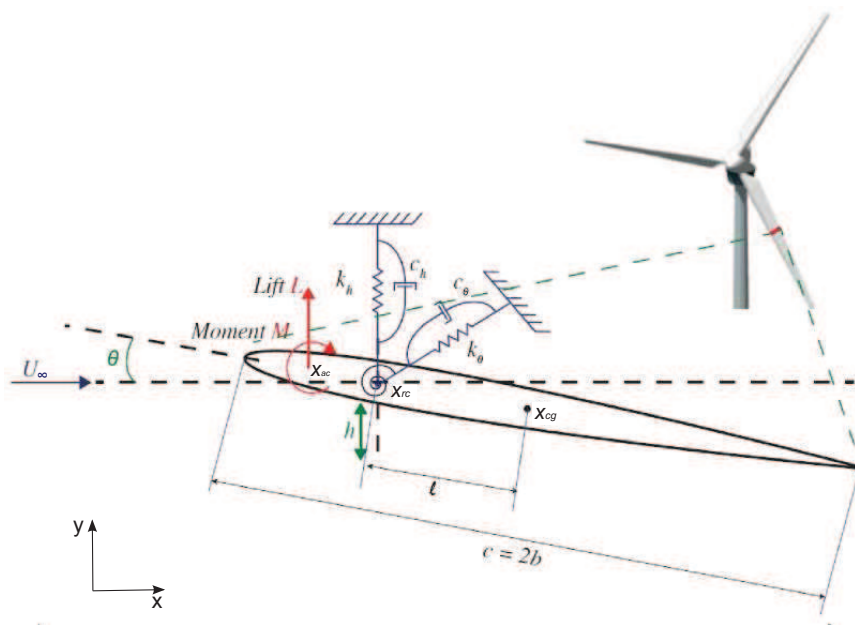


Figure 2.10: A Schematic Representation of a 2D Airfoil Section. *Bichiou et al. [13]*

The figure also points out the parameters of interest in the formulation of the aeroelastic problem. These are declared here:

- U_∞ : Free-stream velocity
- c : Airfoil's Chord Length
- θ : Pitch Angle
- h : Heave Displacement
- M : Moment around Aerodynamic Center
- L : Lift of Airfoil
- x_{ac} : Location at which the forces act (assumed quarter-chord)

- x_{rc} : Location of Center of Rotation (assumed to be equal to the elastic axis)
- x_{cg} : Location of the Center of Gravity
- l : Distance between Center of Rotation and Center of Gravity
- c_h : Damping Coefficient in Heave Direction
- c_θ : Damping Coefficient in Pitch Direction
- k_h : Stiffness in Heave Direction
- k_θ : Stiffness in Pitch Direction

Summation of the forces and moments exerted on the airfoil lead to the general equations of motion. The equations of motion of the airfoil in two directions are then:

$$m\ddot{h} + S\ddot{\theta} + c_h\dot{h} + k_h h = -L \quad (2.2)$$

$$S\ddot{h} + I_{rc}\ddot{\theta} + c_\theta\dot{\theta} + k_\theta\theta = M \quad (2.3)$$

where $S = ml \cos \theta$ is the static mass moment.

2.5 High-Amplitude LCO Experiments

This section describes the set-up and the results of the two experiments of which the data is used to validate the numerical models with. At first, the stall flutter experiment from Li [7] is described. Secondly, the coalescence flutter experiment from Veilleux [8] is discussed.

2.5.1 Stall Flutter Experiment from Li [7]

In this section, the stall flutter experiment carried out by Li [7] which is used to validate the engineering- and the RANS model. The experiment in Li [7] aimed to investigate the stall flutter phenomenon by studying the free motion in pitch and plunge direction and especially the onset and development of self-excited stall flutter oscillations of a rectangular wing with a NACA 0012 profile. The free-stream wind velocity was varied from $U_\infty = 0$ [m/s] up to $U_\infty = 30.7$ which corresponds to a range of Reynolds number from $Re = 0$ to $Re = 630\,000$ and Mach-numbers $M = 0$ to $M = 0.088$ (obtained with $M = \frac{U_\infty}{a}$, where it is assumed that the speed of sound at standard atmosphere temperature $a = 343.6$ [m/s] as shown by Dean [42])

First, the experimental set-up and the static tests results are described in this section. Secondly, the results of the dynamic tests of the pitch-plunge wing are presented and discussed.

Experiment Design

The experiments were carried out in two different wind tunnels, one for the static tests and the other for the dynamic tests, in the Goldstein Laboratory of the University of Manchester, at Barton Aerodrome. A graphical overview of the experimental model is given in Figure 2.11. The experimental apparatus consists of the wing, the support mechanisms, which includes the bearings, springs and rods, and pressure sensors.

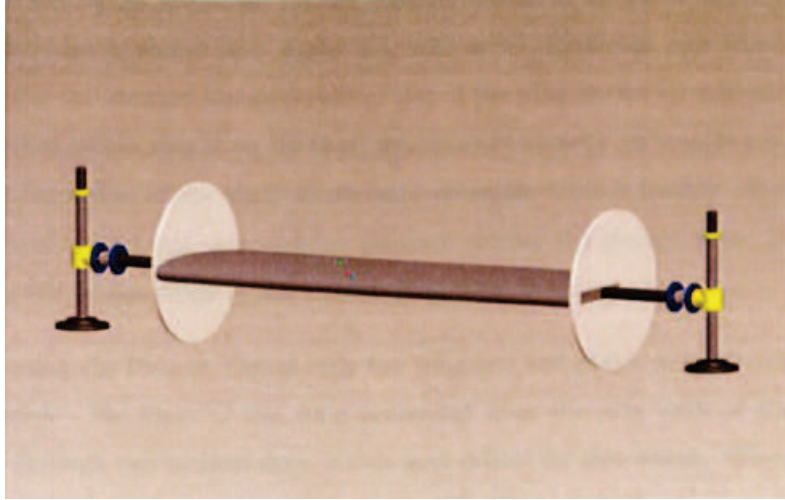


Figure 2.11: Experimental Model mounted on the Flexible Support System from Li [7].

The wing is a rectangular wing with a NACA 0012 profile with 900 [mm] span, 300 [mm] chord which means an aspect ratio (AR) of 3 [-]. The support mechanism was designed such to allow free motion of the wing in pitch and plunge direction. By using two pairs of compression springs and a pair of torsion springs, the restoring force is provided and the structural stiffness is given. The stiffness of the torsional springs were chosen such that the wing would undergo static divergence at airspeeds around 20 [m/s]. Bearings and bushes were used in order to minimise friction. An overview of the relevant experimental parameters is given in Table 2.1.

Table 2.1: Experiment Structural Parameters from Li [7]

Parameter	Symbol	Unit	Value
Chord	c	[m]	0.3
Span	S	[m]	0.9
Total Torsional Spring Stiffness	k_{θ}	[Nm/rad]	13.07
Total Compression Spring Stiffness	k_y	[N/m]	18 976
Centre of Rotation	x_{RC}	[%]	38.33
Moment of Inertia around the Centre of Rotation	I_{RC}	[kg · m ²]	0.31
Mass	M	[kg/m]	16.67

Two different sensors were used in the experiment; one to obtain the aerodynamic forces and another to obtain the displacement and rotation. A piezoresistive pressure sensor

is used to measure the pressure distribution, from which the aerodynamic forces are deduced, with 18 pressure taps located around the middle section of the wing and a laser displacement sensor measured the pitch and plunge displacement.

Initially, static tests were performed in order to obtain the static aerodynamic lift, drag and moment and the corresponding coefficients for range of incidence angles of attack from -39° to 39° . Static experiments were carried out for 21 different velocities ranging from $U_\infty = 7$ [m/s] to $U_\infty = 27$ m/s. For this thesis study data is only available at 6 different wind speeds (13,14,15,16,25 and 26) from which two wind speeds, determined by their reliability and scope, are chosen and the corresponding lift-, drag- and moment coefficients are shown in Figure 2.12.

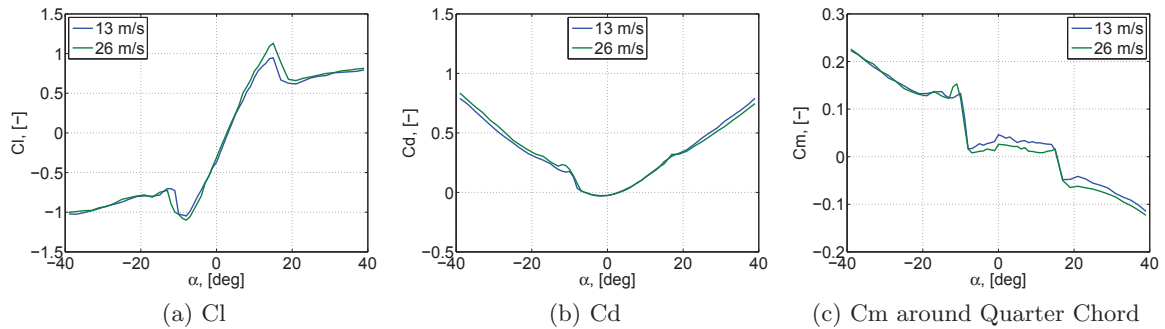


Figure 2.12: Static Lift-, Drag- and Moment Coefficients at $U_\infty = 13$ [m/s] and $U_\infty = 26$ [m/s] from Li [7].

The asymmetry in the force coefficient graphs clearly shows that the constructed wing does not have the exact contour of a symmetric NACA 0012 profile. The procedure of obtaining the shape of the wing by folding a metal sheet around several ribs resulted in an asymmetric profiled wing. Discrepancies with other static experimental data on the NACA 0012 have been observed as well by Li [7].

Dynamic Test Results

This section describes the dynamic test results of the pitching and plunging wing from the experiment. An initial excitation in the form of a hand-administered moment around the pitch axis intended to rotate the wing far beyond angles of stall was given if needed. The measurement of the position and pressure responses always start simultaneously. The available data from the experiment represents the dynamic results of using configuration 'Spring 2' for the compression springs. Several representable wind speeds (3.9, 9.3 and 11.1 m/s) are chosen and the dynamic responses are displayed in Figure 2.13.

From the figures it can be seen that the excitation impulse is not equal for the different wind speeds as it was hand-administered. At $U_\infty = 3.9$ [m/s], the response is damped and decays to equilibrium position. However at $U_\infty = 9.3$ [m/s], the excitation results in the wing performing limit cycle oscillations of amplitudes of 40° in pitch. The amplitude in plunge is very low (around 5 cm) when LCOs occur and the plunge natural frequency is not excited at all due to the high stiffness in plunge. The response of the wing is single-modes, despite the two degrees of freedom of the system. At $U_\infty = 11.1$ [m/s], no

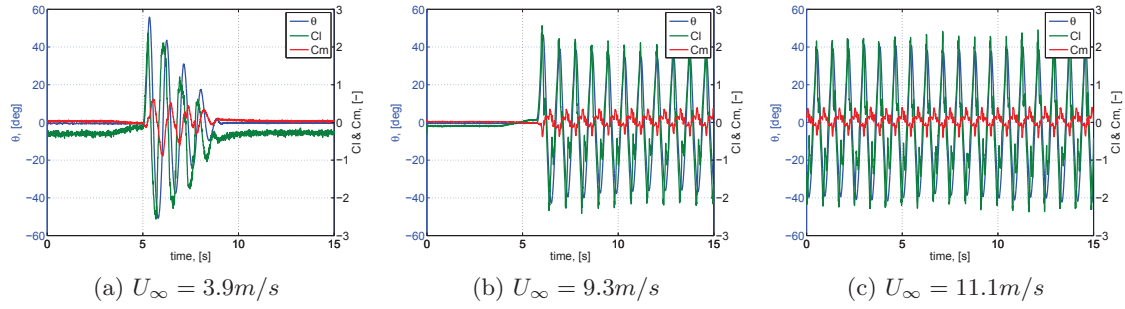


Figure 2.13: Dynamic Pitch Angle and Lift- and Moment Coefficients at different Wind Speeds from Li [7].

external excitation is needed and the wing performs LCOs spontaneously.

An interesting thing to note is that in the low wind speed case right after the excitation there is a small drop in C_m , but increases afterwards and lags the pitching motion by about 90° . However in the high wind speed cases, where LCOs occur the C_m is directly 180° out of phase of the pitching motion.

Bifurcation plots of the experimental pitch angles, plunge displacements, lift- and moment coefficient are shown in Figure 2.14:

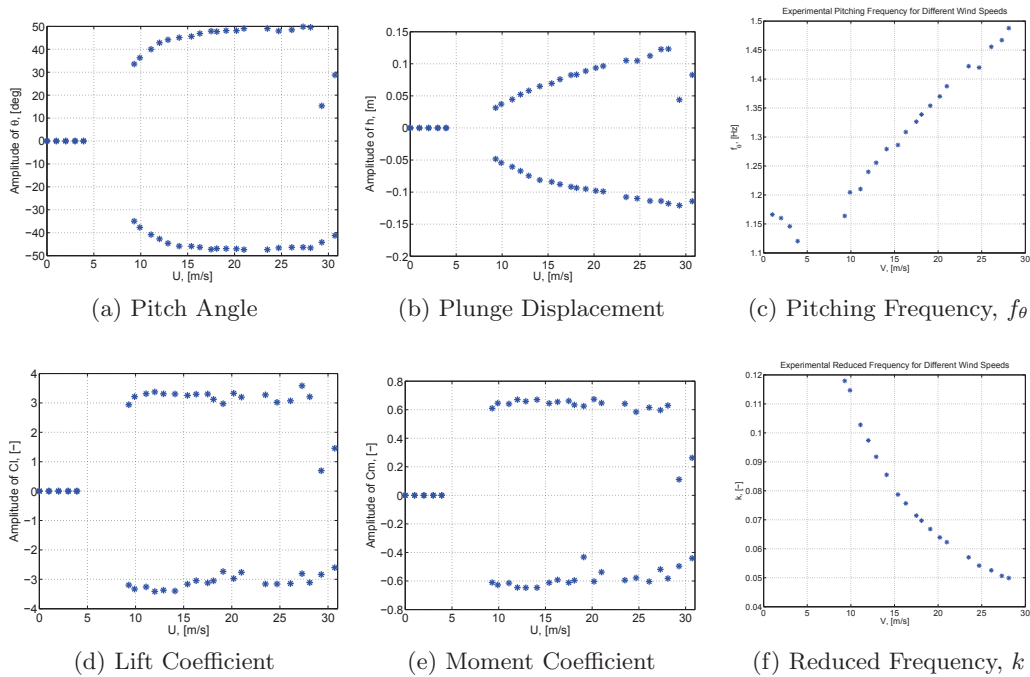


Figure 2.14: Mean Amplitudes and Frequencies of LCOs for Different Wind Speeds from Experiment of Li [7].

From the figure, the most important conclusion to be drawn is that for wind speeds between 9.5 and 15 [m/s], the mean amplitude of especially the pitch angle still increases

and afterwards remains constant. Another point which is noteworthy is the fact that the lift coefficient oscillates with a mean amplitude of around 3 [-] which is almost three times higher than the maximum static lift coefficient. This is a clear indication of the dynamic stall phenomenon at which the maximum instantaneous lift coefficient can significantly exceed the maximum static lift coefficient.

Figure 2.14c and 2.14f show the pitching motion's frequency and reduced frequency respectively for different wind speed. The figures clearly show an increase in frequency and decrease in reduced frequency with an increasing wind speed for wind speeds at which LCOs occur. As, with increasing wind speed, the amplitude of motion remains rather constant when LCOs are seen, the increase of energy in the fluid results in an increase in frequency.

2.5.2 Coalescence Flutter Experiment from Veilleux [8]

Another experiment on self-excited LCOs of a NACA 0012 profiled wing has been carried out by a research group from the Royal Military College of Canada (RMC), Kingston, Ontario, Canada by **Poirel and Mendes** [14]. The wing, mounted on a pivot, was free to move in two degrees-of-freedom. Although their aim was investigating the low-amplitude LCOs caused by the laminar separation bubble at a limited range of transitional Reynolds numbers ($Re = 50\,000$ to $120\,000$), they observed in certain cases high-amplitude LCOs caused by *coalescence flutter* whose exponentially growing amplitude is limited by flow separation at large angles of attack. As mentioned before, a feature of coalescence flutter is that the frequency of oscillation of both degrees-of-freedom tend to merge and this explains the single frequency seen in the experiment. Two different heave stiffnesses were investigated in the experiment and only the resulting pitching- and normalised heaving amplitude and reduced frequency are publicly available. An overview of the structural parameters is given in Chapter 5. The results are shown in Figure 2.15.

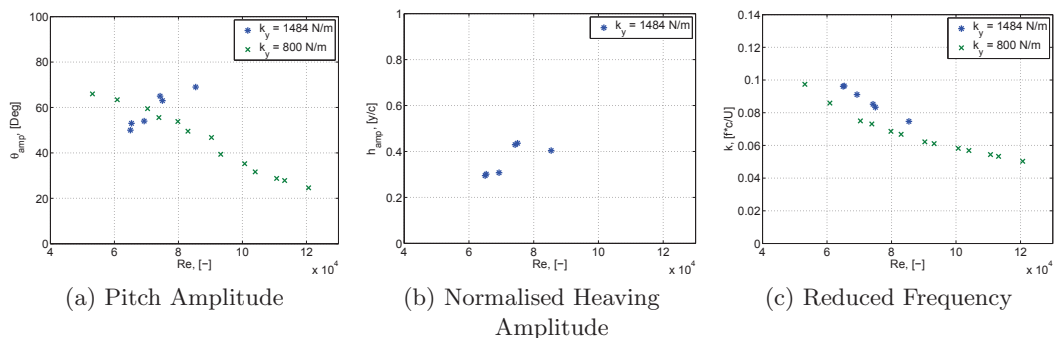


Figure 2.15: Pitch- and Heave Amplitudes and Reduced Frequencies of LCOs as function of Reynolds number from Experiment of **Poirel and Mendes, Veilleux** [14, 15].

The experiment is assessed to be very useful in validating the aeroelastic models developed as part of the thesis. Numerical FSI RANS simulations (with a Spalart-Allmaras turbulence model) have been successfully performed by **Veilleux** [8] on the high-amplitude

LCOs in the experiment from [Poirel and Mendes \[14\]](#). [Veilleux, Veilleux \[8, 15\]](#) provides a more clear and deeper analysis of the high-amplitudes LCOs in the experiment. That is why in the remainder of this report, when referenced to the coalescence flutter experiment, a reference to [Veilleux \[8\]](#) is made.

Engineering Model

In this chapter, the technical set-up of the engineering model used for aeroelastic flutter prediction of an airfoil is described. This means that the first task defined in Section 1.2 is carried out: **Task 1:** *Design a suitable engineering model including a dynamic stall model, which is able to numerically simulate aeroelastic behaviour of an airfoil.* The engineering model consists of two parts: an aerodynamic part and a structural part. In the aerodynamic part, a modified version of the Risø dynamic stall model from Hansen et al. [16], developed at the Danish National Laboratory for Sustainable Energy, is used for the prediction of unsteady aerodynamic loading on the airfoil undergoing arbitrary motion in the pitch- and heave degree of freedom. The structural part consists of the structural equations of motion to solve for the positions and velocities of the airfoil. An iterative procedure uses aerodynamic loading to determine the airfoils position and velocity, and then recalculates the aerodynamic loading for the new position. Section 3.1 describes the method of calculating the unsteady aerodynamic forces. Afterwards, Section 3.2 explains how the structural equations of motion are defined. In Section 3.3, the method of obtaining the semi-empirical constants, which serve as an important input in the aerodynamic model, is described. Section 3.4 deals with validating the aerodynamic model at high-amplitude oscillations. In Section 3.5, the structural part of the engineering model is validated. Finally, a brief summary of the chapter is given in Section 3.6.

3.1 Aerodynamic Part

The Risø dynamic stall model from Hansen et al. [16] is a Beddoes-Leishman type dynamic stall model in state-space representation to model the unsteady loading on an airfoil section undergoing arbitrary motion. In the Risø model, the two major adaptations from the Beddoes-Leishman model are that no compressibility effects are taken into account and the contribution of the leading edge vortex (LEV) to the forces and moment are neglected. The former modification is incorporated as the model is especially designed for the wind turbine environment which usually do not operate in Mach numbers above 0.3 and the flow is thus incompressible. The latter modification is incorporated as it is

assumed that leading edge separation is not a dominating phenomenon for relatively thick airfoils used on wind turbine blades. However, according to Larsen et al. [5], leading edge separation does play a role in wind turbine airfoils as well as thin airfoils; especially in high amplitude changes in the angle of attack, leading edge separation may contribute to the lift significantly. As the experimental data is obtained with a NACA-0012 profiled wing, which is neither a relatively thick nor a typical wind turbine profile, leading edge separation is taken into account in the proposed model and the a comparison of both approaches is presented in Section 3.4. Furthermore, the proposed model includes the effects of shed vorticity from the trailing edge as well as the effects of the instationary trailing edge separation point.

The model is created with the Matlab software package [2], partially in the Simulink-environment. A general flowchart of the model is shown in Appendix D. A concise step-by-step description of the calculations of the unsteady aerodynamic forces and moments is given below. All airfoil specific coefficients or parameters are elucidated in Section 3.3.

1. With the known incoming velocity U , and the geometrical angle of attack at three-quarter chord point of the airfoil, $\alpha_{3/4}$, the effective angle of attack, α_E is calculated as follows:

$$\alpha_E = \alpha_{3/4}(1 - A_1 - A_2) + x_1(t) + x_2(t) \quad (3.1)$$

where A_1 and A_2 are airfoil dependent coefficients and x_1 and x_2 are state variables which are calculated with the following ordinary differential equation (ODE) for $i = 1, 2$:

$$\dot{x}_i + \frac{2U}{c} \left(b_i + \frac{c\dot{U}}{2U^2} \right) x_i = b_i A_i \frac{2U}{c} \alpha_{3/4} \quad (3.2)$$

where \dot{x}_i is the derivative of the first two state variables, b_1 and b_2 are non-dimensional time constants, c is the chord, and \dot{U} is the derivative of the incoming wind speed.

2. With the calculated effective angle of attack and the derivative of the instantaneous angle of attack, $\dot{\alpha}$, the unsteady lift for attached flow can be calculated:

$$C_L^p = C_{L,\alpha}(\alpha_E - \alpha_0) + \pi c \frac{\dot{\alpha}}{2U} \quad (3.3)$$

where the first term represents the circulatory term and the second the non-circulatory term for attached flow. The term $C_{L,\alpha}$ represents the slope of the lift curve in the linear region of attached flow and α_0 represents the angle of attack at zero lift coefficient.

3. According to [Thwaites \[43\]](#), the steady separation point on the airfoil, f^{st} , is calculated according to the calculation of lift on a flat plate in a potential Kirchhoff flow as function of the angle of attack:

$$f^{st} = \left(2\sqrt{\frac{C_L^{st}(\alpha)}{C_{L,\alpha}(\alpha - \alpha_0)} - 1} \right)^2 \quad (3.4)$$

where $C_L^{st}(\alpha)$ is the steady lift curve. The separation point can only vary between 0 and 1, where at $f^{st} = 0$, the flow separates at the leading edge and at $f^{st} = 1$, the flow is fully attached, as shown in [Figure 3.1](#). A few criteria have to be introduced in order to ensure that the separation point is correctly defined and does not reach beyond the defined domain.

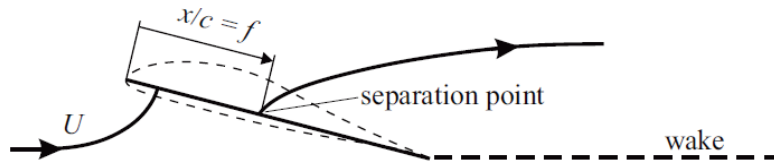


Figure 3.1: The trailing edge separation point, f^{st} , on a flat plate defined in a potential Kirchhoff flow. [Hansen et al. \[16\]](#)

4. The dynamics of the trailing edge separation are included through effectively calculating the dynamic separation point, f'' , by introducing the following two ODEs:

$$\dot{x}_3 + T_p^{-1}x_3 = T_p^{-1}C_L^p(t) \quad (3.5)$$

$$\dot{x}_4 + T_f^{-1}x_4 = T_f^{-1}f'(t) \quad (3.6)$$

where x_3 and x_4 are two additional state variables, T_p is the time constant for the pressure lag, T_f is a time constant for the lag in the boundary layer, $f'(t)$ is an equivalent quasi-steady separation point calculated as $f' = f^{st}(\alpha_f)$ with equation 3.4, where α_f is obtained as $\alpha_f = \frac{x_3}{C_{L,\alpha}} + \alpha_0$. The latter state variable is equal to the unsteady separation point: $f'' = x_4$.

5. The contribution to the lift coefficient during leading edge separation is due to a vortex developing and detaching at the leading edge. Combined with the counter-acting trailing edge vortex, this contribution is called, $C_{L,v}$. During the dynamic stall process, a vortex will develop at the leading edge and increase in strength as long as it is attached or travelling over the airfoil. The vortex starts to travel as soon as the retarded lift coefficient, which is the state variable x_3 , reaches a critical normal coefficient $C'_{L0,v}$, which is an airfoil dependent parameter:

$$\dot{\tau} = \frac{V}{3c}H(x_3 - C'_{L0,v}) \quad (3.7)$$

where $\dot{\tau}$ is the derivative of the travel time of the vortex along the airfoil for which $\tau = 0$ and $\tau = 1$ are respectively equivalent to the time the vortex is at the leading

edge and the trailing edge and H represents the Heaviside function. The ODE for $C_{L,v}$ is shown below:

$$\dot{C}_{L,v}(t) + \omega_4 C_{L,v}(t) = \Delta \dot{C}_L(t) H(1 - \tau) H(\dot{\alpha}) \quad (3.8)$$

where $\Delta \dot{C}_L = C_L^p \left(1 - \left(\frac{1 + \sqrt{f''}}{2} \right)^2 \right)$ and ω_4 is a parameter related to the diminishing effect on the leading edge vortex contribution.

6. The total *unsteady lift coefficient* is obtained by summation of the several contributions and is calculated as follows:

$$C_L^{dyn} = \underbrace{C_{L,\alpha}(\alpha_E - \alpha_0) f'' + C_L^{fs}(\alpha_E)(1 - f'')}_{C_{L,TE}} + \underbrace{\pi T_u \dot{\alpha}}_{C_{L,NC}} + \underbrace{C_{L,v}}_{C_{L,v}} \quad (3.9)$$

where $T_u = \frac{c}{2U}$ is the added mass term.

7. The total *unsteady drag coefficient* is calculated with the known unsteady lift coefficient:

$$C_D^{dyn} = \underbrace{C_D^{st}(\alpha_E)}_{C_{D,st}} + \underbrace{\Delta C_D^{ind}}_{C_{D,ind}} + \underbrace{\Delta C_D^{f''}}_{C_{D,TE}} \quad (3.10)$$

where $C_D^{st}(\alpha_E)$ is the static drag coefficient and the other two terms are calculated as follow:

$$\Delta C_D^{ind} = (\alpha - \alpha_E) C_L^{dyn} \quad (3.11)$$

$$\Delta C_D^{f''} = (C_D^{st}(\alpha_E) - C_{D_0}) \left(\left(\frac{1 - \sqrt{f''}}{2} \right)^2 - \left(\frac{1 - \sqrt{f^{st}(\alpha_E)}}{2} \right)^2 \right) \quad (3.12)$$

8. Finally, the total *unsteady moment coefficient* is obtained:

$$C_M^{dyn} = \underbrace{C_M^{st}(\alpha_E)}_{C_{M,st}} + \underbrace{\Delta C_M^{f''}}_{C_{M,TE}} + \underbrace{\pi T_u \dot{\alpha}}_{C_{M,NC}} \quad (3.13)$$

where $C_M^{st}(\alpha_E)$ is the static moment coefficient, $\Delta C_M^{f''}$ is the unsteady moment due to the dynamic TE separation, $\frac{\pi c \alpha}{4U}$ is the added mass effect due to the pitch rate of the airfoil and the last term represents the moment coefficient as a result of the leading edge vortex. They are calculated as follows:

$$\Delta C_M^{f''} = C_L^{dyn} (a^{st}(f'') - a^{st}(f^{st}(\alpha_E))) \quad (3.14)$$

where a^{st} is the position of an equivalent pressure centre defined by the static lift and moment curves:

$$a^{st} = \frac{C_M^{st} - C_{M_0}}{C_L^{st}} \quad (3.15)$$

Now expressions for the unsteady force- and moment coefficients are known, the corresponding forces, including forces in a ‘ x -’ and ‘ y -’ reference frame, and moment are obtained as follows:

$$L = 0.5\rho U^2 C_L^{dyn} c \quad (3.16)$$

$$D = 0.5\rho U^2 C_D^{dyn} c \quad (3.17)$$

$$M_{0.25} = 0.5\rho U^2 C_M^{dyn} c^2 \quad (3.18)$$

$$F_x = D \cos \alpha - L \sin \alpha \quad (3.19)$$

$$F_y = D \sin \alpha + L \cos \alpha \quad (3.20)$$

where the lift, drag and moment around the quarter-chord point acting on the airfoil are respectively L , D and $M_{0.25}$. With all forces and moments known, their influence on the motion of the airfoil are calculated through solving the structural equations of motion, which is explained in the next section.

3.2 Structural Part

The equations of motion for a system with a stiffness, damping and mass subjected to an external force have been defined in Section 2.4 and are shown in matrix notation below. The system of second order differential equations are solved for the accelerations every time-step with the backslash operator in Matlab.

$$\underbrace{\begin{bmatrix} m & ml \cos \theta \\ ml \cos \theta & I_{RC} \end{bmatrix}}_A \underbrace{\begin{bmatrix} \ddot{y} \\ \ddot{\theta} \end{bmatrix}}_x = \underbrace{\begin{bmatrix} F_y - c_y \dot{y} - k_y y \\ M_{RC} - c_\theta \dot{\theta} - k_\theta \theta \end{bmatrix}}_b \quad (3.21)$$

$$Ax = b \quad (3.22)$$

$$x = b \setminus A \quad (3.23)$$

A fixed time-step of $\Delta t = 0.001$ [s] is used and the explicit fourth-order Runge-Kutta method (ode4 in Matlab) is used to compute the model state at the next time-step. More information about this method can be found in [Butcher \[44\]](#).

3.3 Obtaining the Semi-Empirical Coefficients

The original Risø dynamic stall model only needed six airfoil dependent parameters, but with the implementation of the leading edge separation contribution, two additional parameters are required. In the proposed models the following parameters need to be obtained in order to ensure an accurate simulation: b_1 , b_2 , A_1 , A_2 , T_p , T_f , ω_4 and $C'_{L0,v}$. [Bauchau \[19\]](#) provides a table with values for T_p and T_f for a NACA-0012 airfoil at a range of Mach numbers. An overview of these values are given in Table 3.1. Below, the methods of obtaining all semi-empirical coefficients are explained:

- $\mathbf{b_1, b_2, A_1, A_2}$: These are the indicial lift response coefficients which determine the response of an airfoil to a step input. A technique has been developed by [Bergami et al. \[45\]](#) to determine these coefficients geometrically from the airfoil profile. The coefficients depend on the geometrical angle which is made with the trailing edge of the airfoil at three locations along the surface of the airfoil. For a thin profile in incompressible flow, $A_1 + A_2 \simeq 0.5$ as stated by [Fung \[46\]](#).
- $\mathbf{T_p}$: This parameter represents the time lag of the peak pressure and only depends on the Mach number as stated by [Pereira et al. \[47\]](#) and can be determined if the Mach number is known. [Leishman and Beddoes \[31\]](#) states that the value of T_p is largely independent of airfoil shape. When the T_p value is extrapolated from Table 3.1 to match the Mach-number used in the experiment, which is calculated in Section 2.5, a value of $T_p = 1.5$ [-] is found.
- $\mathbf{T_f}$: This parameter represents the viscous lag and is sensitive to both the profile geometry and Mach number as stated by [Mert \[48\]](#). He numerically obtained that for a variety of airfoils, this value lies between $1.44 \leq T_f \leq 17.56$. For the NACA-0012 airfoil, the value for high Mach-numbers is found in Table 3.1. Extrapolating T_f to the Mach-number in the experiment yields $T_f = 5$ [-]. As this extrapolation introduces some uncertainty in the correct value of the parameter, a sensitivity analysis has been performed. The results are presented in Appendix C and show that modification of this parameter does not significantly change the value of lift- and moment coefficients, but does have a small effect on the rate at which the force coefficients change at high angles of attack. The value of $T_f = 5$ is assessed to be suitable for the current simulations.
- ω_4 : This is a parameter for the leading edge vortex diminishing rate and it is concluded by [Berdowski \[49\]](#) that airfoil responses are not very sensitive to variance of this parameter. The value from [Berdowski \[49\]](#) is taken: $\omega_4 = 0.075$ [-].
- $\mathbf{C'_{L0,v}}$: This is the critical normal coefficient at which the leading edge vortex begins to develop and travel along the airfoil and depends on the Mach-number. According to [Pereira et al. \[47\]](#), the best method of determining this coefficient is to simply take the maximum value of the normal force coefficient. For the NACA-0012, the value has been determined by [Leishman and Beddoes \[31\]](#) and results in $C'_{L0,v} = 1.5$ [-]

Table 3.1: *Semi-Empirical Parameters for a NACA 0012 Airfoil for different Mach Numbers from Bauchau [19]*

M	T_p	T_f
0.30	1.7	3.0
0.40	1.8	2.5
0.50	2.0	2.2
0.60	2.5	2.0
0.70	3.0	2.0
0.75	3.3	2.0
0.80	4.3	2.0

With the methods described above, the coefficients are obtained and an overview is given in Table 3.2.

Table 3.2: *Semi-Empirical Parameters of a NACA 0012 Airfoil at moderate Reynolds Numbers.*

Parameter	Unit	Value
b_1	[-]	0.36
b_2	[-]	0.05
A_1	[-]	0.39
A_2	[-]	0.25
T_p	[-]	1.5
T_f	[-]	5
ω_4	[-]	0.075
$C'_{L0,v}$	[-]	1.5

3.4 Validation of the Aerodynamic Part

In this section, the aerodynamic part of the engineering model is validated against experimental results from Li [7]. A comparison is made between the original Risø dynamic stall model, the model based on the Risø model including the leading edge separation contribution and the experimental force coefficients at different velocities. The responses at two different velocities are investigated: a low wind speed case at which a decaying response is observed and high wind speed case at which LCOs occur. The aerodynamic part is isolated from the structural part in the models and a prescribed motion similar to the experimental motion is enforced. All computations performed with the engineering model are done on a 2.30 GHz Intel(R) Core(TM) i7-3610QM on a single core.

3.4.1 Prescribed Motion at $U_\infty = 3.9$ [m/s] - Decaying Case

The engineering model is forced to follow the motion response at a wind speed of $U_\infty = 3.9$ [m/s] shown in Figure 3.2. The resulting lift- and moment coefficients are respectively

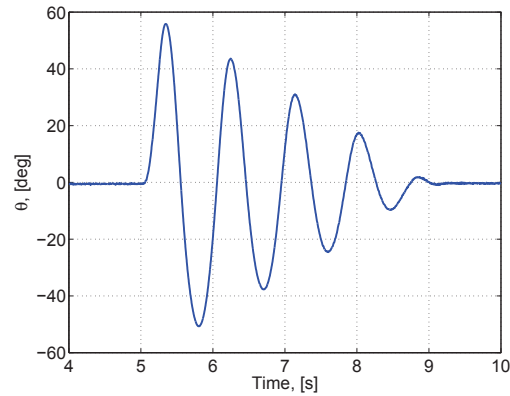


Figure 3.2: Motion at $U_\infty = 3.9$ [m/s] for validation of the Semi-Empirical Model from Li [7].

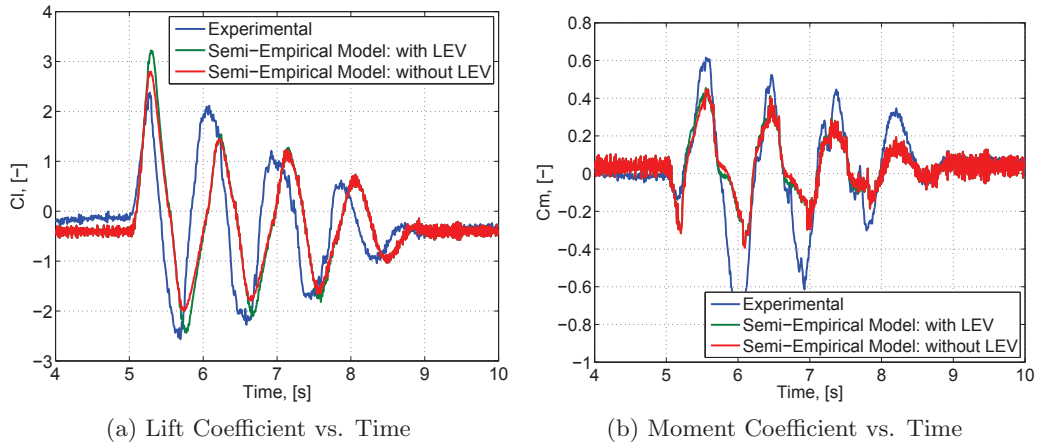


Figure 3.3: Comparison of Lift- and Moment Coefficients at $U_\infty = 3.9$ [m/s] of Semi-Empirical Model and Experimental Results from Li [7].

shown in Figure 3.3a and 3.3b.

Comparing the lift coefficients, it can be seen that overall the maximum amplitude and the trend at negative pitching motion are captured accurately. Including the LEV in the model introduces an additional maximum lift at the maximum pitch angles. Especially at negative pitch angles, the LEV-contribution seems to improve the prediction of the lift coefficient. A drawback of the both semi-empirical models is that it shows a lag in lift coefficient compared to the experimental results.

Regarding the moment coefficient, discrepancies are observed with the experimental data as the predicted moment coefficient is substantially lower. Accurate prediction of the moment coefficient with semi-empirical dynamic stall models have proven to be difficult, but also the inaccuracies in the measurement procedure with the pressure taps in the experiment contribute to this discrepancy. The latter can be seen in the results at low wind speeds in Appendix B, where the force coefficients are overestimated in an unphysical manner.

3.4.2 Prescribed Motion at $U_\infty = 12.9$ [m/s] - Oscillating Case

At a higher windspeed of $U_\infty = 12.9$ [m/s], high-amplitude limit cycle oscillations occur without any initial perturbation. The motion at the concerned wind speed is shown in Figure 3.4. The corresponding force coefficients over time and angle of attack predicted by the engineering model are shown in Figure 3.5. In the plots with the pitch angle on the x -axis, the mean values are indicated with the solid lines and the standard deviations are indicated with the dashed lines.

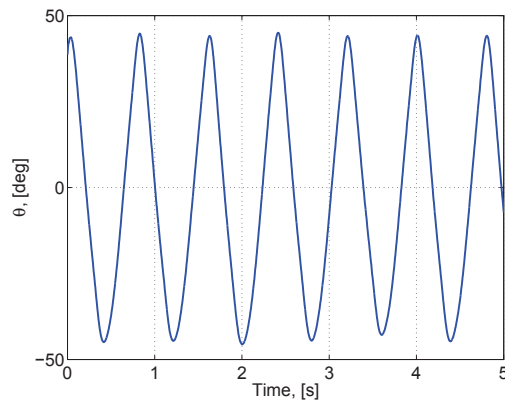


Figure 3.4: Motion at $U_\infty = 12.9$ [m/s] for validation of the Semi-Empirical Dynamic Stall Model from Li [7].

From the figures on the left side, it can be seen that there is a clear difference in the semi-empirical model with- and without the LEV contribution. The model including the LEV-contribution very accurately captures the maxima and minima, while the model without the LEV-contribution substantially underpredicts the lift coefficient. The reattachment of the flow, after a maximum or minimum pitch angle is reached, denoted by the smaller secondary peak is not fully described by both engineering models. However, the general behaviour is described by a delay in the decrease of lift coefficient. The lift coefficient plotted against the pitch angle shows that this delay results in an over- and underestimation in respectively negative- and positive pitching motion.

Contrary to the results at $U_\infty = 3.9$ [m/s], the moment coefficients seem to be accurately predicted and are very similar to the experimental results at $U_\infty = 12.9$ [m/s]. Including the LEV-contribution results in an improved ability of the engineering model to capture the moment coefficient peaks.

3.4.3 Conclusions of Aerodynamic Validation

The force coefficients as a result of a prescribed motion at two different velocities have been obtained in order to judge the aerodynamic part of the engineering model. The results

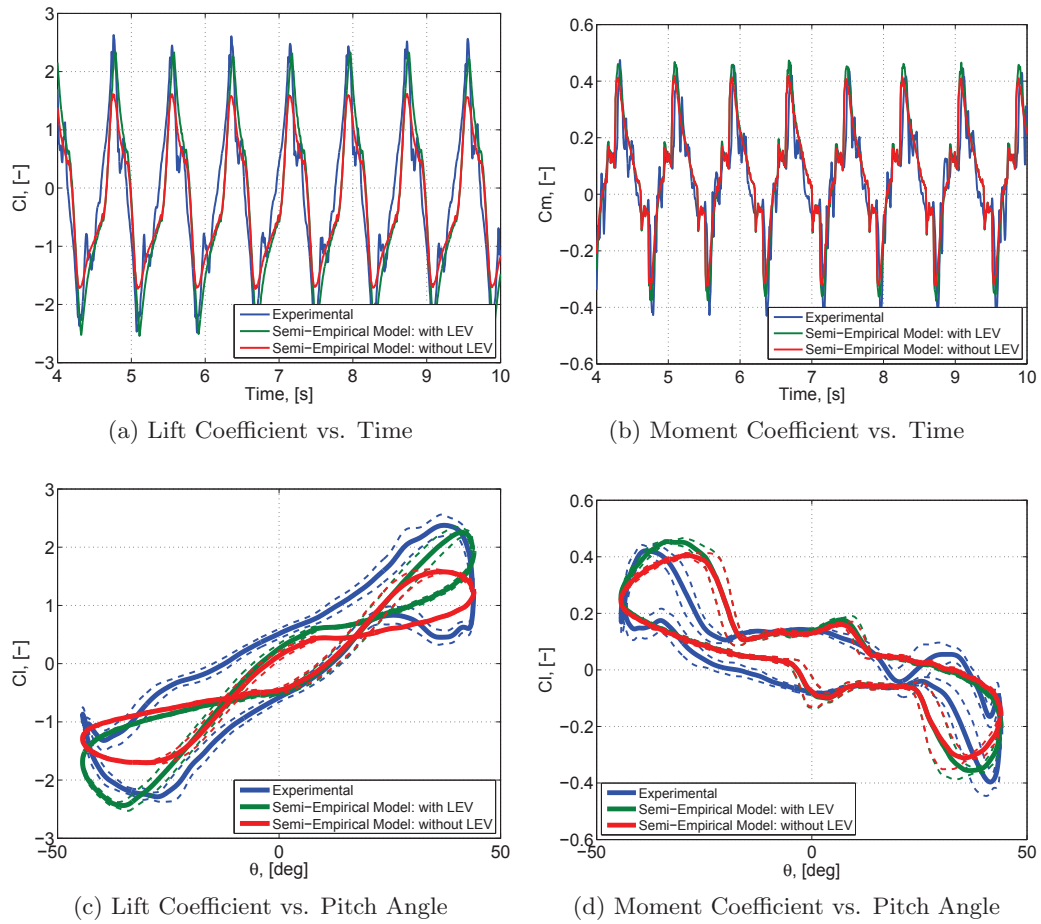


Figure 3.5: Comparison of Lift- and Moment Coefficients at $U_\infty = 12.9$ [m/s] of Semi-Empirical Dynamic Stall Model and Experimental Results from Li [7].

showed that in general the engineering model is able to reproduce the experimental results to a certain extent. The increased force prediction accuracy of the engineering model in the high wind-speed case provides confidence in the ability of the engineering model to simulate high-amplitude limit cycle oscillations. Including the LEV contribution improves the capability of the semi-empirical model to capture the maxima and minima in force coefficients. The aerodynamic part with the LEV contribution of the engineering model is deemed to be sufficiently accurate to use throughout the rest of the study.

3.5 Validation of the Structural Part

This section deals with the validation of the structural part of the engineering model. This means that aerodynamics are not taken into account and a comparison is made with the experimental results of the decaying motion at wind-off conditions.

3.5.1 Obtaining the unknown Structural Parameters

In order to be able to perform the structural validation, all necessary parameters shown in Equation 3.21 have to be known. This implies the use of three parameters that were not explicitly quantified in the experiment; the damping coefficient in pitch and heave, and centre of gravity location. The unknown parameters are quantified in the following two subsections.

Obtaining the Location of the Centre of Gravity

The location of the centre of gravity has not been determined in the experiment and is therefore not available. This location mainly has an effect on the frequency and amplitude of the system's response. This is due to the fact that if the location of the centre of gravity would coincide with the rotational centre, the term l in Equation 3.21 would be zero and the cross-terms are eliminated from the equation.

In general, it can be assumed that the centre of gravity is located aft the rotational centre. Similar studies and experiments take the centre of gravity at around 45% of the chord-length in case of a NACA 0012 profile [Rana et al.](#), [Le et al.](#) [50, 51]. As the NACA 0012 wing used in the experiment does not contain any particular extremities in its mass distribution, it is decided to assume that the location of the centre of gravity is located at 45% of the airfoil's chord.

Obtaining the Damping Coefficients

The damping coefficients in pitch and heave direction of an underdamped system can be obtained by the logarithmic decrement method as explained in [Inman](#) [52]. From the structural response in wind-off condition in the experiment, the damping ratio, ζ [-], is obtained with:

$$\zeta = \frac{1}{\sqrt{1 + \left(\frac{2\pi}{\ln(x_0/x_1)}\right)^2}} \quad (3.24)$$

where x_0 and x_1 are the amplitudes of two consecutive peaks of the pitching- or heaving motion. The pitch- and heave damping coefficient are then respectively obtained with:

$$c_\theta = \zeta_\theta \cdot 2\sqrt{I_{RC} \cdot k_\theta} \quad (3.25)$$

$$c_y = \zeta_y \cdot 2\sqrt{m \cdot k_y} \quad (3.26)$$

The wind-off responses from [Li](#) [7] in both degrees of freedom are displayed in Figure 3.6.

In general, in the case of a constant damping coefficient, a response at wind-off conditions shows a logarithmic decaying trend. It can be clearly seen in the figures that the decay of the pitching- and plunging signal does not show a logarithmic decaying response. From

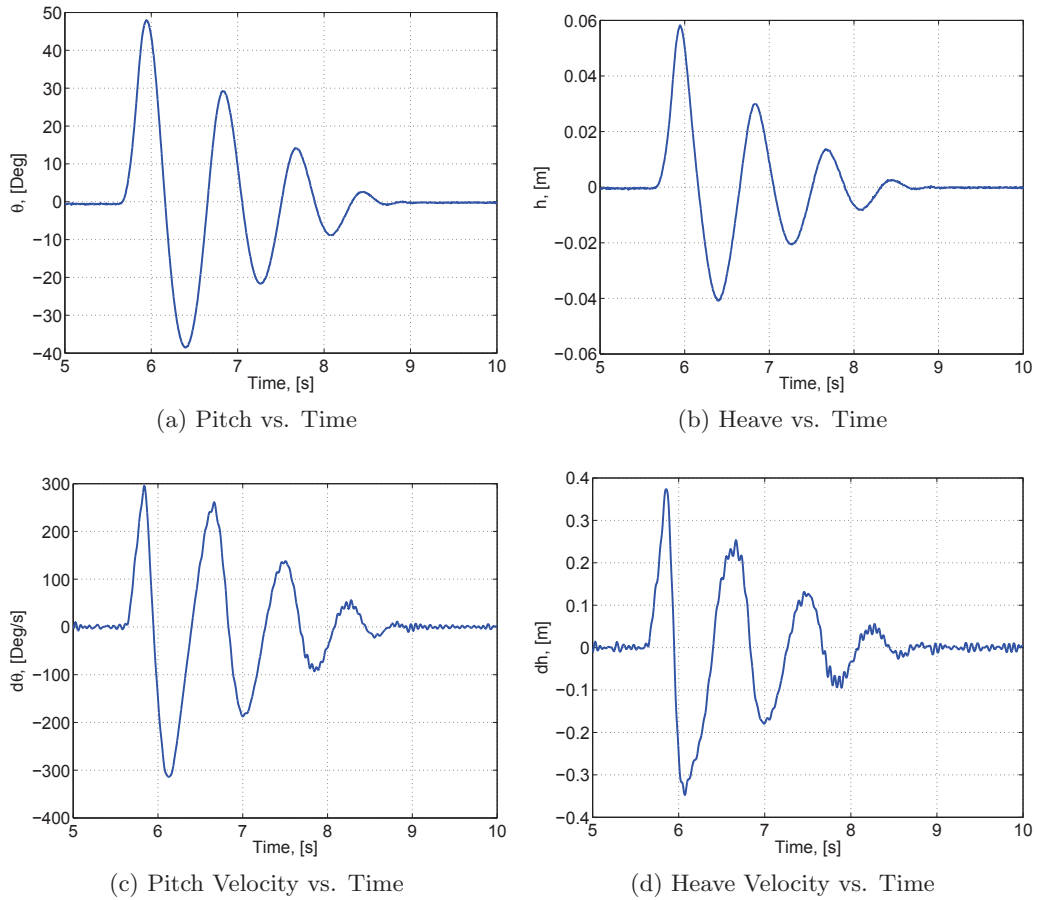


Figure 3.6: Pitch- and Plunge Motion and Velocity Response at Wind-off Conditions of Spring 2 Configuration of Experimental Results from Li [7].

this observation, it can be concluded that the damping coefficient is to a certain extent non-linear.

Obtaining the damping ratios peak to peak from the pitch- and heave velocity responses, shown in Figure 3.6, with equation 3.24 yields the non-linear damping ratio in pitch and heave as displayed respectively in Figures 3.7c and 3.7d. Subsequently, the damping ratios are fitted with a one-term exponential model and extrapolated:

$$y = ae^{bx} \quad (3.27)$$

with the exponential coefficients, input and output shown in Table 3.3.

Table 3.3: Two-term Exponential Fit Coefficients for the Damping Coefficients in Pitch and Heave.

y	x	a	b
$\zeta_{\dot{\theta}}$	$\dot{\theta}$ [Deg/s]	0.3077	-0.006713
$\zeta_{\dot{h}}$	\dot{h} [m/s]	0.2199	-3.898

The damping coefficients in pitch- and heave direction are straightforwardly obtained with Equations 3.25 and 3.26.

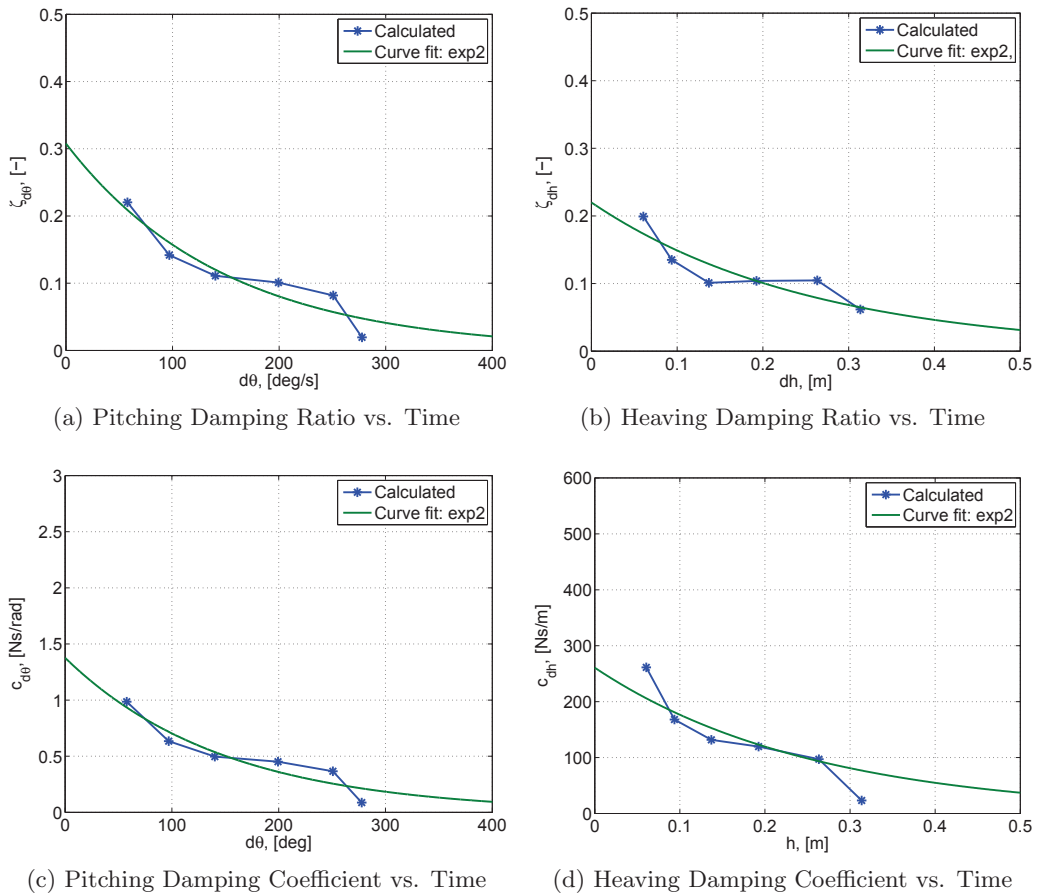


Figure 3.7: Damping- Ratios and Coefficients in Pitch and Heave of Spring 2 Configuration of Experimental Results from Li [7].

3.5.2 Comparison with Wind-off Experimental Results

Now all parameters are known, the wind-off simulation is performed with the structural part of the engineering model and a comparison is made with the experimental response in order to validate the structural part of the engineering model. The airfoil was given an initial pitching velocity similar to the one from the experiment and the response of the airfoil is observed. The pitch- and heave responses of the numerical simulations in

wind-off conditions for the different damping coefficient criterion are compared with the experimental response in Figure 3.8.

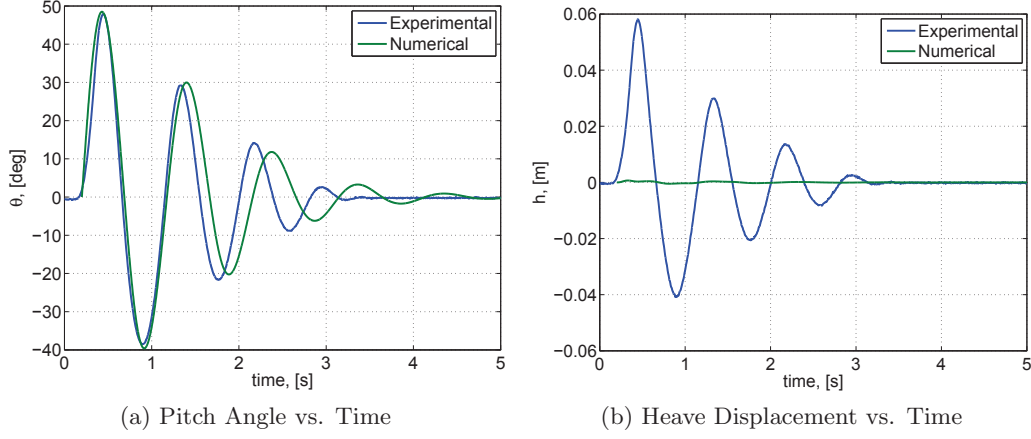


Figure 3.8: Wind-off Responses with Non-linear Damping compared to Experimental Response from Li [7].

Comparing the pitching motion, it can be seen that the response decays in a similar way as in the experiment: lower decay at high amplitudes and higher decay at low amplitudes which results in similar pitch amplitudes. Regarding the heave motion, the numerical excitation in heave direction is negligible compared to the experimental heave motion. This is due to fact that the high stiffness in heave is the most decisive factor in the heaving motion refraining from excitation. However, it is believed by the author that the high heave stiffness value given in the experiment is questionable. Reducing the damping coefficient in heave does not improve the heave response motion. Introducing an initial heaving velocity results in a high frequency heaving response not similar to the experimental heave response. In the experiment, the heave response is purely due to the pitching motion and oscillates at the same frequency.

From the numerical response, it clearly can be seen that the obtained frequency in pitch is lower than the experimental ones. The theoretical undamped- and damped frequency in pitch, $f_{\theta,u}$ and $f_{\theta,d}$, are respectively calculated as follow:

$$f_{\theta,u} = \frac{1}{2\pi} \cdot \sqrt{\frac{k_{\theta}}{I_{RC}}} \quad (3.28)$$

$$f_{\theta,d} = f_{\theta,u} \cdot \sqrt{1 - \zeta_{\theta}} \quad (3.29)$$

The different frequencies in pitch are shown in Table 3.4.

Table 3.4: Numerical and Theoretical Frequencies at Wind-Off Conditions compared to Experimental Observed Frequency from Li [7].

	f, [Hz]
$f_{\theta,exp}$	1.20
$f_{\theta,num}$	1.02
$f_{\theta,u}$	1.03
$f_{\theta,d}$	1.01

The experimentally observed frequency is around 18% higher than the theoretical- and numerical obtained frequency. It is believed that this is caused by a supposed non-linear stiffness in the system which has a direct effect on the frequency as indicated by Equation 3.28. For the sake of simplicity and due to the uncertainty in quantifying the non-linear stiffness, it is decided to not take this non-linearity into account. However, care should be taken as this might have an effect on the critical onset velocity of the LCOs.

3.5.3 Conclusions of the Structural Validation

Validating the structural part with experimental data from Li [7] has proven to be neither easy nor straightforward. The complexity due to the non-linearities and uncertainties in the experiment complicate the validation of the structural part. However, with the approximation of the pitching motion obtained in the previous section it is assessed that the structural part, given accurate damping and stiffness input, works accordingly. The heaving motion is considered to be of less importance as all responses in the experiment are pitch dominated as stated by Li [7].

An overview of the final structural parameters of the experiment from Li [7] are given in the Table 3.5. An indication is given whether the parameter has been quantified in the experiment or has been obtained previously in this section.

Table 3.5: Experiment Structural Parameters from Li [7].

Parameter	Symbol	Unit	Value	Given/Obt.
Chord	c	[m]	0.3	Given
Span	S	[m]	0.9	Given
Torsional Spring Stiffness	k_{θ}	[N · m/rad]	13.07	Given
Compression Spring Stiffness	k_y	[N/m]	18 976	Given
Centre of Rotation	x_{RC}	[%]	38.33	Given
Mass M.o.I around the C.R.	I_{RC}	[kg · m ²]	0.31	Given
Mass	M	[kg/m]	16.67	Given
Centre of Gravity	x_{CG}	[%]	45	Obtained
Torsional Damping Coefficient	C_t	[N · s/rad]	$ae^{b\theta} \cdot 2\sqrt{I_{RC}k_{\theta}}$	Obtained
Heaving Damping Coefficient	C_y	[N · s/m]	$ce^{dh} \cdot 2\sqrt{mk_y}$	Obtained

3.6 Summary

This chapter has dealt with the first model proposed for the aeroelastic simulations of an airfoil, i.e. the engineering model. The adapted version of the Risø semi-empirical dynamic stall model used as the aerodynamic part and the structural part have been discussed and validated. Completing this chapter has been equivalent to performing the first task as defined in Chapter 1: **Task 1:** *Design a suitable engineering model including a dynamic stall model, which is able to numerically simulate aeroelastic behaviour of an airfoil.* The engineering model showed to be capable of numerically obtaining force coefficients at a high-amplitude motion to a satisfactory accuracy and that including the LEV contribution in the dynamic stall model improved this force prediction as compared to experimental data from Li [7]. Now the engineering model has been designed and validated, it is assessed to be suitable for the aeroelastic simulations of an airfoil which will be performed in Chapter 5. The next chapter deals with the theory, set-up and validation of the other proposed model for aeroelastic simulations of an airfoil: the RANS model.

Chapter 4

RANS Model

The engineering model discussed in the previous chapter represents a model which describes the behaviour of a transient airfoil by means of a simplification and decomposition of the physics involved in the dynamic motion. As this method does not fully capture all physical quantities involved in the process, a deeper and broader understanding hereof can be obtained by solving the Navier-Stokes equations by means of CFD computations. This chapter describes such model. This is related to the second task as defined in Chapter 1: **Task 2.** *Design a reliable, accurate and efficient RANS model in OpenFOAM which is able to numerically simulate aeroelastic behaviour of an airfoil.* The goal of this chapter is to provide an overview of the necessary steps taken in developing a reliable, accurate and efficient aeroelastic RANS model within the OpenFOAM-framework. This is done by dividing this chapter into five sections. The first section describes several fundamental theories behind numerical simulations of fluid flows by means of CFD computations. Section 4.2 deals with a grid convergence study which is conducted in order to reduce the spatial discretisation error and ensure spatial convergence of the grid. A temporal convergence study to obtain a time-independent solution is performed in Section 4.3. Section 4.4 describes the set-up of the aeroelastic RANS model used later on. To conclude this part, a brief overview of the chapter is given Section 4.5.

4.1 Theory

This section describes several fundamental theoretical principles behind solving the Navier-Stokes equations by means of CFD computations. Firstly, the Navier-Stokes equations are described. Secondly, a description of the discretisation methods within the OpenFOAM-framework is given. Afterwards, some principles of turbulence and turbulence modelling are explained. The last part of this section describes an important region when solving fluid flows around an airfoil: the boundary layer.

4.1.1 Navier-Stokes Equations

When applying Newton's second law to fluid motion (conservation of momentum) together with the assumption that the stress in the fluid is the sum of a diffusing viscous term and a pressure term, the Navier-Stokes equations arise. These non-linear partial differential equations are able to describe the motion of fluid substances. The general form of the equations of fluid motion for an incompressible flow consist of the incompressible continuity equation which represents the conservation of mass:

$$\frac{\partial u}{\partial x} + \frac{\partial v}{\partial y} = 0 \quad (4.1)$$

and the incompressible Navier-Stokes equations which represent the conservation of momentum:

$$\underbrace{\frac{\partial \mathbf{v}}{\partial t}}_{\text{Time Variation}} + \underbrace{\mathbf{v} \cdot \nabla \mathbf{v}}_{\text{Convection}} = \underbrace{-\frac{\nabla p}{\rho}}_{\text{Pressure}} + \underbrace{\nu \nabla^2 \mathbf{v}}_{\text{Viscous}} + \underbrace{\mathbf{F}}_{\text{External Force}} \quad (4.2)$$

where \mathbf{v} is the fluid velocity, p is the fluid pressure, ρ is the fluid density, $\nu = \mu/\rho$ [m^2/s] is the kinematic viscosity and \mathbf{F} is an external force applied to the fluid. The meaning of the different contributing terms are given underneath.

The Navier-Stokes equations can also be written in Einstein notation:

$$\frac{\partial u_i}{\partial t} + u_j \frac{\partial u_i}{\partial x_j} = -\frac{1}{\rho} \frac{\partial p}{\partial x_i} + \nu \frac{\partial^2 u_i}{\partial x_j^2} + f_i \quad (4.3)$$

Solving the Navier-Stokes equations yields the velocity- and pressure fields. When these quantities are obtained, other quantities of interest, such as lift- and drag forces may be found. Analytical solutions of the Navier-Stokes equations are practically non-existent as they are highly non-linear coupled differential equations due to the quadratic non-linearity in the *convective* term. That is why these equations need to be solved numerically at discrete points. In the remainder of this section, the procedure of numerically solving the Navier-Stokes equations are described.

4.1.2 Discretisation

In order to numerically solve the Navier-Stokes equations, a computational domain is created which on its turn is divided into small elements. The discretisation method used in OpenFOAM is the *finite volume method* (FVM) approximation. This method divides the domain into a finite number of contiguous control volumes (CVs). Taking the integral form of the Navier-Stokes equations over the control volume, V_c , yields the following equation:

$$\int_{V_c} \frac{\partial u_i}{\partial t} dV + \int_{V_c} u_j \frac{\partial u_i}{\partial x_j} dV = - \int_{V_c} \frac{1}{\rho} \frac{\partial p}{\partial x_j} dV + \int_{V_c} \nu \frac{\partial^2 u_i}{\partial x_j^2} dV \quad (4.4)$$

Each term can be evaluated after implementation of Gauss' theorem and after the boundary conditions are set. This theorem relates the flux of a vector field through a surface to the behaviour of the vector inside the surface and is more extensively explained in Jasak [53]. After the discretisation of each term has been done, the discrete form of the Navier-Stokes equations are solved in OpenFOAM in a *segregated approach* where the equations are solved in sequence [53].

Solution Algorithms

Considering the discretised form of the Navier-Stokes equations, a pressure-velocity coupling is observed. Two algorithms are most popular when dealing with this inter-equation coupling in the pressure-velocity system: the *Semi-Implicit Method for Pressure-Linked Equations*-algorithm (SIMPLE) by Patankar [54] and the *Pressure Implicit with Splitting of Operators*-algorithm (PISO) by Issa [55]. The so-called PIMPLE-algorithm is a hybrid version of the PISO- and SIMPLE-algorithm. The step-by-step procedure of the algorithms are described into more detail in Appendix E. A brief overview of the methods of the different algorithms are is given below:

- **SIMPLE:** The SIMPLE-algorithm solves a steady-state problem iteratively which eliminates the necessity to fully resolve the linear pressure-velocity coupling. The momentum equation is solved and a velocity field is obtained. The pressure gradient term is calculated using an old pressure distribution and a new pressure distribution is obtained. With the new pressure distribution, the face fluxes are calculated.
- **PISO:** The PISO-algorithm is an extension of the SIMPLE-algorithm and is used for transient flow computations. It solves the momentum equation for the velocity field with the pressure field from the previous time step. Using the new velocity field, a first estimate of the new pressure field is obtained by solving the pressure equation. With the new pressure field, the velocity is corrected and the cell face fluxes are calculated.
- **PIMPLE:** Works similarly as the PISO-algorithm, but with two additions: an outer correction loop and underrelaxation of the variables.

Arbitrary Lagrangian-Eulerian Approach

OpenFOAM uses, in case of a stationary mesh, an *Eulerian* approach. In the *Eulerian* approach, which is described in more detail in Batchelor [56], the focus lies on specific locations in space and physical quantities of the fluid flows are measured over time when they pass through these points. This is different from the *Lagrangian* approach in which individual particles are followed in space and time. In case of a moving- or deforming mesh, OpenFOAM implements a combination of the *Eulerian*- and *Lagrange* approach in a so-called *Arbitrary Lagrangian Eulerian*-method (ALE) as explained in Donea et al. [57]. The concerning ALE-approach introduces an additional mesh velocity in the convective term in Equation 4.4. Together with the fact that in a deforming mesh, the volume of each

particular cell changes over time leads to the following formulation of the Navier-Stokes equation of a moving- and/or deforming mesh:

$$\frac{\partial}{\partial t} \int_{V_c} u_i dV + \int_{V_c} u_j \frac{\partial(u_i - u_m)}{\partial x_j} dV = - \int_{V_c} \frac{1}{\rho} \frac{\partial p}{\partial x_j} dV + \int_{V_c} \nu \frac{\partial^2 u_i}{\partial x_j^2} dV \quad (4.5)$$

where u_m represents the motion of the mesh. This modification introduces a new criteria which is called the *Discrete Geometric Conservation Law* (DGCL) which states that the change of the volume of a particular cell must be equal to the volume swept by the faces of the cell.

Time Discretisation

In order to perform transient simulations, OpenFOAM incorporates implicit time-stepping. The implicit method finds solutions of the next time step by evaluating the current state of the system and the next one. In equation form as formulated by [Butcher \[58\]](#):

$$y_{i+1} = y_i + hf(t_{i+1}, y_{i+1}) \quad (4.6)$$

A widely used condition in mathematics is the *Courant-Friedrichs-Lewy* (CFL) condition which is used in numerically solving certain partial differential equations originally formulated by [Courant et al. \[59\]](#). An important quantity in this condition is the Courant number. The Courant number is a measure of the time it takes for a fluid particle to travel through a particular cell and is defined as:

$$Co = \frac{u\Delta t}{\Delta x} \quad (4.7)$$

where u is the velocity of the particle, Δt is the time-step and Δx is the length of the cell. In *explicit* simulations, the condition must be fulfilled that the Courant number must be smaller than 1. Due to the unconditionally stable nature of *implicit* time stepping, implicit simulations are not constrained with the criteria that the Courant number should be lower than 1. [Ansys \[60\]](#) states that typical values are $Co = 2-10$, but in some cases higher values are acceptable.

4.1.3 Turbulence

Although, the Navier-Stokes equations are capable to solve turbulent flows, it is numerically extremely difficult due to the nature of turbulence. Turbulence are characterised as an unsteady, three-dimensional, irregular, stochastic motion in which transported quantities (mass, momentum, scalar species) fluctuate in time and space as stated in [Ansys \[17\]](#). In turbulent flows, unsteady vortices appear on many scales and interact with each other. The range of scales in such flows is very large, from the smallest turbulent eddies characterised by Kolmogorov microscales, to the flow features comparable with the size of the

geometry. In turbulent flows, energy is transferred from larger eddies to smaller eddies which is known as the 'Kolmogorov Cascade'. The large scale eddies contain most of the energy and in the smallest eddies, turbulent energy is converted into internal energy by viscous dissipation.

Turbulence Modelling

In order to solve for turbulence in fluid flows, several models are available. The models with their characteristics are listed below.

- Reynolds Averaged Navier-Stokes Simulation (RANS)
 - Solves time-averaged Navier-Stokes equations
 - All turbulent length scales are modelled in RANS
 - Various different models are available
 - Computational cheap
- Large Eddy Simulation (LES)
 - Solves the spatially averaged Navier-Stokes equations
 - Large eddies are directly resolved, but eddies smaller than the mesh are modelled
 - Computational expensive
- Detached Eddy Simulation (DES)
 - Hybrid method of RANS and LES
 - Treats near-wall region with a RANS approach and the bulk flow with a LES approach.
 - Computational expensive
- Direct Numerical Simulation (DNS)
 - Numerically solving the full unsteady Navier-Stokes equations
 - Resolves the whole spectrum of scales
 - No turbulence modelling is required
 - Extremely computational expensive

As it is not necessary in the project to fully resolve the flow on the smallest scales and a time-efficient solution is required, it is decided to use the RANS-approach to simulate the turbulent flow. The method of obtaining the RANS equations from the N-S equations is explained below.

RANS Equations

By separating the local value of the variable into the mean and the fluctuation around the mean, it is possible to derive the equations for the mean properties themselves. In the RANS-method, turbulent flow can be decomposed into its time-averaged and fluctuating quantities:

$$u = \bar{u} + u' \quad (4.8)$$

With this decomposition implemented in the Navier-Stokes equations from Equation 4.3, as originally described in Reynolds [61], the full RANS-equations become:

$$\rho \frac{\partial \bar{u}_i}{\partial t} + \rho \bar{u}_j \frac{\partial \bar{u}_i}{\partial x_j} = \rho \bar{f}_i + \frac{\partial}{\partial x_j} \left[-\bar{p} \delta_{ij} + 2\mu \bar{S}_{ij} - \rho \overline{u'_i u'_j} \right] \quad (4.9)$$

where $\bar{S}_{ij} = \frac{1}{2} \left(\frac{\partial \bar{u}_i}{\partial x_j} + \frac{\partial \bar{u}_j}{\partial x_i} \right)$ is the mean rate of strain tensor, δ_{ij} is the Kronecker delta and $-\rho \overline{u'_i u'_j}$ is referred to as the Reynolds stress. This is the general Reynolds Averaged Navier-Stokes equation. These averaged equations are not closed (number of unknown variables are greater than the number of equations) and require the introduction of turbulence models.

RANS Turbulence Models

A closure problem arises due to the introduction of the non-linear Reynolds stress term in the RANS equation. In order to close the problem and solve the equation, the turbulent stresses are related to the mean flow by means of Boussinesq's hypothesis:

$$\overline{u'_i u'_j} = \nu_t \left(\frac{\partial \bar{u}_i}{\partial x_j} + \frac{\partial \bar{u}_j}{\partial x_i} \right) - \frac{2}{3} k \delta_{ij} \quad (4.10)$$

where k [m^2/s^2] represents the turbulent kinetic energy. This introduces an extra variable called the *turbulence eddy viscosity*, ν_t [m^2/s], which has to be solved for. This is done by using one of the turbulence models, of which the most commonly employed models in modern engineering applications are listed below:

- Spalart-Allmaras (S-A)
- k - ϵ
- k - ω
- k - ω SST (Menter's Shear Stress Transport)
- Reynolds stress equation model

where ω [1/s] is the specific turbulence dissipation and ϵ [m^2/s^3] is the turbulence dissipation. A turbulence model which is considered to be an effective and accurate is the k - ω SST model from [Menter \[62\]](#). It is a two-equation eddy-viscosity model in which the shear stress transport (SST) formulation combines the best of two worlds. It combines the k - ω with the k - ϵ turbulence model in a way that the k - ω -model is used in the inner region of the boundary layer and switches to k - ϵ behaviour in the free-stream. This method avoids the common k - ω problem that the model is too sensitive to the inlet freestream turbulence properties. The use of k - ω in the inner region of the boundary layer ensures that the model is valid within the viscous sub-layer and thus can be used as a low-Re turbulence model without any extra damping functions. It is generally believed that the k - ω SST results in relatively good solutions for the flow with a large area of separation. Previous studies have shown that the k - ω SST turbulence model yields the best results compared to experimental data in flows over static or dynamic airfoils ([\[63, 64, 65, 66, 67\]](#)).

The two-equation model, respectively for k and for ω , is formulated as follows:

$$\frac{\partial(\rho k)}{\partial t} + \frac{\partial(\rho u_j k)}{\partial x_j} = P - \beta^* \rho \omega k + \frac{\partial}{\partial x_j} \left[(\mu + \sigma_k \mu_t) \frac{\partial k}{\partial x_j} \right] \quad (4.11)$$

$$\begin{aligned} \frac{\partial(\rho \omega)}{\partial t} + \frac{\partial(\rho u_j \omega)}{\partial x_j} &= \frac{\gamma}{\nu_t} P - \beta^* \rho \omega^2 + \frac{\partial}{\partial x_j} \left[(\mu + \sigma_\omega \mu_t) \frac{\partial \omega}{\partial x_j} \right] \\ &+ 2(1 - F_1) \frac{\rho \sigma_{\omega 2}}{\omega} \frac{\partial k}{\partial x_j} \frac{\partial \omega}{\partial x_j} \end{aligned} \quad (4.12)$$

An extensive description of all parameters found in Equation 4.11 and 4.13 is given in Appendix F. In order to solve the RANS equations with the k - ω SST turbulence model properly, the values of the turbulence parameters (k , ω and ν_t) at the boundary conditions have to be approximated. This is done following the formulation of [\[68\]](#):

$$k_{ff} = \frac{3}{2} U_\infty^2 I^2 \quad (4.13)$$

$$\frac{\nu_t}{\nu} = 2 \times 10^{-7} \cdot Re \quad (4.14)$$

$$\omega_{ff} = \frac{k_{ff}}{\frac{\nu_t}{\nu} \cdot \nu} \quad (4.15)$$

$$\nu_{t_{ff}} = \frac{k_{ff}}{\omega_{ff}} \quad (4.16)$$

$$\omega_w = \text{omegaWallFunction} \quad (4.17)$$

$$k_w = \text{kqRWallFunction} \quad (4.18)$$

$$\nu_{t_w} = \text{nutWallFunction} \quad (4.19)$$

where the turbulence intensity, I [-], is formulated as follows $I = \frac{\sigma}{U_\infty}$, where σ [m/s] is the standard deviation in the freestream flow. Furthermore, the subscripts ‘ w ’ and ‘ ff ’ denote respectively the wall- and farfield boundary condition.

4.1.4 Boundary Layer

An important and widely studied region is the boundary layer on the airfoil. The fluid flow around an object can be divided in two areas: one inside the boundary layer, dominated by viscosity and creating the majority of drag experienced by the boundary body and one outside the boundary layer, where viscosity can be neglected without significant effects on the solution. A boundary layer can be *laminar* or *turbulent*, where the former is characterised by its ‘smooth’ flow and the latter by swirls or ‘eddies’ in the flow. The turbulent boundary layer can be divided into three layers as shown in Figure 4.1: the sublayer- and buffer layer and the fully-turbulent region/log layer which together form the inner layer of the boundary layer and the outer layer. In the sublayer, the turbulence is suppressed by (molecular) viscosity and therefore is a thin laminar layer at which the velocity gradient is linear. In the turbulent log layer, the velocity profile is logarithmic and turbulence plays a major role. The outer region serves as an interim region between the viscous sublayer and the fully turbulent layer.

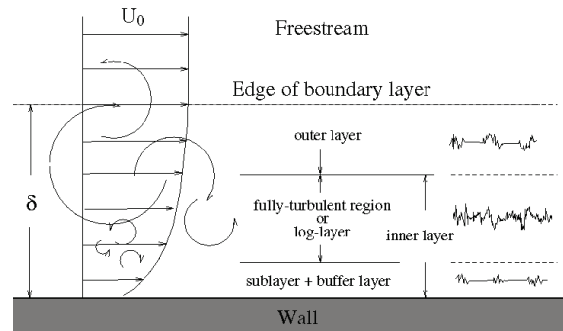


Figure 4.1: Turbulent Boundary Layer. [17]

The shape of the boundary layer has an impact on the performance of an airfoil such as lift- and drag coefficients. That is why it is important to accurately capture the correct behaviour of the boundary layer in numerical simulations. Traditionally, there are two methods when it comes to modelling the near-wall region. One method does not resolve the sublayer + buffer layer region, but uses the so-called ‘wall-functions’. These are semi-empirical formulas which determine the near wall velocity profiles. The other method fully resolves the near-wall region. A graphical overview of these methods is given in Figure 4.2.

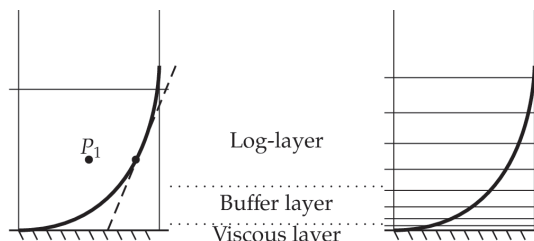


Figure 4.2: Boundary Layer Wall Treatment. [18]

The right graph shows the grid structure of fully resolving the boundary layer and the

left graph shows the usage of one cell in the inner region of the boundary layer which is resolved by means of a wall function. Using one of these methods in numerical simulations comes down to selecting a suitable y^+ -number, which is the non-dimensional wall distance. The required cell height near the wall depends on this number:

$$y^+ = \frac{dy \cdot u_\tau}{\nu} \quad (4.20)$$

where dy [m] is the initial cell height and u_τ [m/s] is the friction velocity near the wall. An overview of both methods and their characteristics is given below:

- Resolving the Viscous Sublayer
 - Initial cell height should be about $y^+ = 1$
 - Computational more expensive
 - A low-Reynolds number turbulence model should be used
- Using a Wall Function
 - Initial cell height needs to be $30 < y^+ < 300$
 - Computational less expensive
 - Uses wall function approach with high Reynolds turbulence model.

In order to obtain the initial cell height, the following steps have to be undertaken. From the Reynolds number, the skin friction coefficient $Cf[-]$ can be determined for external flows following the formulation from [Schlichting et al. \[69\]](#).

$$Cf = 0.0592 \cdot Re^{-0.2} \quad (4.21)$$

With the skin friction, the initial cell height is obtained with the following equation:

$$dy = 2 \cdot \frac{y^+ c}{Re \sqrt{\frac{Cf}{2}}} \quad (4.22)$$

This equation will be used in the grid convergence study in the next section in order to determine the height of the first cell on the airfoil. A previous study by [Lof \[70\]](#) has proven that solving for a $y^+ < 1$ yields better results in case of a steady or transient simulation over an airfoil, especially in high angles of attack. This value will be used during the rest of the study.

4.2 Grid Convergence Study

In order to ensure that the solution obtained with the CFD simulations is independent of a mesh refinement, a so called *grid convergence study* is performed. The mesh refinement is done by means of decreasing the sizes of the cells throughout the whole domain. This is done by increasing the total number of cells in the domain while keeping the domain size constant.

The mesh of the airfoil and it's domain are created in Pointwise [71]. In order to ensure an accurate, robust and efficient simulation a grid convergence of the model is performed. There are two realistic options when it comes to grid generation: an O-grid or a C-grid. They both have their advantages and disadvantages as stated in Lutton [72]. For example: the O-grid is superior to the C-grid in determining the pressure coefficient in the vicinity of the leading edge in the subsonic range. However, the C-grid may capture the wake slightly more accurate due to the high grid point concentration directly behind the airfoil. It has been decided to use an O-grid for the mesh because of its ease of generation and application in OpenFOAM. The grid convergence study is carried out at an angle of attack of 5° in a steady simulation by means of the SIMPLE-algorithm which interchangeably iterates over the velocity and pressure to drive the equations towards convergence. Several key parameters are varied while others are kept constant. An overview of the key parameters is given in table 4.1.

Table 4.1: Key Parameters for Grid Convergence Study

Parameter	Symbol
Number of Grid Points on Airfoil	n_a
Grid Point Spacing - L.E. & T.E.	ds
Initial Cell Height	dH
Growth Rate	GR
Number of Cells	N
Domain Size	D

4.2.1 Initial Cell Height Determination with y^+

The height of the first layer of cells, $dH[m]$ on the airfoil is determined with the value of the y^+ -number $[-]$, chord of the airfoil, air velocity and the kinematic viscosity. The last three parameters yield the Reynolds number. The procedure is described in Section 4.1.4. To ensure that the y^+ -number remains smaller than 1 for the whole range of velocities used in the experiment, the maximum Reynolds number is taken and used to calculate the initial cell height. Equation 4.22 yields an initial cell height of $dH = 2 \times 10^{-5}[m]$.

4.2.2 Parameter Variation

The first step to be taken is to fix the initial cell height, dH , and the Domain Size, D . A rule of thumb is to keep the grid point spacing towards the leading- and trailing edge

more or less equal to the initial cell height, dH . Furthermore, another common practice is to use a domain with a radius of around 80 times the chord length of the airfoil. The amount of grid points on the airfoil, n_a , as well as the total number of cells in the domain, N , are varied. In order to vary the total amount of cells, which are doubled each finer grid, the growth ratio is varied. Thus, the growth ratio depends on the number of grid points on the airfoil and the total amount of cells. This leads to the study set-up shown in Table 4.2.

Table 4.2: Variation of Parameters in Grid Convergence Study

Parameter	Unit	Value
Initial Cell Height	[m]	2×10^{-5}
Domain Radius	[c]	80
No. of Grid Points on the Airfoil	[-]	[150 200 250 300]
Total Number of Cells	[-]	\approx [10 000 20 000 40 000 80 000]
Growth Rate	[-]	varied

4.2.3 Grid Convergence Results

The simulations on the NACA0012 airfoil at $\alpha = 5^\circ$ with a varying number of grid points on the airfoil's surface and total number of cells are performed. For every case, the criteria is set that solution convergence must be reached. The simulations are done on a 2.5 GHz Intel(R) Xeon(R) CPU E5-2670v2 processor on a single core. The amount of iterations is set to 5000 and the duration of the simulation depends on the number of cells. A typical progress towards solution convergence is depicted in Figure 4.3. The horizontal development of the force coefficients and the residuals of the variables of interest after around 1500 iterations together with the low values of the residuals ($< 1 \times 10^{-3}$) show that the solution is converged. However, it must be said that convergence of the solution does not necessarily mean that the solution is accurate.

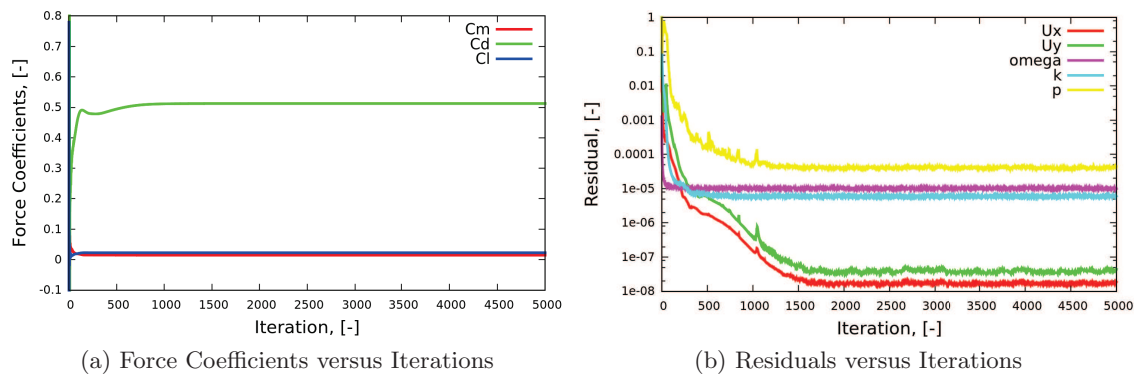


Figure 4.3: Plots of a typical Steady-State Converged Case

An overview of the resulting lift- and moment coefficients for the various grid designs is given in Figure 4.4

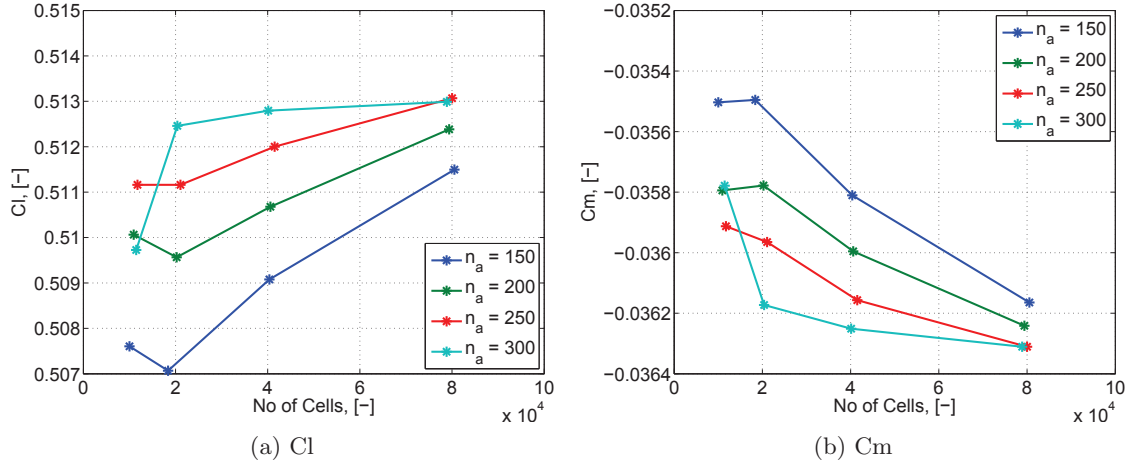


Figure 4.4: Grid Convergence Study: Results

As can be seen from the figures, the curves for different n_a tend to converge in case of the lift- and moment coefficient. Looking at the results of $N = 80\,000$, it can be seen that increasing the number of points on the airfoil reduces the difference in value of the lift- and moment coefficient. The highest two number of points on the airfoil even almost coalesce, thus negligible differences in these results are seen. With this analysis, it is decided to use the case of $n_a = 250$ in the remaining study. The lowest number of cells, $N \approx 10\,000$, yields in all cases a value which is not in line with the trend of the other results. This result is not taken into account in the following step.

In order to decide upon the total amount of cells in the domain, N , a Richardson extrapolation has been performed. More details about the theory and procedure of the Richardson extrapolation can be found in Slater [73]. The Richardson extrapolation extrapolates the output to an infinitesimal grid point spacing such that a comparison can be made with the obtained values for the lift coefficient. An overview of the values and percentual differences with the infinite value are shown in Figure 4.5.

The order of convergence is calculated as follows:

$$p_c = \frac{\ln(C_{l,1} - C_{l,2}) / (C_{l,2} - C_{l,3})}{\ln \sqrt{2}} = 0.68 \quad (4.23)$$

where $C_{l,i}$ is the lift coefficient for the i^{th} grid and p is the order of convergence. The expected convergence order, for the case where n_a is fixed and only the number of cells in j direction are varied, is around $p_c = 1$. The obtained order of convergence slightly deviates from this value, however this might be caused by a number of factors, such as: grid inaccuracies, turbulence modelling or imprecise grid refinement.

An overview of the computational times of the different grids is depicted in Figure 4.6. The figure clearly shows a linear correlation between the total number of cells and the computational time.

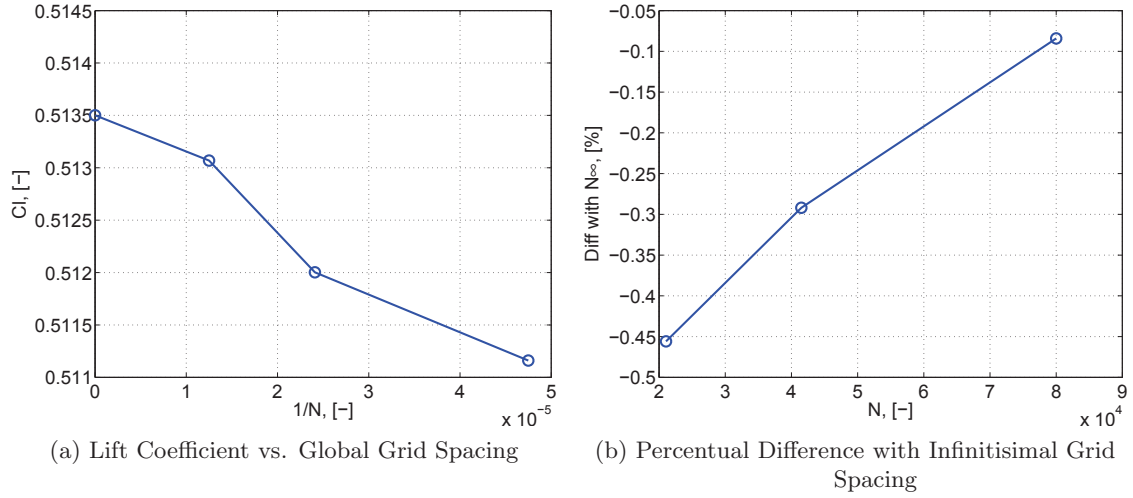


Figure 4.5: Richardson Extrapolation performed on the Results of the $n_a = 250$ Grids.

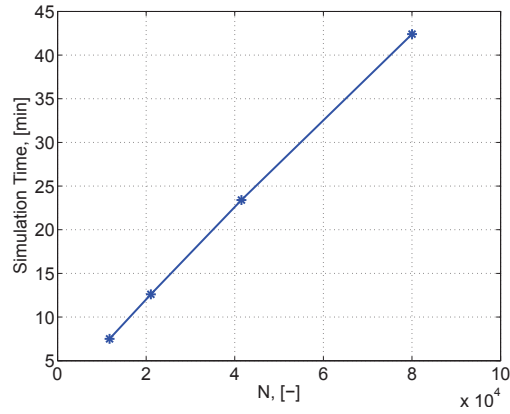


Figure 4.6: Simulation Time for the different Grids for $n_a = 250$.

Taking into account the accuracy and simulation time of the obtained results and the expected grid requirements in the transient simulations, it is decided to use the grid with the highest number of cells, $N \approx 80\,000$. Figure 4.5b shows that the computed lift coefficient is very close to the infinitesimal grid spacing value ($\delta Cl < 0.1$ [%]) and it is expected that such high accuracy would be necessary in the transient simulations. The final mesh is designed with the following parameters:

Table 4.3: Final Mesh Set-up

Parameter	Unit	Value
Number of Grid Points on Airfoil	[-]	250
Initial Cell Height	[m]	2×10^{-5}
Growth Rate	[-]	1.05
Domain Radius	[-]	80c
Number of Cells	[-]	$\approx 80\,000$

A graphical overview of whole domain of the mesh as well as a zoom of the airfoil in the centre of the domain is given in Figure 4.7.

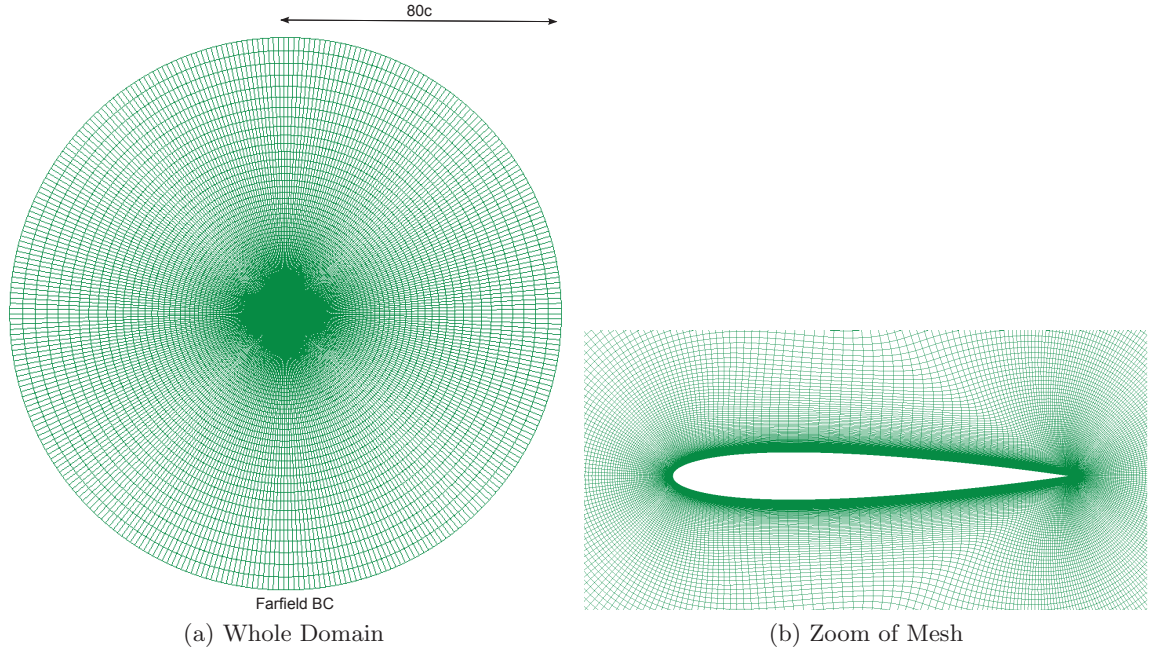


Figure 4.7: Mesh of the NACA-0012

4.3 Time Step Study

Now the grid set-up has been obtained in the previous section, a correct time step in the transient simulations has to be decided upon. This section describes the time step study to ensure a time step independent simulations. The mesh obtained in the previous section is used, a sinusoidal pitching motion similar to the motion at $U_\infty = 12.9$ [m/s] in the stall flutter experiment and the resulting force coefficients are compared at different time-steps. Firstly, the time step study set-up is described in this section and afterwards the results are presented and discussed. All simulations in the time step study were run on a 2.5 GHz Intel(R) Xeon(R) CPU E5-2670v2 processor with four cores.

4.3.1 Time Step Study Set-up

In order to ensure that the RANS model is able to show high angles of attack amplitude oscillations in the aeroelastic study, it is necessary to perform the time step study at high angles of attack amplitude as well. It is decided to force the NACA 0012 airfoil to undergo a similar motion as the motion of the NACA 0012 airfoil in the stall flutter experiment from Li [7] at $U_\infty = 12.9$ [m/s]. The following pitching motion is enforced:

$$\theta(t) = 44 \sin\left(\frac{2\pi}{1.26}t\right) \quad (4.24)$$

The enforced motion compared to the experimental motion is shown in Figure 4.8. The figure clearly shows that the experimental motion is not completely sinusoidal: the maxima and minima in the experiment are more pointed and the pitching velocity is higher in negative direction.

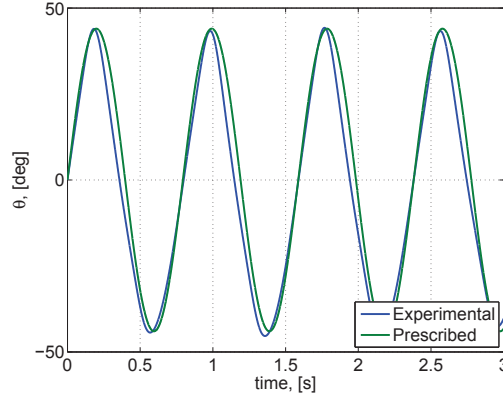


Figure 4.8: Prescribed Motion at $U_\infty = 12.9$ [m/s] for Time Step Study compared with Experimental Motion from Li [7].

An initial estimation for the time step for transient simulations of airfoils can be obtained in the criterion that at in the period of a vortex being shed at least 100 time-steps are taken. The period of a shed vortex is calculated with the *Strouhal*-number as follows:

$$f_v = \frac{St \cdot U_\infty}{c} \quad (4.25)$$

$$T = \frac{1}{f} \quad (4.26)$$

$$\Delta t = \frac{T}{100} \quad (4.27)$$

where $St = 0.2$ [-] is the Strouhal number, f_v is the vortex shedding frequency and T is the period of oscillation. This leads to a recommended time-step of $\Delta t = 1.2 \times 10^{-3}$ [s]. This value is simply to give an initial recommendation of the time step, further refinement is necessary in order to acquire a time independent solution. It is decided to use the time steps as shown in Table 4.4.

Table 4.4: Time Steps used in the Time Step Study

Parameter	Value, [s]
Time Step 1, Δt	1×10^{-3}
Time Step 2, Δt	5×10^{-4}
Time Step 3, Δt	2.5×10^{-4}
Time Step 4, Δt	1.25×10^{-4}

4.3.2 Time Step Study Results

The results of the time step study for the different time steps are shown in Figure 4.9. Time discretisation is done with a second-order backward-differencing scheme. A comparison is made with the experimental force coefficients in order to provide some preliminary insight in the abilities of the RANS model to capture the aerodynamics at the concerning high-amplitude oscillations. The motion of the airfoil is also included in the figures in order to relate the force behaviour to the motion. The left figures show the force coefficients and motion over the complete simulation time and the right figures shows the force coefficients at a single period of oscillation.

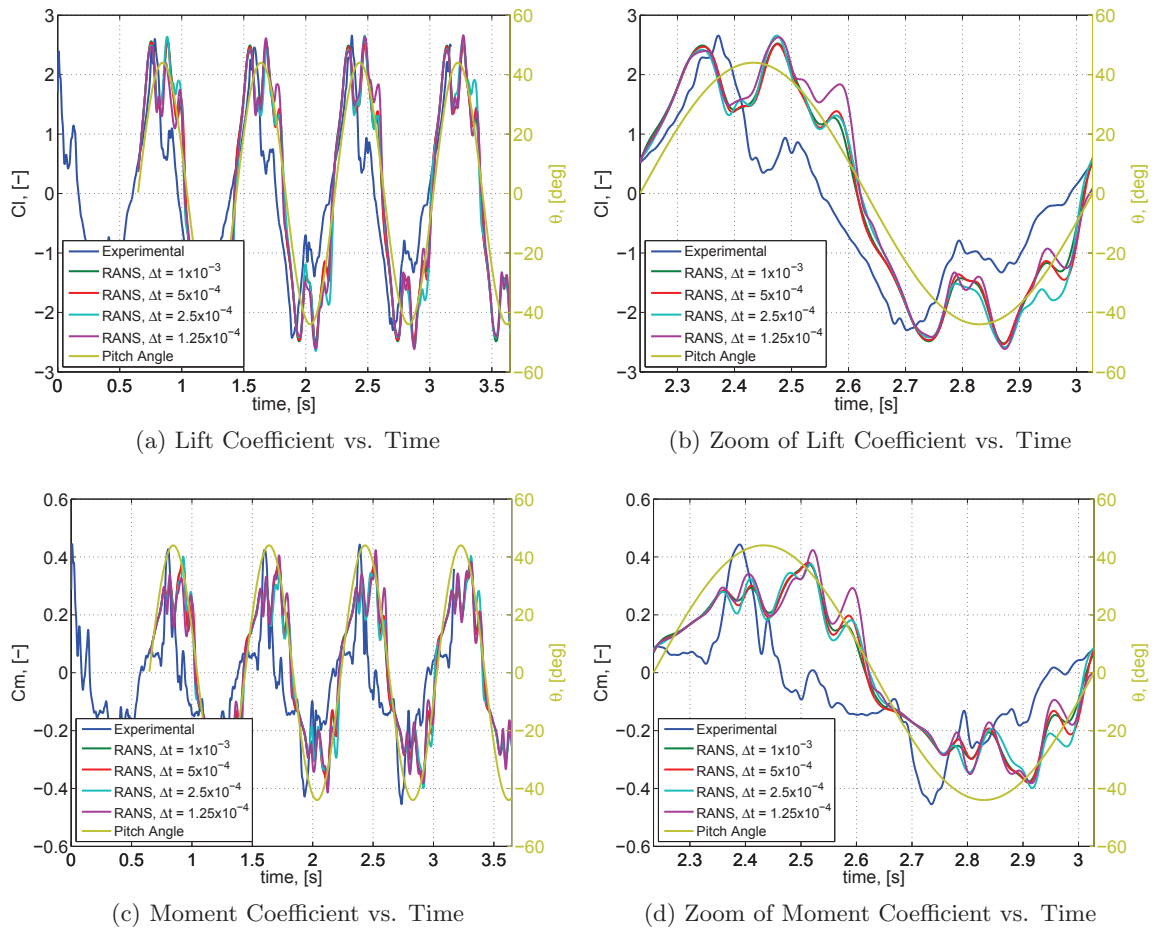


Figure 4.9: Time Step Study Results compared to Data from Li [7]

From the lift- and moment coefficient results, no clear discrepancies among the different time step results are apparent. Some cycle-to-cycle variation is observed in the experimental- and numerical- results especially for the smaller time steps. These variations might be caused by the turbulent nature of the fluid flow. However, the larger cycle-to-cycle variation at smaller time-steps also introduces the possibility that the flow has not quite settled yet. In order to give an impression of all physical quantities, their flow fields at a certain time are shown in Appendix G. As the simulations at all time

steps are numerically converged, the velocity-, pressure- and turbulence fields are properly resolved and the Courant number takes acceptable values (at the highest time-step, 90% of all cells are lower than $Co = 10$), it can be concluded that all time steps provide correct solutions of the fluid flow around a pitching airfoil. Therefore, it is decided that the largest time step, $\Delta t = 1 \times 10^{-3}$ [s], would be sufficient to perform the aeroelastic simulations. It must be said, in hindsight, that in order to improve numerical stability during the aeroelastic simulations, the time step might be susceptible to changes.

As the results are compared with the experimental results, a clear difference is seen in the form of a second peak in the numerical results which value is greatly overestimates the second peak in the experiment. This observation will be discussed in more detail in Section 5.1.

4.4 FSI Solver Set-up

This section describes the set-up of the FSI simulations in OpenFOAM of the airfoil which is free to move in two degrees of freedom. Initially, a rotating mesh was used for the FSI simulations. However, due to the large displacements of cells at the outside boundaries of the mesh, the simulations showed convergence difficulties. A solver including mesh deformation has been developed which eliminates the large displacements at the outside cells as the cells close to the airfoil are deformed and displaced.

The same method to obtain the motion of the airfoil as described in Section 3.2 is used in OpenFOAM. This means that the equations of motion are solved for the acceleration of the body in the new time-step. A schematic overview of the FSI-solver is given in Figure 4.10.

The following steps describe the solution procedure of the FSI-solver:

1. Boundary- & initial conditions, discretisation schemes, solver settings and flowfields are initialised.
2. The first FSI-iteration is set and the fluid (u & p) in the domain is solved for by means of RANS computations.
3. The forces acting on the airfoil are extracted and passed on to the structural solver.
4. A new position of the airfoil is obtained by solving the structural problem.
5. The mesh is deformed
6. The solution's FSI residual is compared with the FSI residual criteria. If the criteria is not reached, go to step 6, otherwise, go to step 8.
7. The amount of FSI iterations is compared to the maximum FSI iterations. If the maximum iterations is not yet reached, $n_{iter} = n_{iter} + 1$ and go to step 2, otherwise go to step 8.

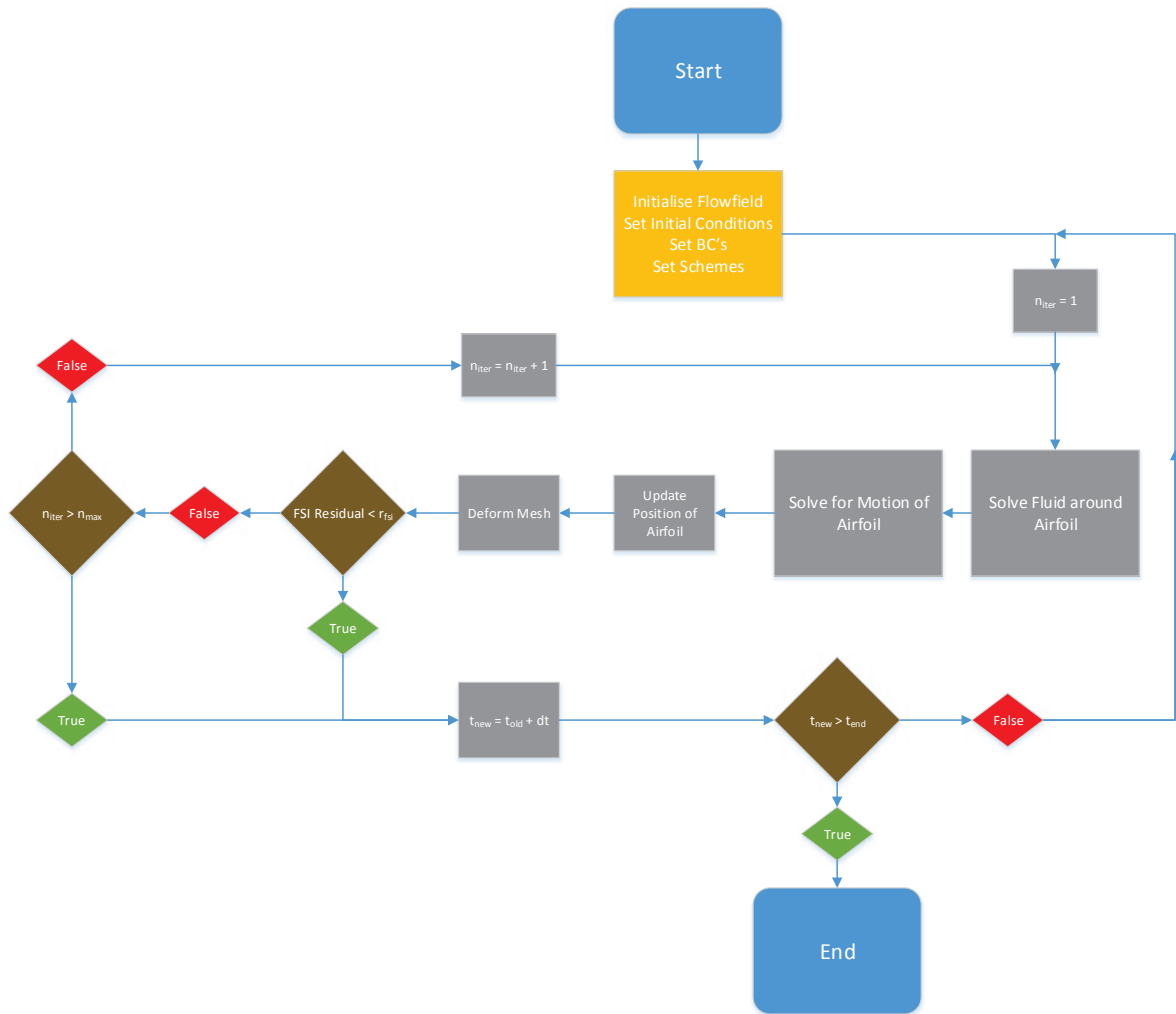


Figure 4.10: Flowchart of the FSI-Solver.

8. If the maximum simulation time is not reached, the mesh is deformed and the simulation procedure start over from step 2. Otherwise, the simulation is finished.

The coupling parameters of the FSI-simulations are shown in Table 4.5.

Table 4.5: FSI Coupling Properties

Parameter	Symbol	Value
FSI Coupling Scheme	-	Aitken
FSI Relaxation Factor - Initial	RF_0	0.9
FSI Relaxation Factor - Maximum	RF_{max}	0.99
FSI Relaxation Factor - Minimum	RF_{min}	0.1
FSI Residual	r_{fsi}	3×10^{-4}
Maximum FSI Iterations	n_{max}	20

4.5 Summary

This chapter has dealt with the second proposed model in the aeroelastic study of a wind turbine airfoil: i.e. the RANS model. The completion of this chapter has led to performing the second task as defined in Chapter 1: **Task 2.** *Design a reliable, accurate and efficient RANS model in OpenFOAM which is able to numerically simulate aeroelastic behaviour of an airfoil.* The RANS model set-up and validation as well as the theoretical principle in solving the Navier-Stokes equations by means of CFD computation have been discussed. A grid- and time-step independence study have been carried out respectively on a static airfoil and an airfoil pitching in a prescribed manner in order to ensure efficient and accurate simulations. An overview of the FSI model set-up used in the aeroelastic simulations has been provided. Now the RANS model design has been completed, the actual aeroelastic simulations on an airfoil can be performed. This is done in the next chapter.

Aeroelastic Simulations

Now the engineering- and RANS model have been designed in Chapter 3 and Chapter 4 and their aerodynamic- and structural parts have been validated individually, the aeroelastic capabilities of both models are validated and assessed. This chapter deals with the aeroelastic validation of the engineering- and RANS model by means of a comparison of the results with experimental data and is equivalent to performing the third task: **Task 3**: *Validate the models with experimental data of self-exciting high-amplitude limit cycle oscillations.* Carrying out this task will provide valuable information in answering the first research question: **1**. *Which numerical models are able to predict critical onset velocity and behaviour of self-exciting high-amplitude limit cycle oscillations of an airfoil?* The chapter is divided into four sections. In Section 5.1, a comparison of the aerodynamic forces obtained with a prescribed motion with the engineering- and RANS model in respectively Chapter 3 and 4 is made. Afterwards, in Section 5.2, both models are used in an attempt to reproduce the stall flutter experiment results from Li [7] by means of aeroelastic analyses. Section 5.3 deals with the validation of the aeroelastic simulations of both models on the flutter experiment from Veilleux [8]. Lastly in Section 5.4, to conclude this part, a discussion of the results and findings obtained in this chapter is done.

5.1 Engineering- and RANS model Prescribed Motion Comparison

In this section, the first direct comparison between the aerodynamic abilities of the engineering- and the RANS model is made. The force coefficients as a result of the prescribed motion at $U_\infty = 12.9$ [m/s] obtained respectively in Section 3.4 and Section 4.3 are compared to the experimental data in Figure 5.1. RANS model results of the largest time-step, $\Delta t = 1e^{-3}$ are used in the comparison. The left figures show the force coefficients over several periods of oscillation, the figures in the middle show the force coefficients over one period of oscillation and the right figures show the force coefficients over the pitch angle. The mean with the corresponding standard deviation of the force coefficient are respectively indicated by the solid and the dashed line.

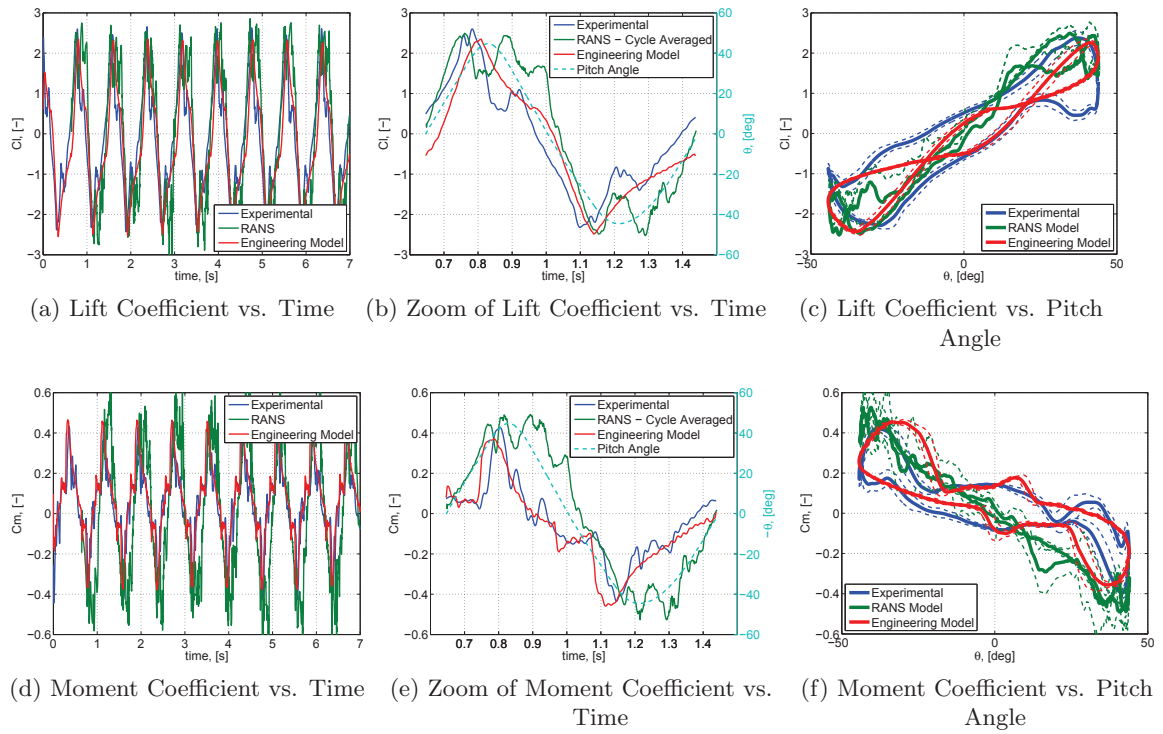


Figure 5.1: Force Coefficients Responses obtained with the Engineering- and RANS Model on a prescribed Motion compared with Experimental Data from *Li* [7].

It can be seen that there are some discrepancies between the results of the numerical models and the experimental data. In order to be able to explain why these discrepancies exist, the results of both numerical models are investigated more deeply. The contributions to the different force coefficients computed in the engineering model as described in Section 3.1 are looked into in the following subsection. Afterwards, the flow behaviour of the RANS model at different time-steps are looked into and the relation between the flow fields and the force development is described.

5.1.1 Prescribed Motion Results of Engineering Model

This part discusses the aerodynamic capabilities of the engineering model obtained with a prescribed motion into more detail. As explained in Chapter 3, the total, dynamic lift- and moment coefficients consist of several contributing terms. In order to be able to assess the ability of the engineering model to actually capture the aerodynamic forces at these high-amplitude oscillations, it is important to understand how these contributing terms behave over time. Figure 5.2 shows the contributions of the different terms to the lift- and moment coefficient as respectively described by Equation 3.9 and 3.13. The lift- and moment coefficients are indicated by the green lines, the contributing terms are indicated with the dashed lines and the experimental data is shown in blue and is added as a comparison.

Looking at the lift coefficient contributions, it easily can be seen that the contribution of the non-circulatory lift coefficient, Cl_{NC} , is very small compared to the rest. The lift

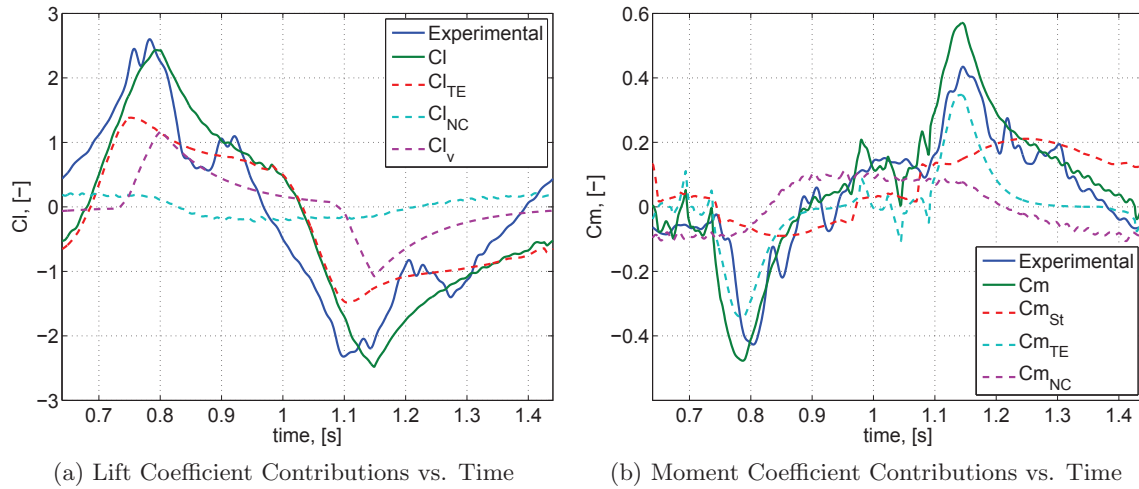


Figure 5.2: Force Coefficients Contributions obtained with Engineering Model compared with Experimental Data from Li [7].

contribution due to the leading edge vortex, Cl_V , clearly shows a peak around shortly before the maximum pitch angle. Afterwards this contribution decreases slowly as the 'artificially introduced vortex' detaches and travels over the airfoil until the next vortex starts to build strength. The major contribution to the lift is caused by the unsteady lift coefficient due to the effect of TE separation, Cl_{TE} . This term greatly determines the phase of the dynamic lift coefficient which can be seen by the 'delay' of the lift coefficient after maximum pitch angle is reached.

The Cl_{TE} contribution can be further divided into two terms as seen in Equation 3.9: an attached contribution, $Cl_{TE,a}$, and a fully separated contribution, $Cl_{TE,fs}$. The contributions of these terms are shown in Figure 5.3. The figure clearly shows that the two terms contribute to the TE lift coefficient in an alternating fashion: during the attached phase, the $Cl_{TE,a}$ dominates the TE lift coefficient value and the $Cl_{TE,fs}$ -contribution is significantly lower. When the airfoil reaches higher angles of attack the $Cl_{TE,a}$ -term tends to go to zero and the $Cl_{TE,fs}$ -contribution increases due to the upstream motion of the dynamic separation point. This increase continues even after a maximum angle of attack is reached, during the pitching down motion, until the separation point moves away from the LE

The engineering model is capable of reproducing the general trend of the lift coefficient at these high-amplitudes of motion. However, the dynamics of shedding the LEV and reattachment of the flow afterwards, denoted by the drop in lift after the first peak and the appearance of a second smaller lift peak in the experimental results, is not fully captured by the engineering model.

When the contributions of the moment coefficients are compared it can be observed that the static moment contribution, Cm_{St} , and the non-circulatory moment contribution, Cm_{NC} , merely determine the phase and contribute slightly to the overall value. The peaks observed in the experiment and simulations are caused by the unsteady moment

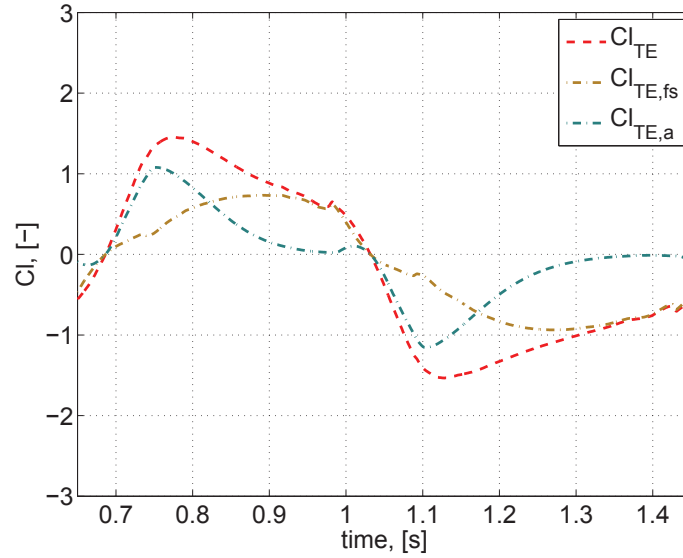


Figure 5.3: Dynamic TE Separation Contribution to the Lift Coefficient vs. Time.

due to the dynamic TE separation, Cm_{TE} . These high values are caused by the fact that Cm_{TE} is directly related to the value of the dynamic lift coefficient through Equation 3.14.

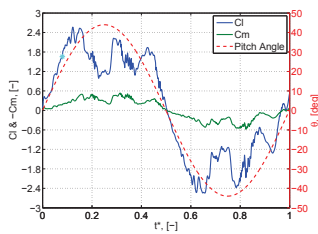
The obtained results with the engineering model on a prescribed motion provide confidence that the model is able to perform aeroelastic simulations on a 2D airfoil and produce flutter behaviour. Validation of the aeroelastic engineering model is done in Section 5.2 and Section 5.3.

5.1.2 Prescribed Motion Results of RANS Model

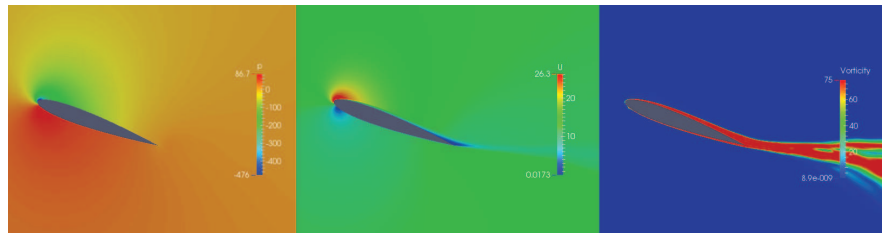
In this section, the aerodynamic forces obtained on a high-amplitude prescribed motion with the RANS model are looked into. As already observed in the introductory part of this section, the lift- and moment coefficients are, for a majority of the oscillation, overpredicted by the RANS model. A tentative explanation is found here by means of visualisation of the flow fields around the airfoil compared with force coefficients. This is done in Figure 5.4. On the left, the force coefficients and pitching motion over time are shown. The cyan coloured dot indicates the non-dimensional time, t^* at which the pressure-, velocity- and vorticity fields are shown on the right.

Analysing the figures, it can be seen that during the upward pitching motion, a vortex develops at the leading edge and builds up strength. When the vortex reaches its maximum strength, at $t^* = 0.12$, the maximum lift coefficient is seen. At a certain point, while still in upward pitching motion, the vortex is shed from the leading edge and a trailing edge vortex (TEV) is being developed which lead to a rapid decline in lift coefficient as seen at $t^* = 0.18$ and $t^* = 0.23$. When the maximum pitch angle is reached the lift coefficient starts to increase as the TEV detaches. At $t^* = 0.29$, after the maximum pitch angle is reached, a second peak in lift coefficient is obtained with the RANS simulations directly

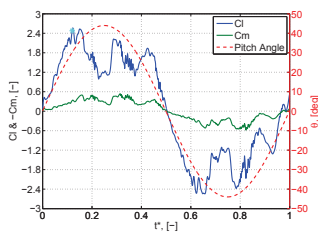
due to the complete detachment of the TEV. Afterwards, at $t^* = 0.38$, while pitching down, a trailing edge vortex is created and the lift coefficient decreases. When the TEV is shed from the surface of the airfoil a third, lower peak in lift coefficient is observed. Afterwards, the airfoil reaches pitch angles in the linear region and the flow reattaches to the surface which leads to a linear decrease of lift coefficient until the process start all over again at negative pitch angles.



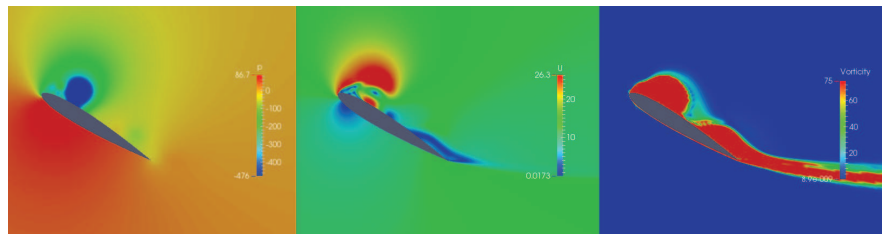
(a) C_l , C_m & θ vs. Time



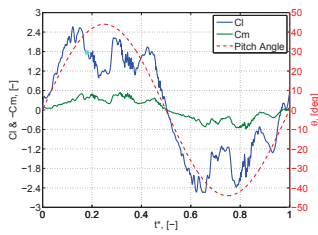
(b) Pressure, Velocity & Vorticity Fields at $t^* = 0.08$



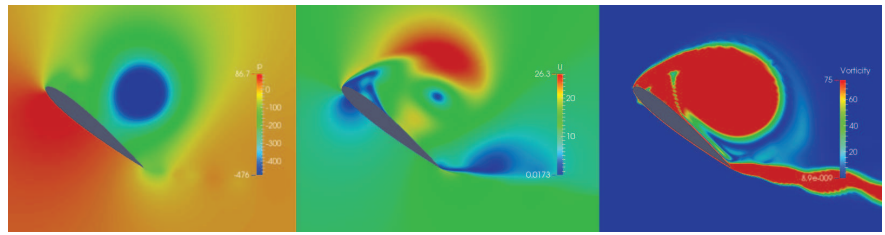
(c) C_l , C_m & θ vs. Time



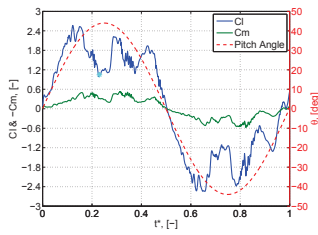
(d) Pressure, Velocity & Vorticity Fields at $t^* = 0.12$



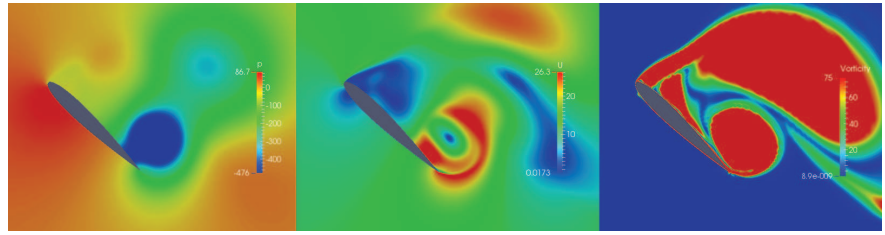
(e) C_l , C_m & θ vs. Time



(f) Pressure, Velocity & Vorticity Fields at $t^* = 0.18$



(g) C_l , C_m & θ vs. Time



(h) Pressure, Velocity & Vorticity Fields at $t^* = 0.23$

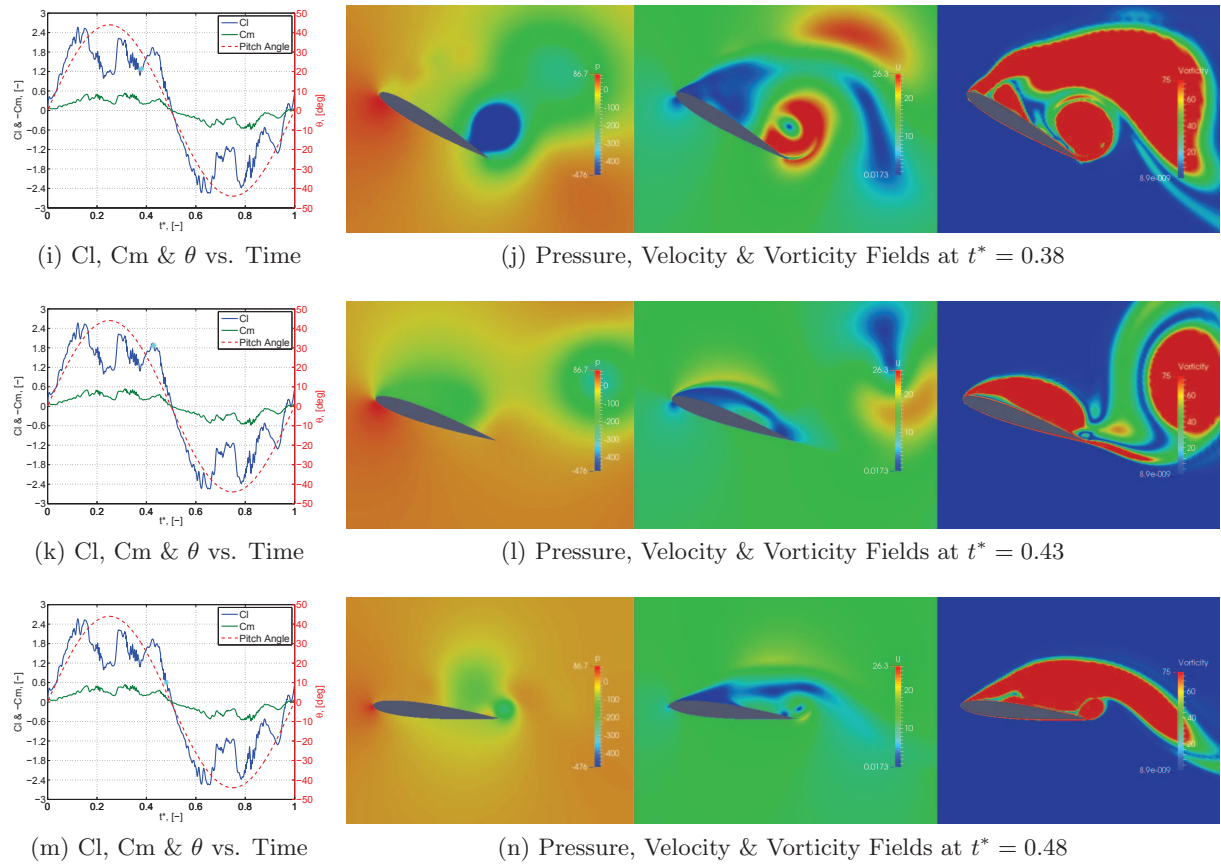


Figure 5.4: Prescribed Motion Results obtained with the RANS Model at $U_\infty = 12.9$ [m/s].

Figure 5.5 provides a detailed overview of the pressure- velocity- and vorticity fields including the velocity vectors at $t^* = 0.12$. In the figure, the recirculation area indicated by the clockwise oriented arrows around an epicentre indicates the LEV.

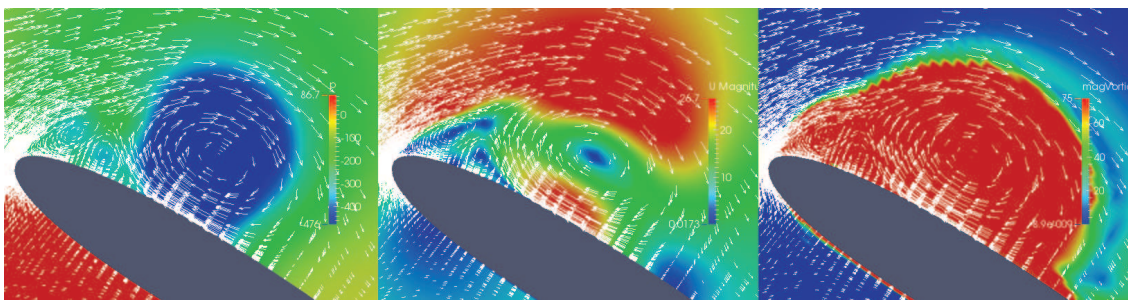


Figure 5.5: Velocity Vector Plots on the Pressure, Velocity & Vorticity Fields at $t^* = 0.12$.

From the analysis on the results obtained with the prescribed simulations with the RANS model, the following important observations are made regarding force prediction of a high-amplitude oscillating NACA 0012 airfoil by a RANS model:

- With an increasing pitch angle up to a first peak in lift coefficient, the RANS model accurately predicts the lift coefficient values as seen in the experiment from Li [7].

Values of lift coefficients around a factor 3 times greater than the static lift at similar angles of attack due to the dynamic stall effect are observed in both results.

- Two additional peaks in lift are furthermore created by the RANS model due to separation of the TEVs. However, compared to the experimental data, their influence on the force coefficients seem to yield an overprediction.
- The overprediction of the force coefficients might lead to a lag in the motion in the aeroelastic simulations performed in the next two sections.

5.2 Aeroelastic Results of NACA-0012 from Li [7]

This section deals with the capability of the engineering- and RANS model to reproduce the results from the stall flutter experiment from Li [7] by means of aeroelastic simulations. At freestream wind speeds used in the experiment, the airfoil is given an initial pitching velocity similar to the ones seen in the experiment. In case of the self-excitation seen in the experiment at high velocities $U_\infty > 10$ [m/s], both models are still given an initial pitching velocity. For the RANS model, this is done to decrease simulation time and for the engineering model, this is done to provide a direct comparison and because it was found that the initial condition did not influence the resulting behaviour of the airfoil.

5.2.1 Results with original Non-Linear Damping

In this part, the structural parameters, including the non-linear damping formulation, from Table 3.5 are used as an input in both models and the grid and time-step obtained in Chapter 4 are used in the simulations by the RANS model.

At first a comparison is made between the models and experimental data at wind-off conditions, $U_\infty = 0$ [m/s]. For the engineering model, this has already been shown in Chapter 3. However, an interesting comparison in the structural model of both numerical models can be made now. The resulting response at wind-off conditions compared to the experimental motion are shown in Figure 5.6. Both responses obtained numerically show a very similar decaying motion. Comparing the numerically obtained amplitudes of motion to the experimental one, also similar values can be seen. However, the frequency obtained with the numerical models is lower than the experimental frequency.

Now for a variety of wind speeds, the aeroelastic simulations are performed. The results at three distinct wind speeds, $U_\infty = 3.9, 12.9$ and 16.3 [m/s], are shown respectively in Figure 5.7, 5.8 and 5.9.

The results at $U_\infty = 3.9$ [m/s] in Figure 5.7 show that the motion of the decaying response is rather similar to the experimental data. Equal amount of oscillations are observed with slightly underestimated pitch amplitudes. The numerically obtained lift coefficients are similar to the experimental results in amplitude on positive pitch angles, however a delay of the lift coefficient is apparent. The moment coefficient over time is substantially underestimated by both models. The high values seen in the RANS model results at the start of the simulation can be disregarded, these are due to the projection of the steady

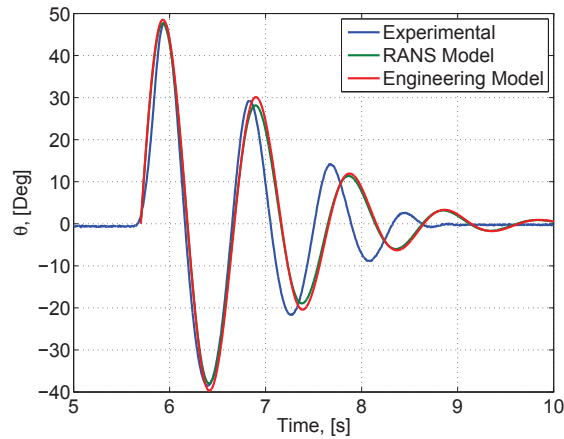


Figure 5.6: Motion Response at $U_\infty = 0$ [m/s] obtained with Engineering- and RANS Model compared with Experimental Data from *Li* [7].

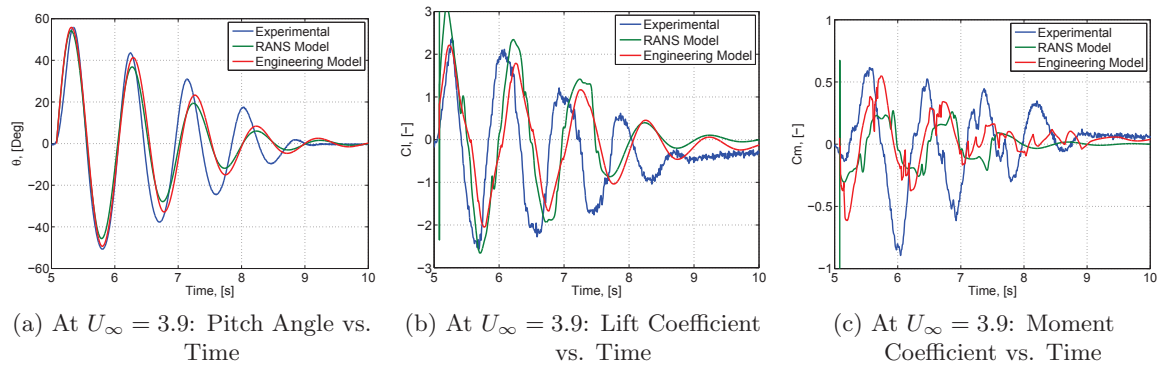


Figure 5.7: Motion Response and Force Coefficients at $U_\infty = 3.9$ [m/s] obtained with the Engineering- and RANS Model compared to Experimental Data from *Li* [7].

state solution on the starting solution of the transient simulations in OpenFOAM.

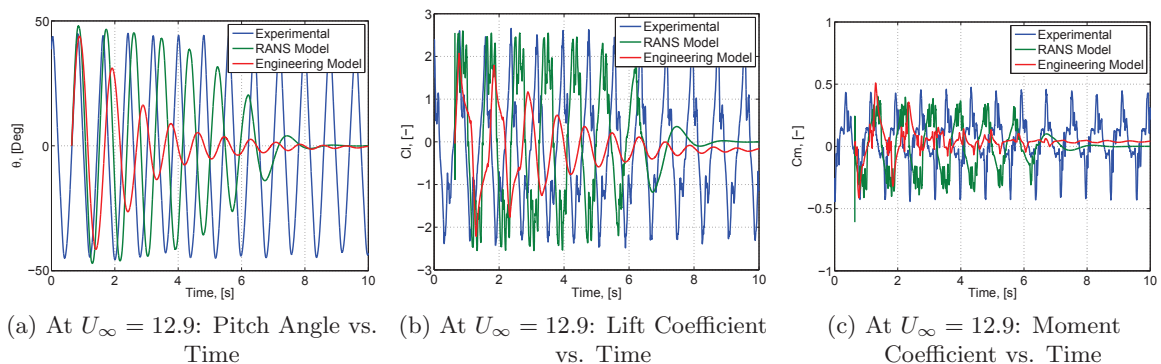


Figure 5.8: Motion Response and Force Coefficients at $U_\infty = 12.9$ [m/s] obtained with the Engineering- and RANS Model compared to Experimental Data from *Li* [7].

The obtained results at $U_\infty = 12.9$ [m/s] in Figure 5.8 show a decaying motion response for both numerical models while in the experiment, LCOs with high amplitudes are observed. Despite the fact that in the first oscillation(s) high lift- and moment coefficient values are obtained, apparently insufficient energy is added from the fluid to the structure to sustain the LCOs.

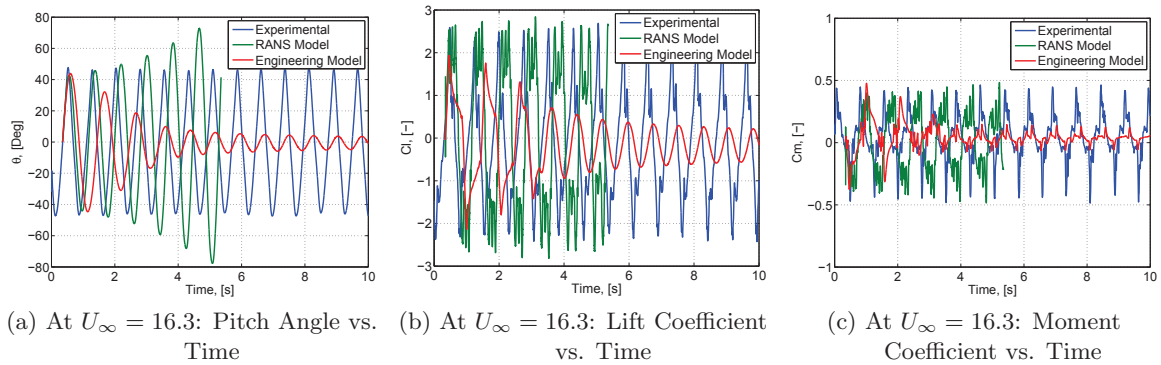


Figure 5.9: Motion Response and Force Coefficients at $U_\infty = 16.3$ [m/s] obtained with the Engineering- and RANS Model compared to Experimental Data from Li [7].

Looking at the results obtained numerically at $U_\infty = 16.3$ [m/s] shown in Figure 5.9, clearly different responses of the engineering- and RANS model are observed. The engineering model results show a decrease of the pitch amplitude until LCOs are obtained with an amplitude of around $\theta_{amp} = 5^\circ$. Compared to the experimental LCOs, the amplitude is significantly smaller and the motion remains in the linear region of the force coefficient curves. Interesting to note is that when the LCO region is reached, the frequency of oscillation coincides with the experimentally observed frequency. At even higher wind speeds, a slight increase in pitch amplitude is observed. This happens until the divergence speed is reached at which the airfoil undergoes divergence.

The RANS model on the other hand, does not show LCOs, but shows divergence of an oscillating motion until the simulation is aborted due to errors. Despite the fact that the lift- and moment coefficients take very similar values as seen in the experiment, no LCOs are produced.

Several conclusions can be drawn from reproducing the results of the experiment from Li [7] with the two numerical models. The results of the aeroelastic simulations performed by the RANS model showed that no LCOs are obtained in the whole range of wind speeds: at the lower wind speeds a decaying motion is seen and at a certain wind speed the motion of the airfoil diverges in an oscillating manner. Comparing the force coefficients with the experimental ones, great similarity is observed, especially considering the maximum values in the first oscillations. This introduces some doubts in the already uncertain structural parameters used in the experiment.

Regarding the engineering model, it can be stated that at wind speeds where LCOs are expected, not enough energy is transferred from the fluid to the structure in order to excite the system and produce high-amplitude LCOs. The uncertain structural- and aerodynamic damping values in the experiment might play an important role in this

as experience has taught that the engineering model is very sensitive to the damping coefficient in the reproduction of the results from this particular experiment. In order to investigate the sensitivity of the engineering model to the non-linear damping values, the non-linear damping is varied and the motion responses and force coefficients are observed in the next section.

5.2.2 Results with adapted Non-Linear Damping

In order to improve the accuracy of reproducing the experimental results with the engineering model, several structural parameters have to be reconsidered. In order to find out whether the cause of the engineering model not producing LCOs lies in the approximation of the non-linear structural damping, the damping is varied in this part and the aeroelastic response is checked. It is decided to reduce the non-linear damping, as described by the formulation shown in Table 3.5, by a factor 3 and introduce a cubic damping coefficient at high angles of attack. The resulting motion and force coefficients responses are shown in Figure 5.10.

The figures clearly show that with a lower non-linear damping and the cubic damping at high angles of attack LCOs do occur at higher wind speeds. The low wind speed case, at $U_\infty = 3.9$ [m/s], shows that the response still decays, albeit at a lower rate. The lower rate is a logical effect of the lower structural damping.

An overview of the most relevant results are shown in Figure 5.11. Regarding the mean pitch amplitudes, the negative pitch amplitudes show very similar values as the experimental ones. However, the positive pitch amplitudes decrease while the experimental amplitudes increase. Looking at the frequency, it can be seen that the numerical frequencies are estimated lower than the experimental ones. Furthermore it shows an opposing trend: while the experimental frequency increases with wind speed, the numerical frequency decreases. However looking at the reduced frequency in Figure 5.11c, a similar trend of the numerical- and experimental results is observed. Only tentative explanations are given as why these discrepancies are observed. First of all, the uncertainty in the non-linear structural damping might play a role in the observed differences/ Furthermore, the fact that the heave motion is not excited in both numerical models might influence the behaviour in pitch as well. Finally, the fact that during the experiment, the windings of the springs sometimes were touching each other leads to behaviour which can not be captured by the numerical models.

5.2.3 Discussion

In principle, it can be concluded that the engineering model including the modified version of the Risø dynamic stall model is able to numerically predict high-amplitude LCOs when given a detailed quantification of the (non-linear) damping and other structural parameters. However, this section proves that the engineering model is very sensitive to the damping coefficient which is a critical parameter and difficult to accurately define in these types of simulations. As the RANS model showed to be capable of accurately

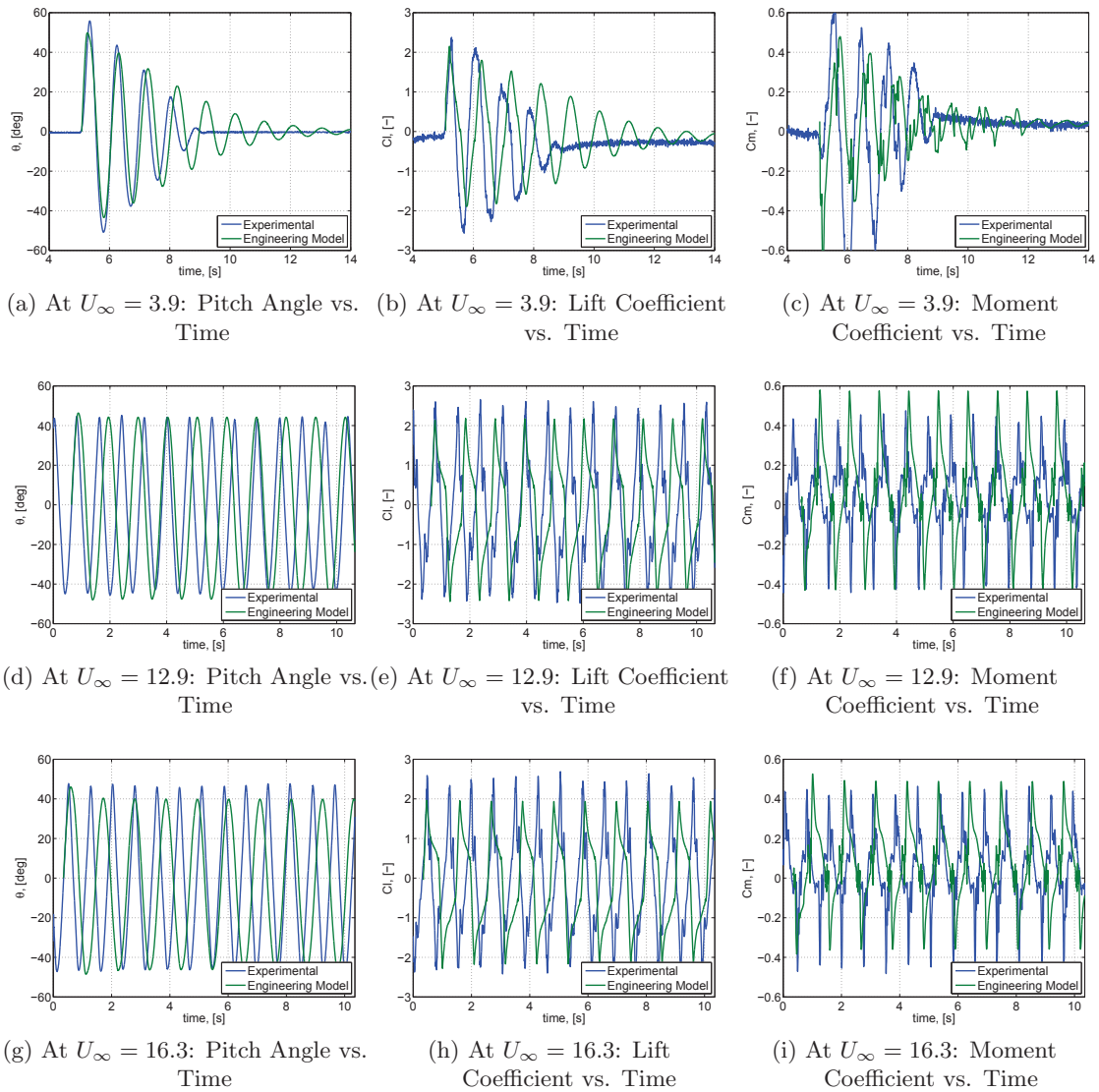


Figure 5.10: Motion Response and Force Coefficients of the Engineering Model with adapted Non-linear Damping compared to Experimental Data from Li [7].

reproducing the forces in the first oscillations at different wind speeds, it is believed that the aforementioned hypothesis is also true for the RANS model. In order to prove this statement, aeroelastic simulations with the engineering- and RANS model are compared to data from a similar experiment, described in Section 2.5, on a NACA 0012 wing in the next section.

5.3 Aeroelastic Results of NACA-0012 from Veilleux [8]

This section deals with the aeroelastic numerical simulations of the engineering- and RANS model compared to the results on the NACA-0012 classical flutter experiment from

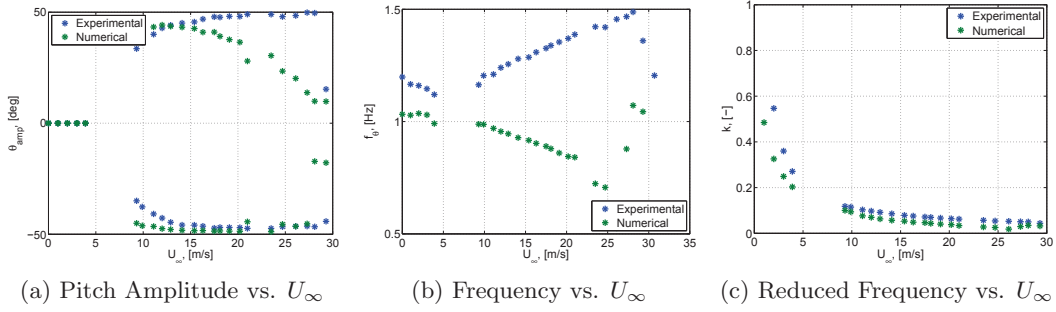


Figure 5.11: Bifurcation Diagram and Frequencies for different Wind Speeds obtained with the Engineering Model with modified Non-linear Damping compared to Experimental Data from Li [7].

Veilleux [8] mentioned in Section 2.5. In the experiment, an initial heaving velocity was given to the airfoil to initiate the response at a certain (rather limited) range of freestream wind speeds ($Re = 65\,000 - 85\,000$). In the numerical simulations a broader range of Reynolds number ($Re = 50\,000 - 120\,000$) is used as these results can be compared with RANS simulation from Veilleux [8] on the same experiment. This section firstly describes the structural parameters of the experiment. Secondly, the main results of the numerical models are compared to the data from Veilleux [8]. Afterwards, typical behaviour over time of both numerical models for several Reynolds numbers are presented and their performance is evaluated.

5.3.1 Structural Parameters

An overview of the structural parameters of the experimental set-up as described in Veilleux [8] is given in Table 5.1. These parameters are given as an input in the engineering- and RANS model to perform the aeroelastic simulations. It must be said that the heave damping coefficient was assessed by Veilleux [8] to have some sort of non-linear behaviour, but he concluded that introducing the non-linearity in his RANS simulations did not effect the results whatsoever. Note that several structural parameters are considered per unit length. As in the experiment, the pitching mass did not participate in the heaving direction and vice versa, the equations of motion as displayed in Equation 2.2 and 2.3 become:

$$m_h \ddot{h} + S \ddot{\theta} + c_h \dot{h} + k_h h = -L \quad (5.1)$$

$$S \ddot{h} + I_{rc} \ddot{\theta} + c_\theta \dot{\theta} + k_\theta \theta = M \quad (5.2)$$

where m_h is the mass in heave direction and where $S = m_p l \cos \theta$ is the static mass moment with the mass in pitch m_p .

5.3.2 Aeroelastic Results Comparison

The resulting pitch- and heave amplitudes of the oscillations as well as a non-dimensionalised frequency over the whole of Reynolds numbers compared to experimental data and RANS

Table 5.1: Experiment Structural Parameters from Veilleux [8]

Parameter	Symbol	Unit	Value
Chord	c	[m]	0.156
Span	S	[m]	0.61
Total Torsional Spring Stiffness	k_θ	[Nm/rad]	0.3
Total Compression Spring Stiffness	k_y	[N/m]	1484 & 800
Centre of Rotation	x_{RC}	[%]	18.6
Centre of Gravity	x_{CG}	[%]	28.6
Moment of Inertia around the C.R.	I_{RC}	[kg · m ²]	0.00135
Mass - Heave	m_h	[kg]	2.5
Mass - Pitch	m_p	[kg]	0.77
Torsional Damping Coefficient	C_t	[N · s/rad]	0.002
Heaving Damping Coefficient	C_y	[N · s/m]	2.0
Initial Heaving Velocity	$V_{h,0}$	[m/s]	0.6

simulations with the S-A turbulence model from Veilleux [8] are shown in Figure 5.12. The non-dimensionalised frequencies in case of a decaying response is also added in order to give an impression of its difference with a LCO motion's frequency.

First, the results of the RANS model are looked into. It can be seen from the figure that the RANS model predicts initiation of LCOs at $Re = 70\,000$, which is around $\frac{70\,000 - 60\,000}{60\,000} \approx 8\%$ higher than the onset Reynolds number found in the experiment. However, in the case of LCOs, the magnitude of amplitudes in pitch- and heave direction are captured very accurately. After an initial increase of LCO amplitude with an increasing Reynolds number, a drop in amplitude at $Re = 120\,000$ is observed in both RANS models. It is believed by the author that this might be caused by the fact that the LEV is shed more rapidly. A more in-depth analysis is made in the next section.

Now, the responses of the aeroelastic simulations of the engineering model, denoted by the red curves in Figure 5.12, are looked into. It can be seen that the same critical onset Reynolds number, albeit with a different amplitude, is predicted by the engineering model as in the experiment. This is considered an important characteristic, as in the parametric study on aeroelastic behaviour of the wind turbine airfoil, the critical onset velocity is the most critical output to be studied. Comparing the amplitude of LCOs, it is easily seen that the engineering model tends to yield an overprediction. This overprediction becomes especially clear in the heaving amplitude. While both RANS models predict a decrease in heave amplitude, the engineering model's heave amplitudes keeps on increasing. A potential cause for this is the high sensitivity of the engineering model to the damping coefficient as seen in the previous section together with the fact that the heaving damping coefficient behaves in an uncertain non-linear fashion.

In order to provide some insight in the simulation times to acquire a real time response of 10 [s] of all cases, an overview is given in Table 5.2. The aeroelastic simulation of $Re = 90\,000$ was performed on a different CPU than the other ones: a 2.27 GHz *Intel(R) Xeon(R) CPU E5520* on four processors. It can easily be seen that the simulation time of the engineering model are almost negligible compared to the RANS model's simulation

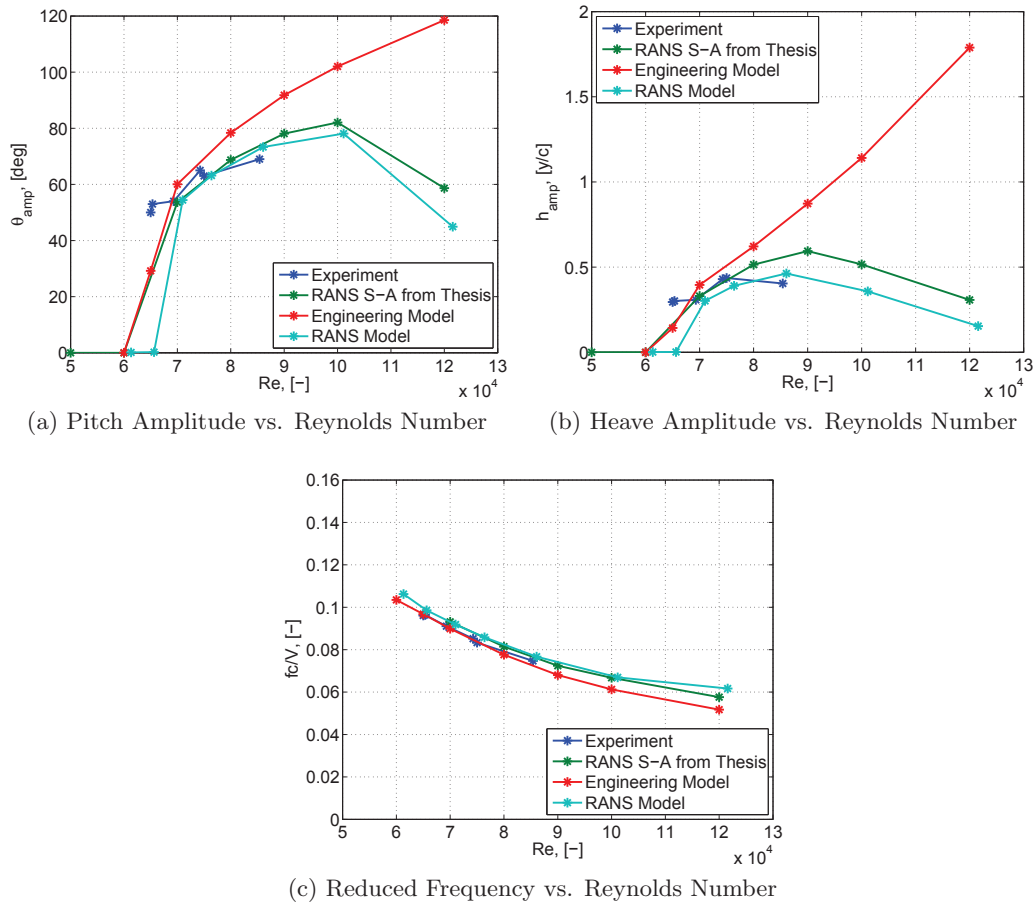


Figure 5.12: Pitch Amplitudes of LCOs obtained with Engineering- and RANS Model compared with Data from Thesis and Experiment from *Veilleux* [8].

time.

Table 5.2: Simulation Time of the Engineering- and RANS model of 10 [s] Real Time Response.

Re	Simulation Time		
	Engineering, [s]	RANS, [s]	RANS, [h]
60 000	20	193 885	54
70 000	20	509 902	142
90 000	20	919 850	256
100 000	20	602 878	167

Now a general insight has been obtained in the behaviour response of the airfoil, a more deeper understanding of the responses predicted by the engineering- and RANS model is obtained in the next part.

5.3.3 Aeroelastic Responses over Time

The motion responses over time obtained with the two models at different Reynolds numbers are shown in Figure 5.13. Unfortunately, no data is publicly available on the motion or forces over time of the experiment from Veilleux [8].

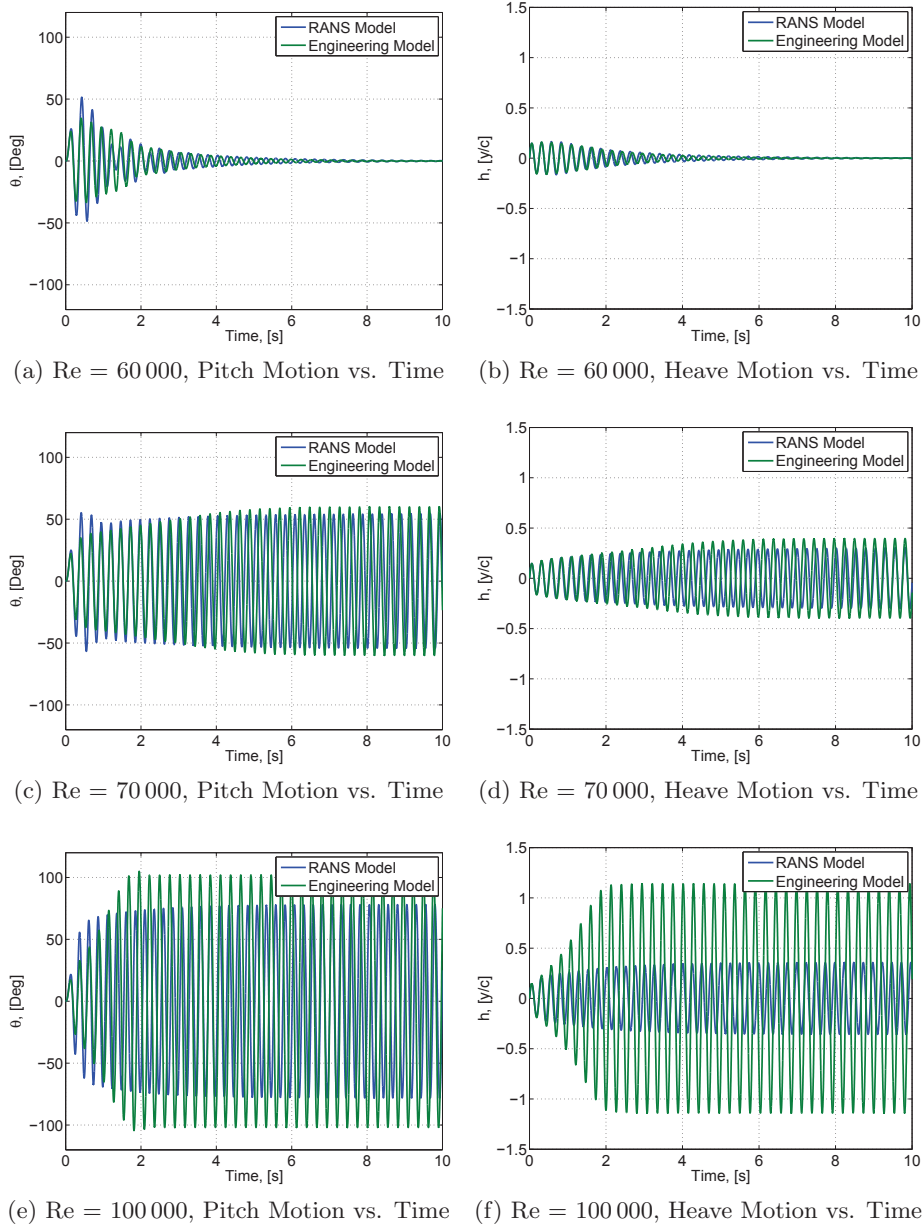


Figure 5.13: Pitch- and Heave Motion Responses obtained with the Engineering- and RANS Model

Comparing the motions of the two models at $Re = 60\,000$ and $70\,000$, it is seen that they produce very similar results regarding the amplitude and frequency of motion. At higher Reynolds numbers, the engineering model's motion amplitudes continues to in-

crease while the RANS model's amplitude levels off and eventually decreases. As stated before, this might be caused by the uncertain non-linear damping or by the fact that the engineering model does not fully capture the physics involved in the shedding of the LEV.

Looking into the force coefficients at $Re = 70\,000$, where the motion response obtained with both models are quite similar, some interesting observations can be made. The lift coefficient over time and over the pitch angle are depicted in Figure 5.14.

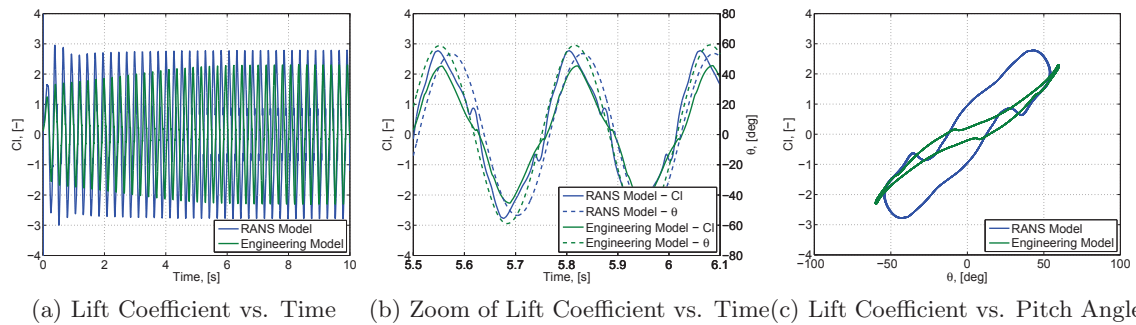


Figure 5.14: Lift Coefficient Response obtained with the Engineering- and RANS Model at $Re = 70\,000$.

It can be seen that the lift coefficient over time obtained by the two models show similar trends as indicated by the solid lines in Figure 5.14b. However, the maximum lift coefficients are somewhat underestimated by the engineering model and the frequency is lower as well. It can also be seen that the RANS model shows a phase difference in lift coefficient and pitching moment (indicated by the blue lines) while the engineering model results show to be in-phase (indicated by the green lines). This difference in phasing is clearly seen in Figure 5.14c, as the engineering shows a ‘sharp’ point indicating the in-phase behaviour, while the RANS model shows a ‘round’ development at high pitch angles. The RANS model shows a clear decrease after the maximum pitch angles is reached after which a smaller second peak is observed similarly to the observation made in experiment from Li [7]. This provides an indication of the fact that the typical dynamic stall phenomenon, characterised by the drop and the second peak in lift coefficient, occurs at these high-amplitude LCOs as well and that the RANS model is able to capture the physics involved.

In order to provide a tentative explanation for the decrease in pitch amplitude at $Re = 120\,000$ obtained by the RANS model, the lift coefficient is further looked into. Figure 5.15 shows the lift coefficient over the pitch angle for a range of Reynolds numbers. An interesting difference between the results is that the slope of the lift coefficient after a maximum lift coefficient is reached at $Re = 120\,000$ is much steeper than at lower Reynolds numbers. This indicates that there is a large drop in lift coefficient in a narrow range of pitch angles, which is caused by the rapid shedding of the LEV. It is believed that this phenomenon limits the growth of amplitude at this particular Reynolds number.

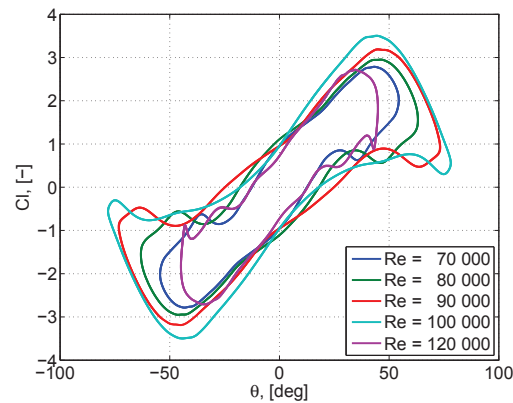


Figure 5.15: Lift Coefficients over Pitch Angle obtained with the RANS Model at Different Reynolds Numbers.

5.3.4 Discussion

This section dealt with the validation of the aeroelastic capabilities of the engineering- and RANS model by means of a comparison with experimental data from Veilleux [8]. It has been observed that both models are capable of producing high-amplitude LCOs with their own advantages and disadvantages. The engineering model proves to be a fast and efficient method of obtaining the critical onset wind speed accurately. However, due to its sensitivity for certain structural parameters such as the damping coefficient combined with uncertainty of this parameter in the experiment, the amplitude of the LCOs are substantially overestimated at high Reynolds numbers. The RANS model shows to be able to reproduce LCOs with very similar amplitudes seen in the experiment. However, the critical onset Reynolds number is slightly overestimated. A major drawback of the RANS model is its high simulation time.

5.4 Summary

This final section provides an overview of the most important observations made and conclusions drawn in this chapter. This chapter has dealt with the validation and the assessment of capabilities of the engineering- and RANS model to perform aeroelastic simulations. These are related to third and fourth task as defined in Section 1.2, which are **Task 3:** *Validate the models with data of self-exciting high-amplitude limit cycle oscillations of experiment.* and **Task 4:** *Compare the efficiency, reliability and accuracy of the numerical models.* Performing both tasks in this chapter yields answers to the first research question: **1.** *Which numerical models are able to predict onset and behaviour of self-exciting high-amplitude limit cycle oscillations of an airfoil?*

Aeroelastic validation of the engineering- and the RANS model has been done by means of a comparison with data from a two experiments on a NACA0012 which showed high-amplitude limit cycle oscillations: a stall flutter experiment from Li [7] and a coalescence

flutter experiment from [Veilleux \[8\]](#). The former was merely used to compare the aerodynamic capabilities of both numerical models as the high uncertainty in and sensitivity of the structural model resulted in a difficult reproduction of the aeroelastic behaviour in the experiment. The latter experiment provided data of the final pitch- and heave amplitudes and frequencies of a high-amplitude oscillating motion. No motion- or aerodynamic data over time were publicly available.

The observations, conclusions, advantages and disadvantages are summarised per model below:

- **Engineering Model:**

- Uses a simplified representation of the physics involved in high-amplitude oscillations.
- Is capable of accurately reproducing aerodynamic lift- and moment coefficients compared to experimental data.
- Does not fully capture the effect of the detachment of the LEV and reattachment of the flow on the force coefficient, but describes it with a general trend.
- Is capable of reproducing LCOs.
- Shows the same critical onset velocity of the LCOs as seen in the experiment of [Veilleux \[8\]](#).
- Provides a fast and efficient way of performing aeroelastic simulations. The simulation time is of the order of a couple of seconds.
- Overpredicts the amplitude in pitch and heave compared to experimental data from [Veilleux \[8\]](#).
- Has proven to be very sensitive to the structural damping coefficient which has a big effect on the aeroelastic response in both experiments. Especially, in the stall flutter experiment, the onset of LCOs was affected by the structural damping coefficient. In the classical flutter experiment, the value of the structural damping coefficient merely had an effect on the amplitude of the LCOs.

- **RANS Model:**

- Does capture the full dynamics and obtains the flow fields of several physical quantities of interest.
- Is capable of accurately reproducing aerodynamic lift- and moment coefficients compared to experimental data.
- Does capture the creation and detachment of the LEV.
- Is capable of reproducing LCOs.
- Produces very similar pitch- and heave amplitudes of the LCOs as seen in the experimental data in [Veilleux \[8\]](#).
- Shows a slightly different critical onset velocity of the LCOs as seen in the experiment of [Veilleux \[8\]](#).

-
- Takes substantially more time to perform aeroelastic simulations.
 - Is less sensitive to the structural damping coefficient.

The most suitable model for the parametric study on the flutter behaviour of a wind turbine airfoil in the next chapter is chosen based on these observations. As the parametric study requires analyses of the effect of varying a broad range of parameters on the aeroelastic behaviour of the wind turbine airfoil, it is desired to use a fast and simple, yet stable and accurate numerical model. For this reason, the engineering model is chosen in the remainder of the study.

Chapter 6

Parametric Study

In the previous chapter, the aeroelastic capabilities of the two numerical models have been studied and compared. The most suitable model for the parametric study, which is the engineering model, has been selected and will be used in this chapter to perform a parametric study on the aeroelastic response of a wind turbine airfoil. This comes down to carrying out the final task in the project defined by **Task 5**: *Perform a parametric study on a wind turbine airfoil with the aim of identifying the critical parameters which affect the self-exciting high-amplitude limit cycle oscillations onset and response.* By performing this study and analysing its outcome, the second research question can be answered: **2**. *Which key parameters of a wind turbine airfoil affect the critical onset velocity leading to limit cycle oscillations?*

This chapter starts out with a description of the wind turbine airfoil to be studied in Section 6.1. Section 6.2 presents and discusses the aeroelastic study on the current design of the wind turbine airfoil. In Section 6.3, aeroelastic simulations are carried out on four potential, conceptual designs of the wind turbine airfoil. From the corresponding results, preliminary conclusions are made on identifying the key parameters in the onset of aeroelastic behaviour. These conclusions are used as an input for the methodological and in-depth parametric study performed in Section 6.4. The effect of introducing a structural angle of attack, in order to simulate a wind turbine airfoil operating close to or in stall, on the aeroelastic behaviour is studied in Section 6.5. The particular section also includes a parametric study in order to identify the key parameters that affect aeroelastic behaviour at higher structural angles of attack. Finally, in Section 6.6, an overview of all the observations made and conclusions drawn in this chapter is given and is used to provide an answer to the last research question: **3**. *How can the risk of self-exciting high-amplitude limit cycle oscillations of a wind turbine airfoil be reduced?*

6.1 The Wind Turbine Airfoil

This section provides an overview of the structural parameters of the wind turbine airfoil and the semi-empirical coefficient needed as an input in the engineering model. The parametric study is performed on a wind turbine airfoil which is located at 75 % radius on the XANT-21 wind turbine. At cut-out conditions, $U_\infty = 20$ [m/s], and assuming an axial induction factor of, $a = 0.1$ [-], the airfoil in question would experience a maximum operating incoming velocity of $U_{rel,op} = 45.4$ [m/s], equivalent to $Re = 1.38 \times 10^6$ [-]. The airfoil is very similar to the NREL S819 from Somers [74] and both airfoil are depicted in Figure 6.1.

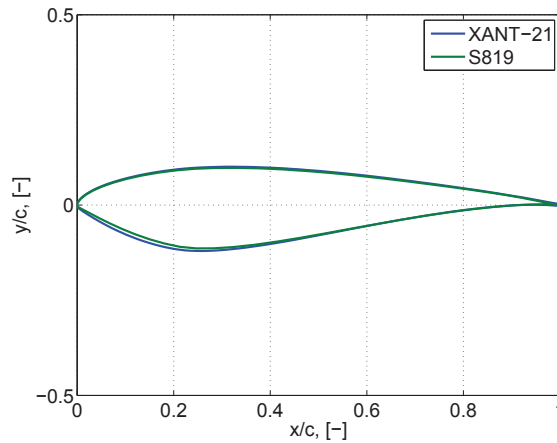


Figure 6.1: Airfoil Contours

The static force coefficient of this particular airfoil have been obtained prior to the thesis and can be found in Lof [70]. The semi-empirical parameters are obtained similarly to the methods described in Section 3.3 and are shown in Table 6.1. The value of T_f is taken from Aagaard Madsen and Rasmussen [75] which uses the value for the FFA-W3-211 which is a similar wind turbine airfoil.

Table 6.1: Semi-Empirical Parameters of the XANT-21 Airfoil.

Parameter	Unit	Value
b_1	[-]	0.33
b_2	[-]	0.05
A_1	[-]	0.40
A_2	[-]	0.23
T_p	[-]	1.5
T_f	[-]	7.0
ω_4	[-]	0.075
$C'_{L0,v}$	[-]	1.3

The structural parameters of the current airfoil design are summarised in Table 6.2. The damping coefficients have been obtained by means of the logarithmic decrement method on wind-off tests. For simplicity a constant damping is assumed.

Table 6.2: Structural Parameters of the XANT-21 Airfoil.

Parameter	Symbol	Unit	Value
Chord	c	[m]	0.446
Total Torsional Spring Stiffness	k_θ	[Nm/rad]	1635
Total Compression Spring Stiffness	k_y	[N/m]	2452
Centre of Rotation	x_{RC}	[%]	26.4
Centre of Gravity	x_{CG}	[%]	44.0
Mass	m	[kg]	10.45
Moment of Inertia around the C.R.	I_{RC}	[kg · m ²]	0.5
Heaving Damping Coefficient	C_y	[N · s/m]	0.94
Torsional Damping Coefficient	C_t	[N · s/rad]	0.17
Natural Frequency in Pitch	f_θ	[Hz]	9.1
Natural Frequency in Heave	f_h	[Hz]	2.4

Now all necessary input is known, the aeroelastic study with the engineering model can be performed. This is done in the following sections.

6.2 Baseline Results

With the known structural parameters as described in the previous section, the pitching- and plunging motion response as a result of varying the relative velocity, U_{rel} , are observed. The airfoil, initially at a equilibrium position at zero angle of attack, is given an initial pitching velocity. The effect of varying the magnitude of the initial pitching velocity is investigated as well. The results are shown in Figure 6.2.

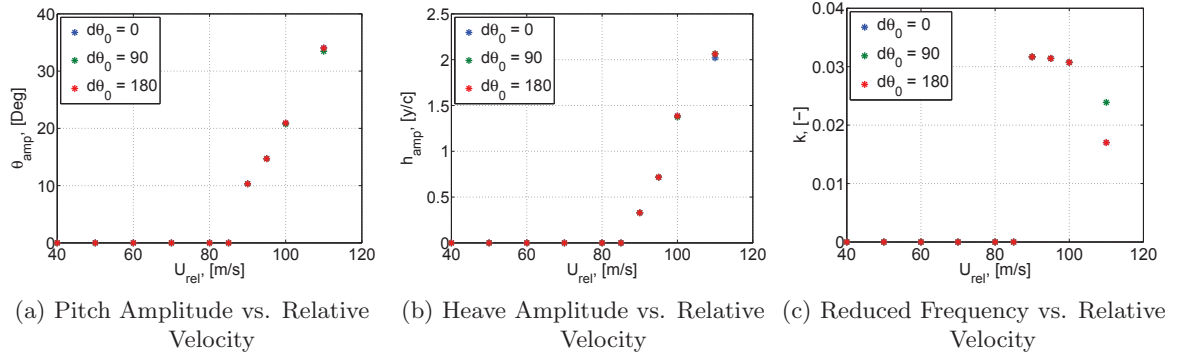


Figure 6.2: Pitch- and Heave Amplitudes and Reduced Frequency of LCOs of the XANT Airfoil obtained with the Engineering Model at Three Different Initial Conditions.

The results show that at the maximum operating incoming velocity, $U_{rel,op} = 45.4$ [m/s], no LCOs occur. Self-excitation is initiated at the critical onset velocity $U_{cr} = 87.5$ [m/s], which is $\frac{87.5}{45.4} \approx 2$ times higher than the maximum operating incoming velocity, which might be considered a very plausible observation for wind turbines as stated in Bichiou et al. [13]. This shows that in the baseline-design, the wind turbine airfoil is not prone

to self-excitation under normal operating conditions at zero structural angle of attack. The graphs further show that changing the initial pitching velocity does not influence the critical onset velocity nor the amplitude of the self-excited LCOs.

In order to be able to find the cause of the onset of LCOs at these particular wind speeds, the frequency of the motion in pitch- and heave direction are studied more closely. Figure 6.3 shows these frequencies for a range of relative wind speeds. What is clearly seen in the figure is that at low wind speeds, the pitch- and heave frequency are apart from each other. When the relative wind speed is increased, the frequencies tend to converge. At $U_{rel} = 80$ [m/s], a sudden jump in the heave frequency occurs which results in a heave frequency very close to the pitch frequency. However, no LCOs are observed yet. The frequencies coalesce exactly at $U_{rel} = 87.5$ [m/s] and from this relative wind speed on, the frequencies remain merged and LCOs occur. Due to the coalescence of the frequencies of the two modes and the fact that the instability occurs at a zero structural angle of attack, thus in a linear lift coefficient region, the aeroelastic instability is classified as *classical flutter*.

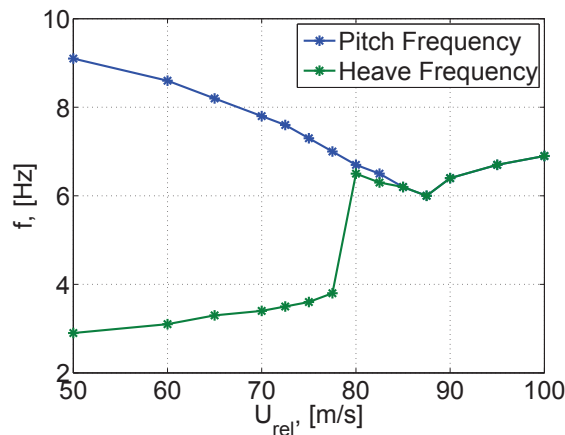


Figure 6.3: Pitch- and Heave Frequency of the Decaying and Oscillating Cases versus Relative Wind Speed of the Baseline Airfoil.

Now the aeroelastic simulations on the so called 'baseline' airfoil have been performed and the type of instability has been classified, an aeroelastic analysis can be performed on four conceptual designs for the wind turbine airfoil. This is done in the next section.

6.3 Conceptual Designs

This section discusses the alternative structural designs of the XANT-21 airfoil which use different materials or material lay-up in several parts of the structure. At first, an overview is given of the structural designs of four concept airfoils. Afterwards, the effect of implementing the alternative materials or lay-up in the airfoil on the critical onset velocity, U_{cr} , is studied. From this study, the key parameters which influence the critical onset velocity are identified. Due to confidentiality, some details of the designs of the airfoil have been left out.

6.3.1 Structural Design

The XANT-21 airfoil consists of four parts: the skin, shearweb, sparcap and a balsa wood part. An overview of the structural parts of the XANT-21 airfoil is shown in Figure 6.4.

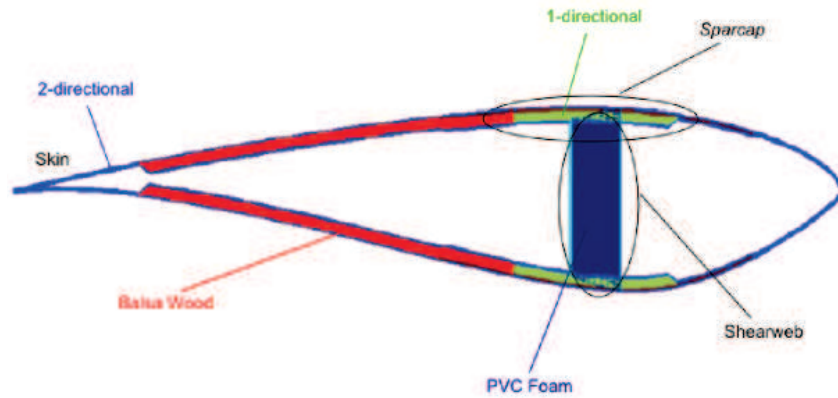


Figure 6.4: Structural Overview of the XANT-21 Airfoil.

Four conceptual designs with varying structural material properties and lay-up have been proposed by XANT. An overview of the implemented changes in the design as well as the major effects on the structural parameters are given below:

1. Skin made of +/- 45 deg ply material:

The material of the whole skin is changed to a ply of +/-45 degree ply material. This leads to a great reduction in heaving- and torsional stiffness. The mass of the airfoil section increases.

2. Skin made of 0-90 deg ply material:

The whole skin of the airfoil section is made of 0-90 degree ply material. This reduces the torsional stiffness substantially. The mass of the airfoil section increases.

3. Sparcap made of flexible UD ply material:

The uni-directional (UD) sparcap material is changed to a flexible sparcap material which mainly reduces the heaving stiffness.

4. Balsa Wood made of flexible UD ply material:

The balsa wood part is replaced with a flexible UD ply material. This results in little change in the torsional- and heaving stiffness. However, major increases are seen in the total mass and, mass moment of inertia, damping coefficient and the location of the centre of gravity.

The relative differences of all structural parameters compared with the 'baseline' airfoil are given in Table 6.3.

Table 6.3: Percentual Difference of Structural Parameters of the Conceptual Designs with the Baseline XANT Airfoil.

Parameter	Units	Values				
		Baseline	Design 1	Design 2	Design 3	Design 4
c	[%]	0	0	0	0	0
k_θ	[%]	0	-45.0	-49.6	-3.6	-0.7
k_y	[%]	0	-28.0	-18.0	-52.0	0
x_{RC}	[%]	0	-2.4	+18.8	+1.0	+0.5
x_{CG}	[%]	0	+2.5	+2.5	-2.7	+13.6
m	[%]	0	+20	+20	+7.0	+53.1
I_{RC}	[%]	0	+26.4	+3.6	-5.0	+83.0
C_y	[%]	0	-20.2	-7.4	0	+23.4
C_t	[%]	0	-17.6	-29.4	-5.9	+35.3
$\omega_{n,h}/\omega_{n,\theta}$	[-]	0.268	0.315	0.318	0.178	0.294

6.3.2 Results of the Conceptual Designs

Now all structural parameters of the conceptual designs are given, the aeroelastic analysis with the engineering model can be performed and the effect of the different structural designs on the critical onset velocity can be assessed. The results are shown in Figure 6.5 which also includes the results of the baseline airfoil.

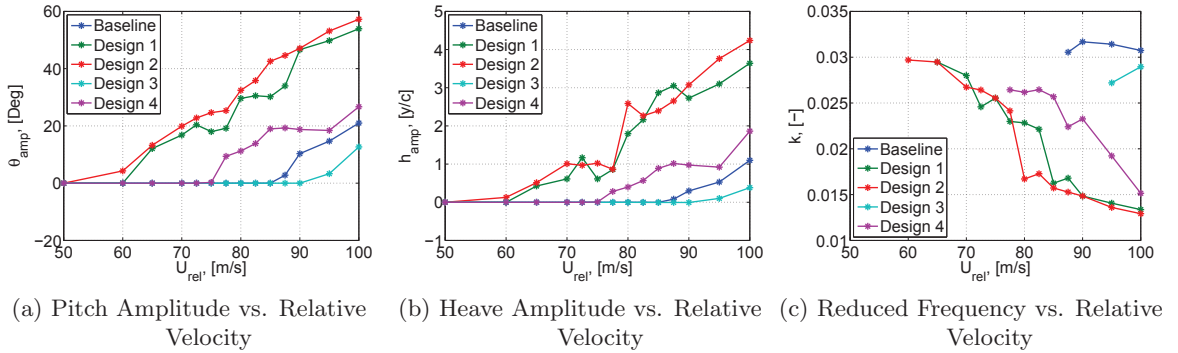


Figure 6.5: Pitch- and Heave Amplitudes and Reduced Frequency of LCOs of Conceptual Designs of the XANT Airfoil.

From the figures, it can be observed that design 1 and 2 reduce the critical onset velocity significantly, design 4 reduces the critical onset velocity moderately, while design 3 increases the critical onset velocity slightly. Noteworthy is that the amplitudes of the pitch and heave motion almost linearly increases with the relative wind speed. An overview of the critical onset velocities are given in Table 6.4.

Table 6.4: Critical Onset Velocities of the Conceptual Designs compared to Baseline Design.

Design	U_{cr} [m/s]	U_{cr} [-]
Baseline	87.5	$2.0 \times U_{rel,op}$
Design 1	65	$1.4 \times U_{rel,op}$
Design 2	60	$1.3 \times U_{rel,op}$
Design 3	95	$2.1 \times U_{rel,op}$
Design 4	77.5	$1.7 \times U_{rel,op}$

6.3.3 Discussion of the Results of the Conceptual Designs

It is clear that the four conceptual designs yield different critical onset velocities. This section discusses briefly what parameters might play a significant role in the change in aeroelastic behaviour type determined to be classical flutter.

As mentioned before, designs 1 and 2 have a substantial negative effect on the critical onset velocity. Both designs have a significant reduction in the torsional- and heaving stiffness. However, the heaving stiffness is significantly reduced in design 3 as well while the critical onset velocity is not so much affected in that case. From this analysis, it can be concluded that the heaving stiffness is of less importance than the pitching stiffness. However, the heaving stiffness plays an important role in the frequency ratio in heave over pitch, which is a critical parameter in classical flutter.

Looking at the results of design 4 and the change in structural parameters in Table 6.3, it can be seen that the stiffness in both degrees of freedom are barely changed. This means that the reduction in U_{cr} lies in the mass and its associated terms: location of the centre of gravity and mass moment of inertia. Classical flutter onset is greatly affected by the location of the centre of gravity as mentioned in Chapter 2. Although the mass moment of inertia has a slight negative impact on the frequency ratio in heave over pitch, it is believed that the reduction of U_{cr} of design 4 is associated with the relatively large rearward shift of the centre of gravity. This theory also fits with the increase of U_{cr} of design 3 as a result of the forward shift of the centre of gravity.

The next section provides some in-depth studies of systematically varying the critical parameters and their effect on the critical onset velocity.

6.4 Parametric Study

This section presents and discusses the effect of varying the critical parameters on the critical onset velocity. Firstly, the effect of varying the damping coefficients is discussed. Secondly, the effect of varying the pitch- and heave stiffness on the critical onset velocity is studied. Afterwards, a parametrisation is done with the goal to find the influence of the mass distribution on the total mass, location of the centre of gravity and the mass moment of inertia and the corresponding effect on the critical onset velocity.

6.4.1 Effect of Pitch- and Heave Damping Coefficient

The effect of varying the pitch- and heave damping coefficient is found not to have any significant effect on the critical onset velocity. This might be contradictory to the fact that in Chapter 5, the engineering model was very sensitive to the value of the damping coefficient. However, this observation is explained by means of Figure 6.6. The figure shows the contributions of the separate terms at $U_{rel} = 87.5$ [m/s] in the equations of motion as formulated in Equation 2.2 and 2.3: the force-, damping- and stiffness contribution. Both figures clearly show that the damping-term contribution indicated by the green lines, compared to the force- and stiffness-term contributions is negligible. For this reason, it has been decided to not perform a parametric study on the pitch- and heave damping coefficient.

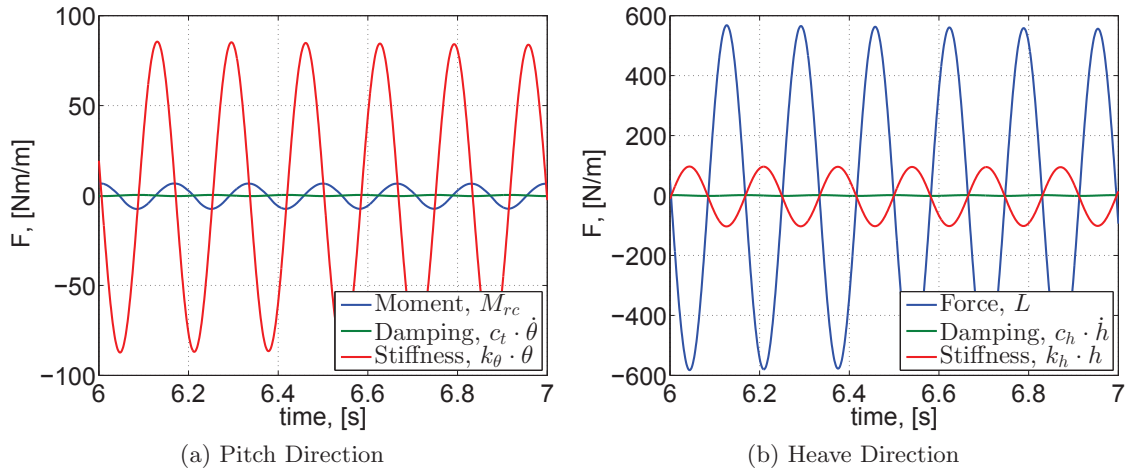


Figure 6.6: Contributions of different Terms in the Equations of Motion in Pitch- and Heave Direction at $U_{rel} = 87.5$ [m/s].

6.4.2 Varying the Pitch- and Heave Stiffness

The effect of reducing the pitch- and heave stiffness on the critical onset velocity is shown in Figure 6.7a as well as the resulting natural frequency ratio is shown in Figure 6.7b. The baseline results obtained in Section 6.2 are represented in the upper-right corner in both figures at $k_y = 100\%$ and $k_\theta = 100\%$. Thus, the x - and y -axes respectively represent the percentage of the baseline heave- and pitch stiffness taken for the aeroelastic analysis. The resulting critical onset velocity is displayed in the colorbar.

From Figure 6.7a it can be easily seen that reducing the pitch stiffness, k_θ , has a significant negative effect on the critical onset velocity. If a pitch stiffness of 50% of the original value is taken, the critical onset velocity reduces with around $\Delta U_{cr} = \frac{60-90}{90} \approx 33\%$.

A reduction in the heave stiffness, k_y , yields an increase in the critical onset velocity. At first thought, this might come across as counter-intuitive: decreasing the stiffness, increases the flutter speed. However, this can be explained by looking at Figure 6.7b. From the figure, it becomes clear that when the heave stiffness, k_y , is reduced, the heave natural frequency, ω_h , decreases which means that the natural frequency ratio of heave

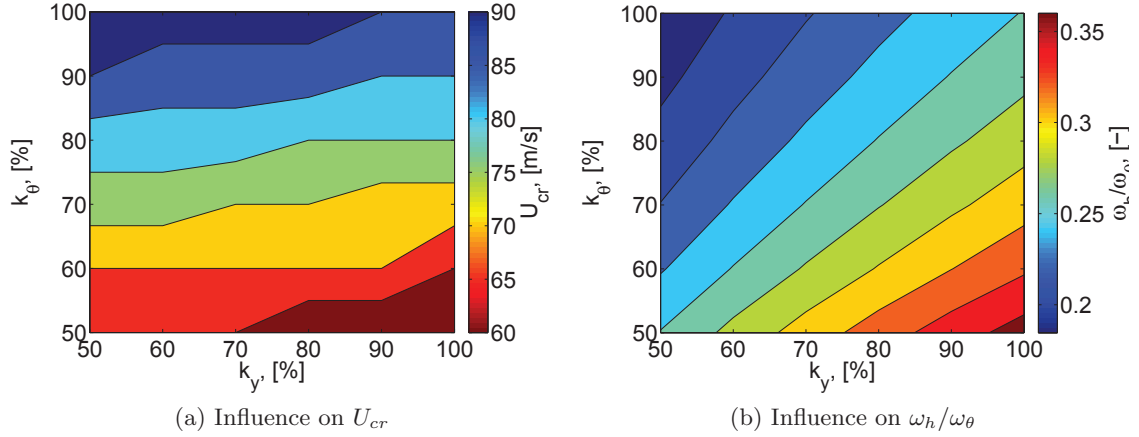


Figure 6.7: The Effect of varying the Pitch- and Heave Stiffness on the critical onset Velocity and Frequency Ratio.

over pitch, ω_h/ω_θ becomes smaller. As this ratio is smaller than 1 for the baseline airfoil, $\omega_h/\omega_\theta < 1$, the ratio would even more deviate from the critical ratio of $\omega_h/\omega_\theta = 1$. Hence, the increase of the critical flutter speed.

Also noteworthy is the fact that the decrease in heave stiffness does not affect the critical onset velocity as much as the pitch stiffness: taking 50% of the original value of k_y increases U_{cr} with $\Delta U_{cr} = \frac{65-60}{60} \approx 8\%$.

6.4.3 Parametrisation of the Mass Distribution

This part deals with the parametrisation of the mass and the associated parameters which are the location of the centre of gravity and the mass moment of inertia. It is decided to divide the total mass of the airfoil depicted in Figure 6.4 into three mass contributions: the sparcap-, skin- and balsa wood mass contributions:

$$m_{total} = m_{spar} + m_{skin} + m_{balsa} \quad (6.1)$$

where m_{spar} includes the mass of the shear webs. With this obtained mass distribution, a relation with the location of the centre of gravity, x_{cg} , and the mass moment of inertia, I_{rc} , can be obtained:

$$x_{cg} = \frac{m_{spar} \cdot x_{sc} + m_{skin} \cdot x_{cg,skin} + m_{balsa} \cdot x_{cg,balsa}}{m_{total}} \quad (6.2)$$

$$I_{rc} = m_{spar} \cdot (x_{sc} - x_{rc})^2 + m_{skin} \cdot (0.75 \cdot c - x_{rc})^2 + m_{balsa} \cdot (x_{cg,balsa} - x_{rc})^2 \quad (6.3)$$

where x_{sc} , $x_{cg,skin}$ and $x_{cg,balsa}$ are respectively the distance from the leading edge to the spar caps, the centre of gravity of the skin and the centre of gravity of the balsa wood part.

It is decided to perform an initial study where the masses of the different parts are changed independently in order to gain some insight on their corresponding effects on the critical onset velocity. All mass-contributions are independently multiplied with a factor 2 and the pitch- and heave stiffness are varied in a similar fashion as in the 'baseline'-airfoil study as shown in Figure 6.7. An overview of the changes in mass and their effect on the location of centre of gravity, mass moment of inertia and total mass is given in Table 6.5.

Table 6.5: *Effect of the Mass Contributions Changes on other Structural Parameters.*

Mass-part Change	m_{total} [%]	x_{cg} [%]	I_{rc} [%]
$m_{\text{spar}} \times 2$	+34.4	-8	+0.9
$m_{\text{skin}} \times 2$	+32.8	-1	+57
$m_{\text{balsa}} \times 2$	+32.8	+9	+41

The resulting critical onset velocities for the different variations in mass contributions, compared with the baseline result obtained previously, are shown in Figure 6.8. Looking at the effect of the mass of the spar caps in Figure 6.8b, a significant increase in the critical onset velocity is observed. Reducing the pitch stiffness with 50 % results in a minimum critical onset velocity of $U_{cr} = 70$ compared to $U_{cr} = 60$ in the baseline case. From Table 6.5, it can be seen that the change in the spar mass barely has an effect on the mass moment of inertia, but merely effects the location of the centre of gravity. Thus, it can be confirmed that a shift of the location of the centre of gravity towards the leading edge positively effects the critical onset velocity.

Comparing the results of changing the mass of the skin with the baseline results, it can be seen that no significant changes in critical onset velocity are apparent, albeit a small negative effect. Noting the fact that the mass moment of inertia in this case changes significantly yields the conclusion that the mass moment of inertia is of less importance compared with the location of the centre of gravity in its effect on the critical onset velocity.

Looking at the effect of changing the mass of the balsa wood part, it can be seen that the critical onset velocity is largely affected in a negative way. This decrease is, based on the conclusions stated before, largely due to the rearward shift of the location of the centre of gravity.

6.4.4 Parametric Study of the Mass Distribution on Flutter Stability

Now a clear correlation between the mass distribution, pitch- and heave stiffness and the critical onset velocity have been observed, a more in-depth study on the critical onset velocity for varying parameters can be performed. The goal of this analysis is to obtain a range of design recommendations in case a reduction of the flexibility of the airfoil is required. The set-up, assumptions and criteria used in this analysis are listed below:

- The pitch stiffness is reduced: $k_{\theta} = [50 \ 75 \ 100]$ % of original k_{θ} .
- The spar cap mass is varied: $m_{\text{spar}} = [80:10:150]$ % of original m_{spar} .

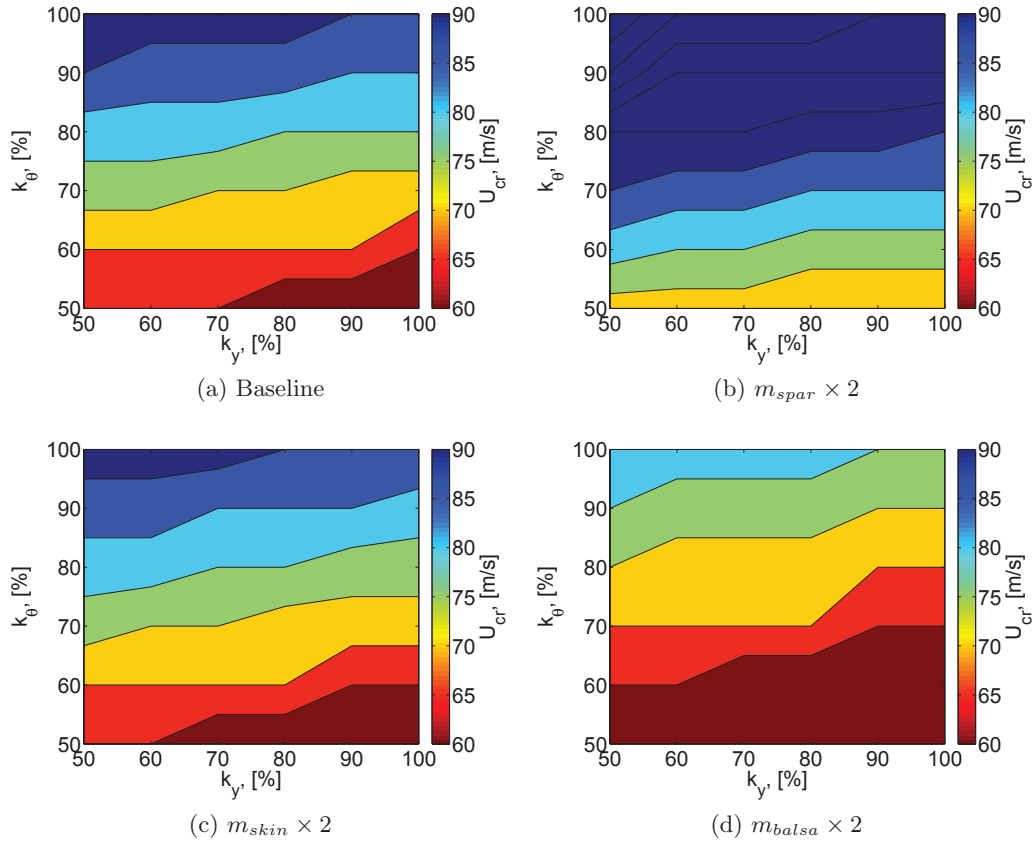


Figure 6.8: Critical Onset Velocities for different Mass-Contributions.

- The skin mass is varied: $m_{skin} = [50:10:150]$ % of original m_{skin} .
- The balsa wood mass is varied: $m_{balsa} = [50:10:200]$ % of original m_{balsa} .
- Criteria set that $U_{cr} \geq 90$ [m/s] must be ensured.
- Assumption is made that the heave stiffness, k_y , is reduced with 25 % (taken as an average of the four conceptual designs).
- Assumption is made that the location of the centre of rotation is fixed.

The parametric study on the flutter stability is performed with the engineering model and the results for the different pitch stiffnesses are discussed below.

$k_\theta = 100\%$:

With the same pitch stiffness as the baseline airfoil, the flutter diagram for a variety of sparcap masses is shown in Figure 6.9. The red area in the graphs denotes a critical onset velocity lower than $U_{cr} = 90$ [m/s] and the blue area denotes the opposite. From the figures can be seen that, as observed before, that increasing the sparcap mass more or less increases the stability range linearly. Increasing the mass of the skin does not have a

large effect on the stability range. The mass of the balsa wood part plays a decisive role in the stability of the airfoil.

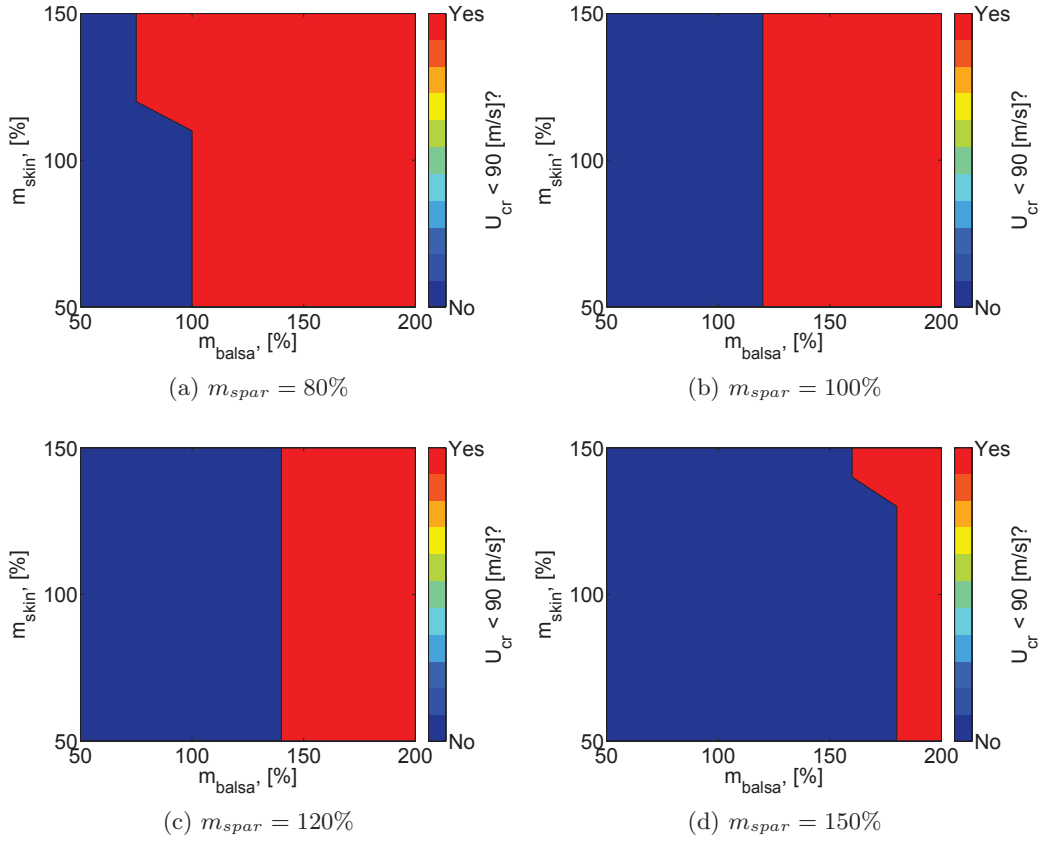


Figure 6.9: Flutter Diagram for different Mass-Combinations at $k_\theta = 100\%$.

$k_\theta = 75\%$:

At a pitch stiffness of 75% of the original value, the stable area of $U_{cr} > 90$ [m/s], indicated by the blue area, becomes significantly smaller and is only reached if the mass of the balsa part is reduced to at least 60% of its baseline value.

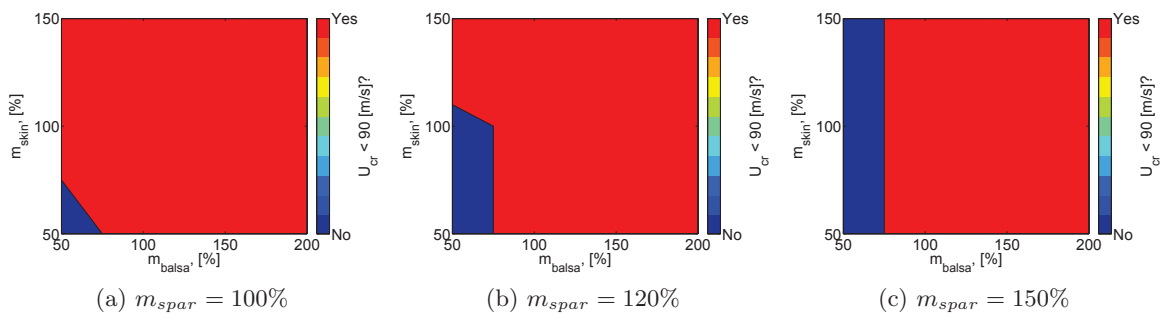


Figure 6.10: Flutter Diagram for different Mass-Combinations at $k_\theta = 75\%$.

$k_\theta = 50\%$:

If the pitch stiffness is reduced to 50% of its original value, the criteria that $U_{cr} > 90$ [m/s] is not fulfilled at all. This means that reducing the torsional stiffness with 50%, no combination of a modification of the mass-contributions ensures a critical onset velocity higher than 90 [m/s]. In order to increase the stability of the airfoil, mass could be added close to the leading edge in order to bring the location of the centre of gravity more forward.

6.5 Structural Angles of Attack Study

As at high wind speeds, stall-controlled wind turbines operate close to stall angles of attack, the aeroelastic behaviour might be significantly different. This section deals with studying the effect of introducing structural angles of attack on the critical onset velocity and the behaviour of the motion in case of flutter instability. The baseline airfoil is taken as a reference case, only the structural angle of attack is varied and the aeroelastic response is obtained with the engineering model. Afterwards, several structural parameters are changed in the design to obtain the critical parameters which affect the critical onset velocity in the aeroelastic responses at higher structural angles of attack.

6.5.1 Results

In this part, the structural angle of attack is varied. The range includes angles of attack in the linear- (far away and close to stall), pre-stall- and post-stall region of the lift-coefficient curve. The resulting responses for the different structural angles of attack are shown in Figure 6.11. The pitch angles are centred around zero by removing the value of the static angle of attack.

The figures clearly show a correlation between the structural angle of attack and the critical onset velocity: the flutter speed decreases with an increasing structural angle of attack. Looking at $\theta_{geom} = 5^\circ$, which is in the linear lift-coefficient region, no difference is observed in the onset velocity, however the amplitude of LCOs are higher than in the baseline case. The first change in flutter speed is observed at $\theta_{geom} = 10^\circ$, which is still in the linear region close to the pre-stall area. Increasing the structural angle of attack to $\theta_{geom} = 12.5^\circ$ and $\theta_{geom} = 15^\circ$ even decreases the critical onset velocity further. The latter one lies beyond the maximum static stall angle of $\alpha_{cl,max} \approx 14^\circ$ and therefore has a negative lift coefficient slope.

Looking at the heave amplitude of $\theta_{geom} = 15^\circ$ in Figure 6.11b, it can be seen that the model predicts a relatively large amplitude heaving motion, even when the pitch motion is barely excited. The motions and the corresponding force coefficients are shown in Figure 6.12. The figures show indeed a very low excitation in pitch (which is not categorised as a LCO) and a high heaving amplitude motion. Looking at the force coefficients it can be seen that the lift coefficient takes high values while the moment coefficient shows very low values. Figure 6.12d shows the separate contributions to the lift coefficient as formulated

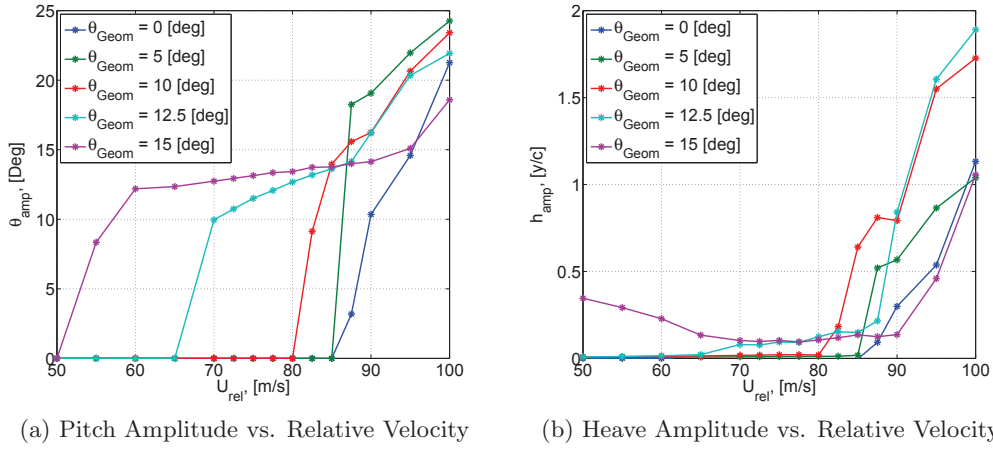


Figure 6.11: Pitch- and Heave Amplitudes and Reduced Frequency of LCOs for different Structural Angles of Attack of the Baseline Airfoil.

in Equation 3.9. The figure shows that the main contributor to the lift coefficient is the lift coefficient due to the dynamic separation point, $C_{L,TE}$, which on its turn shows a high alternating values due to the oscillating motion of the separation point on the airfoil as shown in Figure 6.12e. The engineering model thus predicts a separation point of the flow which moves over the suction surface of the airfoil which leads to the oscillation of the heave motion.

Ignoring the high heave amplitudes at low velocities at $\theta_{geom} = 15^\circ$, it can be observed in Figure 6.11b that when the airfoil is excited, the growth and value of the heave amplitude in the stall-region structural angles of attack cases is significantly lower than in the linear region structural angles of attack. This might be an indication of stall flutter as this shows that the heave motion plays a less important role in the flutter instability. In order to confirm this hypothesis, a deeper analysis of what is actually happening is performed.

Comparing the development of the pitch amplitude over the relative wind speed at an increasing structural angle of attack from Figure 6.11 with the stall flutter study results

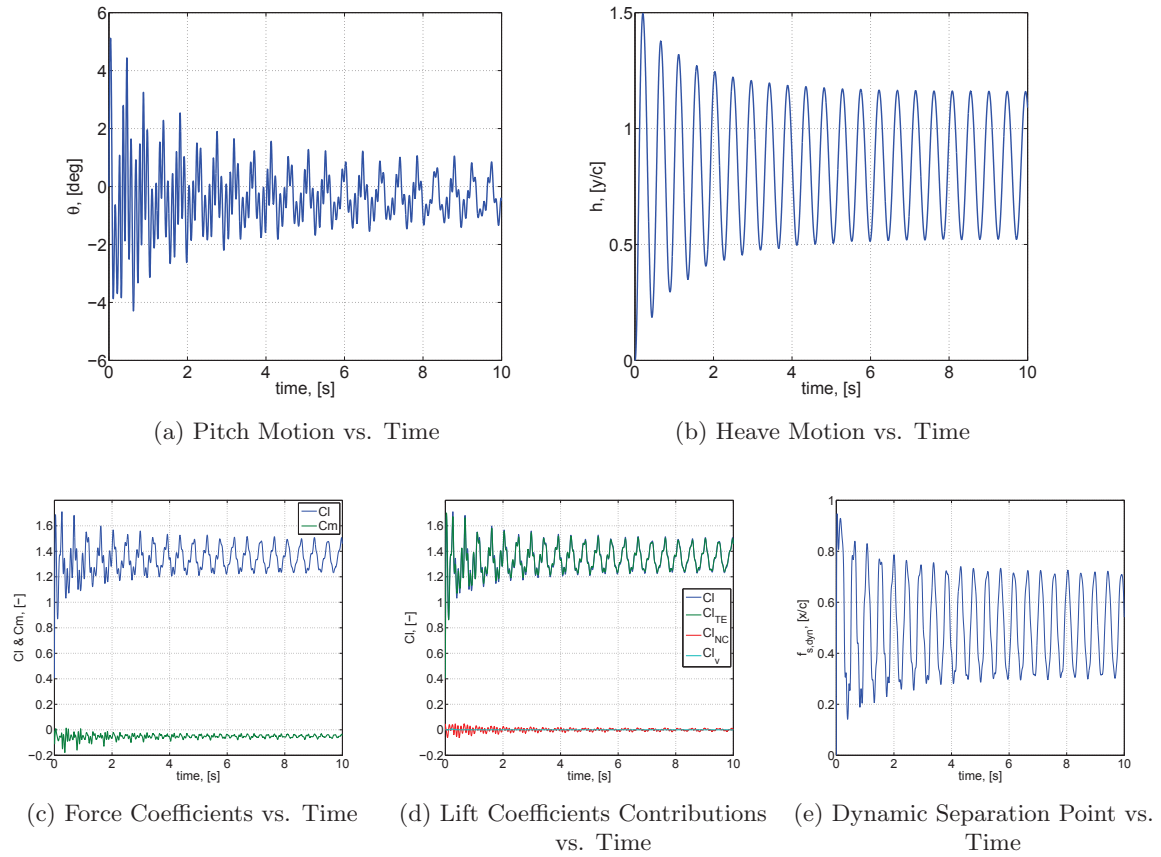


Figure 6.12: Pitch- and Heave Motion, Force Coefficients and Dynamic Separation Point at $\theta_{geom} = 15^\circ$ and $U_{rel} = 50$ [m/s].

from Figure 2.5 from Razak et al. [11], similar observations are made. The growth of pitch amplitude of the airfoil is in the case of a higher structural angle of attack lower than at a lower structural angle of attack. Razak et al. [11] classified the lower growth as a typical indication of stall flutter as they noticed that classical flutter behaves in a more destructive way. The pitch amplitude development at $\theta_{geom} = 12.5^\circ$ and $\theta_{geom} = 15^\circ$ show a lower growth rate and therefore are an indication of stall flutter.

Studying the motions at the critical onset velocity of $\theta_{geom} = 5^\circ$ and $\theta_{geom} = 15^\circ$ provides some interesting information about the onset of the flutter instability process. The pitching- and heaving motions of both structural angles of attack are shown respectively in Figure 6.13 and Figure 6.14.

The frequencies of oscillation are displayed in the captions of the figures. When these are compared it can be seen that the flutter instability at $\theta_{geom} = 5^\circ$ arises from the fact that the frequencies of both motions coalesce and thus still is associated with the classical flutter type. Looking at the motions and frequencies of the results of $\theta_{geom} = 15^\circ$, it is seen that both modes oscillate close to their own natural frequencies as shown in Table 6.2 which means that the frequencies do not coalesce. From this observation, it can be

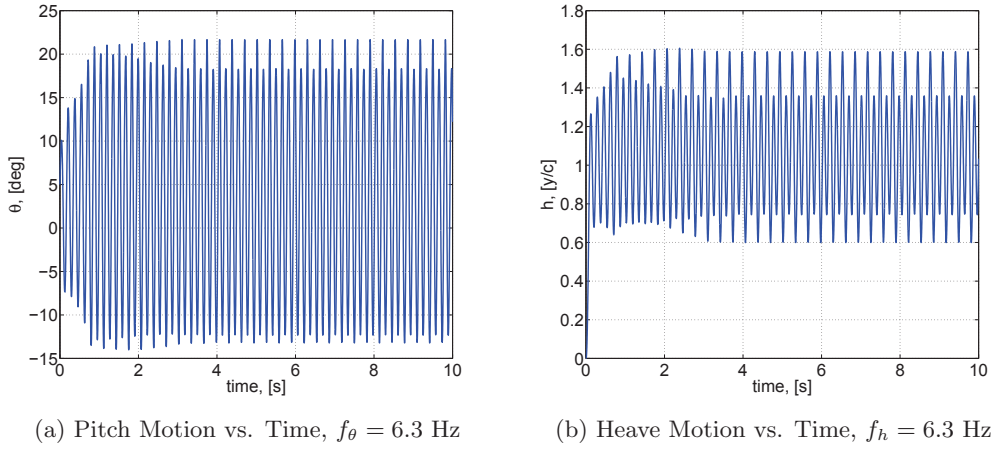


Figure 6.13: Pitch- and Heave Motion at the $U_{cr} = 87.5$ m/s of $\theta_{geom} = 5^\circ$

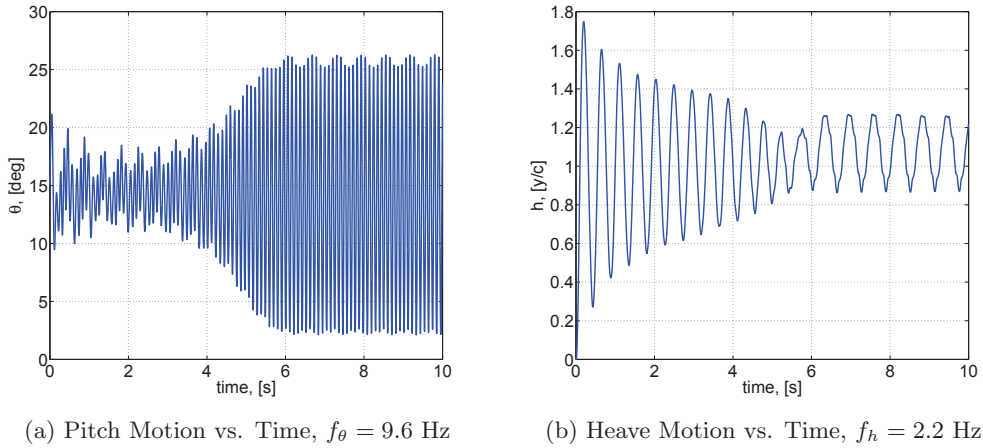


Figure 6.14: Pitch- and Heave Motion at the $U_{cr} = 55$ m/s of $\theta_{geom} = 15^\circ$

concluded that the type of flutter instability at the critical onset velocity at $\theta_{geom} = 15^\circ$ is not associated with classical flutter where the energy transfer from the fluid to the structure relies on the coalescence of the frequencies.

Looking more closely at the pitch- and heave frequencies at the different structural angles of attack for the whole range of relative wind speeds, shown in Figure 6.15, the different types of flutter instabilities can be seen. The grey area in the figures denote that LCOs occur. At $\theta_{geom} = 0^\circ$ and $\theta_{geom} = 5^\circ$, at the critical onset velocities, a clear coalescence of the frequencies of both modes are obtained. At $\theta_{geom} = 10^\circ$, at the LCO onset, the frequencies initially merge. Afterwards, however the frequency of the heave motion differs from the pitching frequency before they merge again around the critical classical flutter speed. At $\theta_{geom} = 15^\circ$, at low wind speeds no coalescence of the frequencies is observed while the airfoil undergoes LCOs. This is an indication of stall flutter. Interesting to note is that at the critical onset velocity of the baseline case, $U_{cr} = 87.5$ [m/s], the frequency

in heave is equal to the frequency in pitch. This shows that at structural angles of attack close to stall, above the classical flutter onset velocity coalescence of the two frequencies occurs.

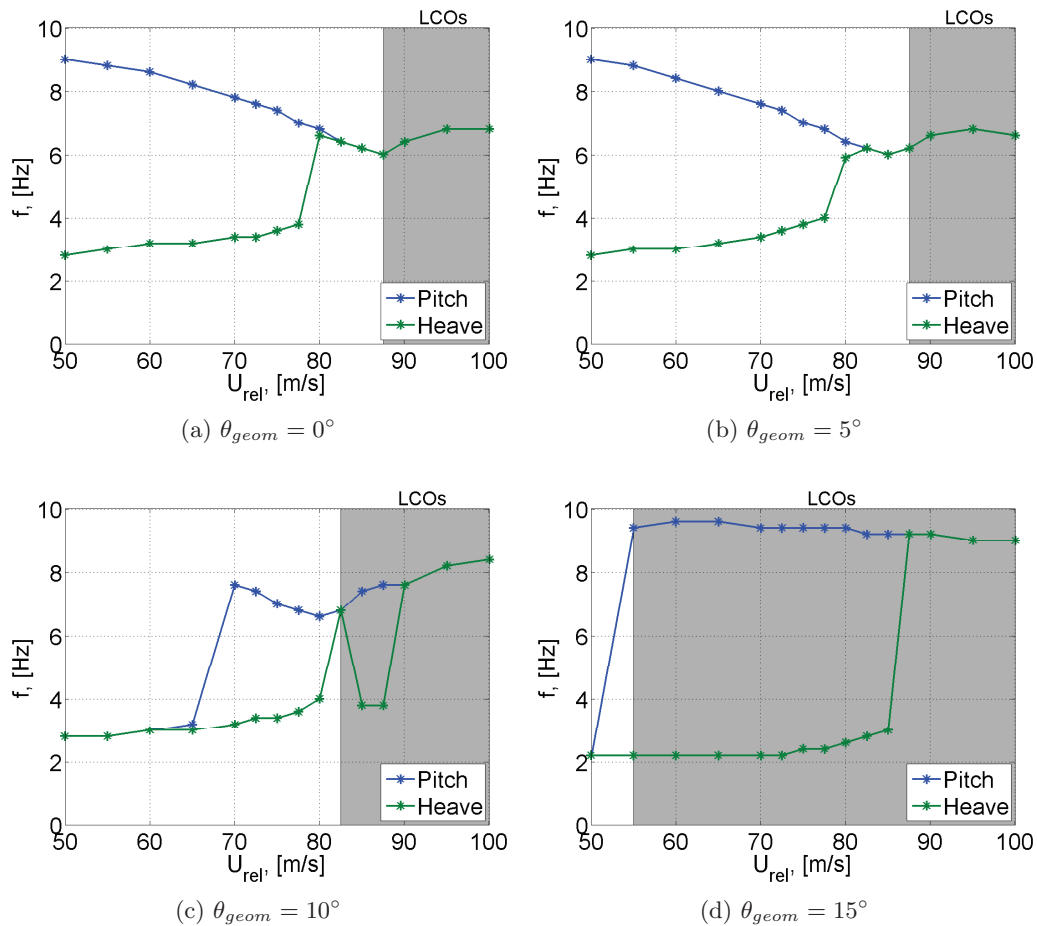


Figure 6.15: Pitch- and Heave Frequencies versus Wind Speeds at different θ_{geom}

Now, the flutter type at structural angles of attack close to stall has been determined to be stall flutter, it is of importance to investigate whether the same structural parameters as in the classical flutter instability have a similar effect on the onset of the stall flutter instability. The following two sections deal with the identification of these parameters by means of sensitivity analyses on the critical onset velocities at higher structural angles of attack.

6.5.2 Sensitivity Analysis of the Pitch- and Heave Stiffness

In this part, a sensitivity analysis is carried out on the pitch- and heave stiffness at different structural angles of attack in order to check whether these parameters have similar effects on the critical onset velocity as in the classical flutter cases. The results are displayed in Figure 6.16.

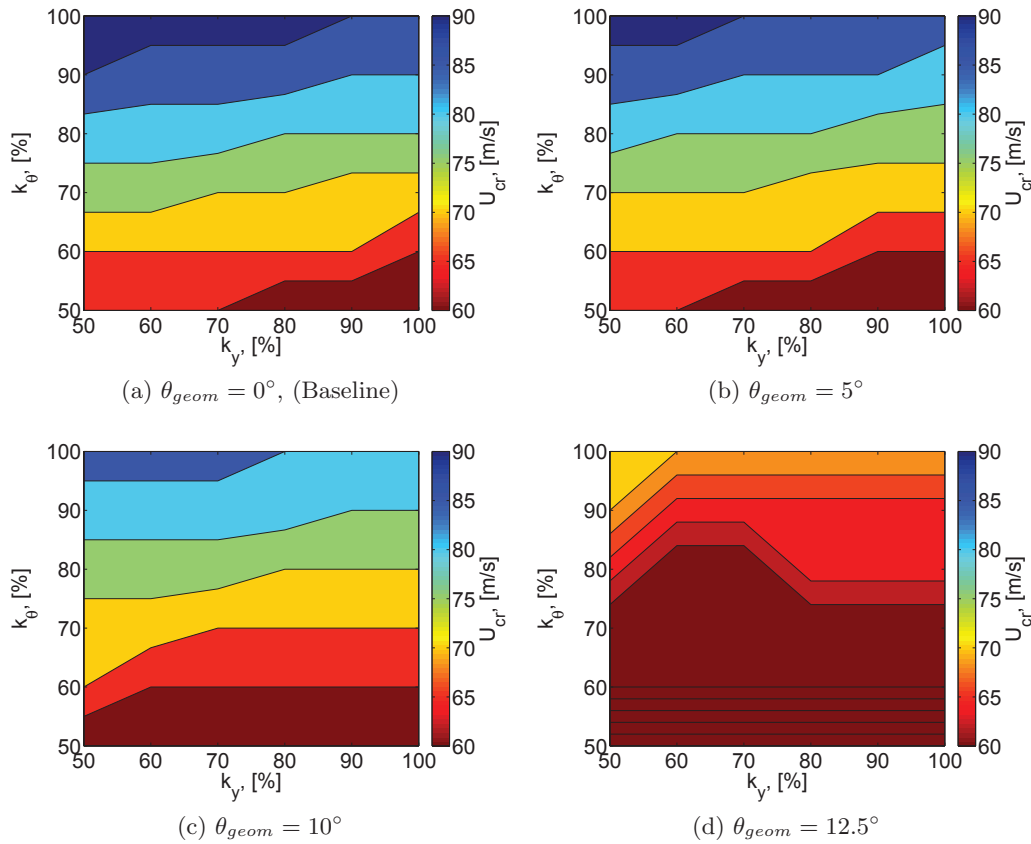


Figure 6.16: Critical Onset Velocity for different Pitch- and Heave Stiffness at different Structural Angles of Attack.

Looking at the results from $\theta_{geom} = 5^\circ$ in Figure 6.16b, no significant changes are observed in the critical onset velocity compared to the baseline results. As the initial conditions of the airfoil still lies in the linear region of the lift coefficient curve which is far enough from the static stall angle, the same type of instability is observed as in the baseline case. At $\theta_{geom} = 10^\circ$, which is at the border of the linear region, the critical onset velocity is reached at lower values than in the baseline case and it has been mentioned before, that the lower onset is due to the occurrence of the stall flutter phenomenon. However, the same trend regarding the effect of varying the pitch- and heave stiffness on the critical onset velocity is seen as in the classical flutter baseline case. This shows that in both types of flutter, the pitch- and heave stiffness have the same amount of effect on the critical onset velocity. At $\theta_{geom} = 12.5^\circ$, which is in the non-linear, positive pre-stall region, the critical onset velocity is dramatically reduced. Interesting to note is that for a certain range of lower heave stiffness, the critical onset velocity is decreased, while until now only increases in the critical onset velocity with a decreasing heave stiffness have been observed.

6.5.3 Sensitivity Analysis of the Mass Distribution

In this part, the influence of the mass distribution on the stability of the airfoil at $\theta_{geom} = 12.5^\circ$ is investigated following the same method as described in Section 6.4. The results are shown in Figure 6.17 (note that the legend has a different range of values than used before as lower critical onset velocity are reached at the concerning structural angle of attack).

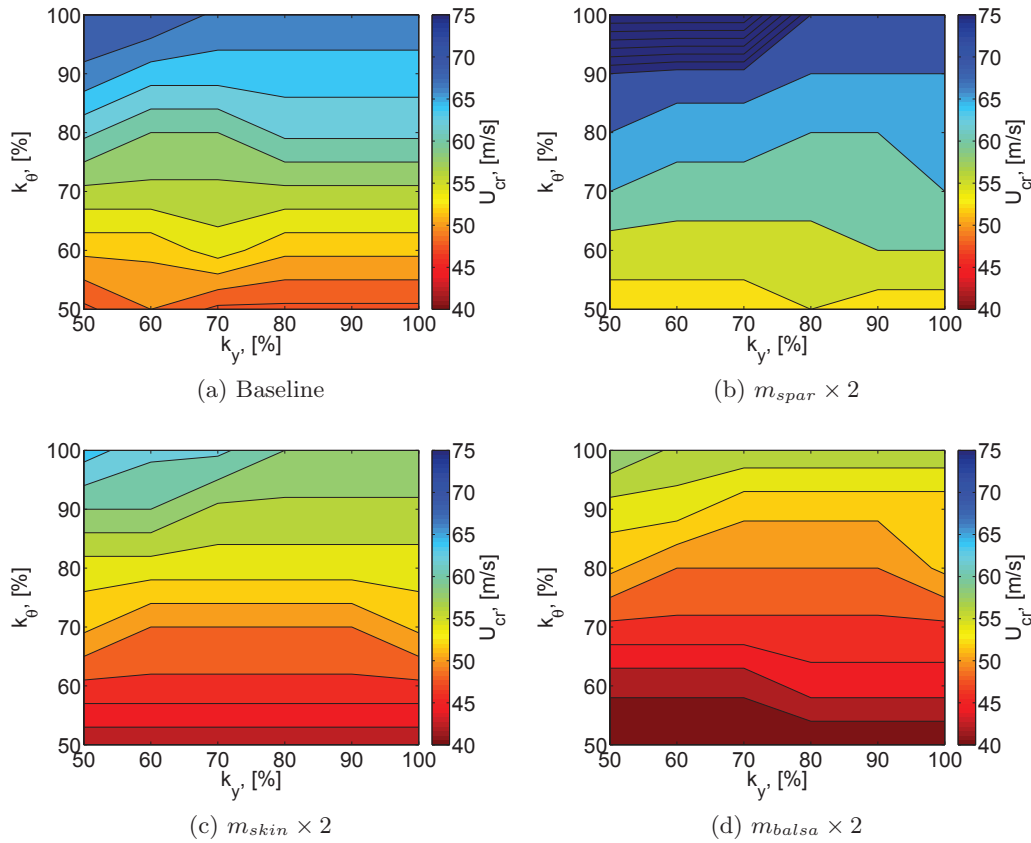


Figure 6.17: Critical Onset Velocity for different Mass Distributions and varying Pitch- and Heave Stiffness at $\theta_{geom} = 12.5^\circ$.

Comparing these results with the mass distribution study performed in Section 6.4, it can be seen that in general similar trends are obtained:

- Increasing the mass of the spar, m_{spar} , increases the critical onset velocity.
- Increasing the mass of the skin, m_{skin} , decreases the critical onset velocity.
- Increasing the mass of the balsa wood part, m_{balsa} , decreases the critical onset velocity substantially.

However, an additional observation is made that decreasing the heave stiffness, k_h , despite the fact that the frequency ratio decreases, sometimes leads to a decrease of the critical

onset velocity. This is contradictory to the observations made before in the classical flutter cases. This might be caused by the fact that at higher structural angles of attack, initially only oscillations may be observed in heave direction and with a decrease in heave stiffness, these oscillations are triggered at lower critical onset velocities.

6.6 Summary

The parametric study on the aeroelastic behaviour of a wind turbine airfoil performed with the engineering model in this chapter has resulted in a completion of the final task: **Task 5:** *Perform a parametric study on a wind turbine airfoil with the aim of identifying the critical parameters which affect the self-exciting high-amplitude limit cycle oscillations onset and response.* Completing this task has provided several answers to the second research question: **2.** *Which key parameters of a wind turbine airfoil affect the critical onset velocity leading to limit cycle oscillations?* This final section provides an overview of the observations made and conclusions drawn in the aeroelastic study on the wind turbine airfoil which have led to these answers. Furthermore, these observations and conclusions will be used in answering the third research question.

The parametric study has been carried out on the aeroelastic response of a wind turbine airfoil. The current airfoil design at 75% radius of the XANT-21 wind turbine blade, was taken as the reference case. The reference case showed not to be exposed to risk on aeroelastic flutter in normal operating conditions. At high wind speeds a factor 2 above the maximum operating wind speed, at zero structural angle of attack, classical flutter has been observed numerically. Afterwards, the aeroelastic simulations with the engineering model have been carried out on four conceptual structural designs of the particular airfoil. From the results it was observed that two alternative designs, where the torsional stiffness was drastically reduced, decreases the critical onset velocity significantly which increases the risk on aeroelastic instabilities. These analyses provided some important insights in the key structural parameters which play a role in the onset of aeroelastic instabilities. A methodological approach to identify the effect of these parameters has been carried out. Furthermore, a parametric study at higher structural angles of attack in the linear lift coefficient region, close to stall and in stall has been performed. These studies have led to the identification of the following key parameters which affect the critical onset velocity and the aeroelastic response:

- Decreasing the torsional stiffness, k_θ , drastically decreases the critical onset velocity.
- A natural frequency ratio, ω_h/ω_θ , close to one increases the risk on aeroelastic instabilities.
- The location of the centre of gravity, x_{cg} , plays an important role in the onset of LCOs: when this parameter moves towards the leading edge increases the critical onset velocity. Its location is directly related to the mass distribution.
- In case of a zero structural angle of attack, decreasing the heaving stiffness, k_h , increased the critical onset velocity. This was merely due to natural frequency ratio

getting closer to one. However in the case of a structural angle of attack close stall, decreasing the heaving stiffness showed also a decrease in the critical onset velocity. It must be said that the effect of changing the heaving stiffness was not as significant as change the torsional stiffness.

- Higher structural angles of attack decreases the critical onset velocity and leads to initiation of the stall flutter phenomenon.

With these critical parameters in mind, finally the third and last research question can be answered: **3.** *How can the risk of self-exciting high-amplitude limit cycle oscillations of a wind turbine airfoil be reduced?*

First of all, considering the conceptual designs of the XANT wind turbine airfoil, it is highly recommended not to replace the material of the skin with the flexible material in any lay-up as this will drastically increase the risk on aeroelastic instabilities. Practically, this comes down to a recommendation to not reduce the total torsional stiffness of the airfoil with more than 25%. Design 1 and Design 2 are classified as high risk in terms of potential aeroelastic instabilities.

Secondly, a conclusion of the parametric study on the wind turbine airfoil was that the distribution of the several mass contributions plays an important role in the critical onset velocity. Increasing the mass of the spar caps, decreasing the mass of the skin or balsa wood moves the location of the centre of gravity forward which has a significant effect on the aeroelastic stability of the airfoil. If this is an impractical procedure or solution, mass can be added close to the leading edge. This will even amplify the effect on the critical onset velocity as the distance between the leading edge and the centre of gravity is larger than the distance to the spar caps.

Thirdly, it is highly recommended to obtain in-depth knowledge about the structural angles of attack at which the airfoil operates. As seen before, the operating structural angle of attack highly affects the critical onset velocity. When these operating ranges are studied, more can be said about the risk on self-excited aeroelastic behaviour.

Conclusions & Recommendations

This report is an outcome of the master thesis for obtaining the MSc Degree at the Delft University of Technology and Denmark Technical University. The research subject was based on the usage of flexible materials in a wind turbine blade and how this might affect the aeroelastic behaviour of the blade by means of a numerical, parametric study. The end of the project has been reached as the tasks and research questions formulated in Chapter 1 have been covered.

This chapter discusses the main conclusions drawn during the course of work and provides recommendations for further research. The conclusions of this thesis are divided according to the research questions and are discussed in Section 7.1. Section 7.2 provides recommendations for improving the modelling procedures and for further research on the topic of aeroelastic instabilities.

7.1 Conclusions

In order to provide a clear and structured method of presenting the answers to the research questions, this section is divided accordingly.

1. Which numerical models are able to predict onset and behaviour of self-exciting high-amplitude limit cycle oscillations of an airfoil?

The development, validation and aeroelastic studies with the engineering- and RANS model have been done in order to find an answer to the first research question. A thorough insight in their capabilities, advantages and disadvantages have been obtained during the course of this project and the most important observations and conclusions are discussed here.

The Engineering Model

In the engineering model, an aerodynamic part is coupled with a structural solver. The aerodynamic part consists of the Risø dynamic stall model from Hansen [4] with an additional LEV contribution to the lift from Larsen et al. [5] and the structural solver consists of the equations of motion of a 2D airfoil in two degrees of freedom. Conclusions on the capabilities of the engineering model is given:

- Introducing the LEV-contribution improves the accuracy of the force prediction of the Risø dynamic stall model at high amplitudes of motion.
- The dynamic stall model is capable of obtaining the maximum peak values and general trend of the force coefficients in the high-amplitudes of a dynamically pitching and plunging airfoil. However, the exact dynamics in the process of the detachment of the LEV and reattachment of the flow afterwards is not fully captured.
- The aeroelastic engineering model is capable of predicting a self-excited instability leading to LCOs.
- The engineering model is capable of predicting the critical onset velocity with satisfactory accuracy.
- The accuracy in predicting the amplitudes of motion in pitch- and heave direction is limited due to model not fully capturing the dynamics in the physics of the creation and shedding of the LEV and sensitivity to the damping coefficient.
- The engineering model has proven to be a fast and efficient method to study the effect of varying several structural parameters on the aeroelastic behaviour of the airfoil.

The RANS Model

The aeroelastic RANS model of a 2D airfoil was created in OpenFOAM by means of a fluid-structure interaction approach. Below, the observations made and conclusions drawn during the analysis of the RANS model are listed:

- The RANS model with the $k-\omega$ SST turbulence model is capable to capture the creation, growth and detachment of a LEV and TEV at high-amplitude oscillations.
- The RANS model is able to produce self-excited high-amplitude LCOs.
- A typical simulation time of 10 seconds of an aeroelastic study on an airfoil at high-amplitudes in pitch- and heave direction with the RANS model is around 120 hours equivalent to 5 days. This long simulation time, compared to the engineering model, has been the most important reason to not use the RANS model in the parametric study.

Based on the findings made during the project, the engineering model has been chosen as the most suitable model to use in answering the second and third research questions.

2. Which key parameters of a wind turbine airfoil affect the critical onset velocity leading to limit cycle oscillations?

The parametric study with the aeroelastic engineering model has led to the following conclusions:

- Decreasing the torsional stiffness, k_θ , drastically decreases the critical onset velocity. This makes the first and second conceptual designs of the wind turbine airfoil, which replace the complete skin with a flexible material, unrealistic as the risk on aerodynamic instabilities greatly increases.
- A natural frequency ratio, ω_h/ω_θ , close to one increases the risk on aeroelastic instabilities.
- The location of the centre of gravity, x_{cg} , plays an important role in the onset of LCOs: when this parameter is shifted towards the leading edge, the critical onset velocity is increased and therefore the risk on aeroelastic instability is decreased.
- Higher structural angles of attack decrease the critical onset velocity and leads to initiation of the stall flutter phenomenon.
- The heave stiffness, k_h , is considered to have less effect than the torsional stiffness on the initiation of the aeroelastic instabilities. At structural angles of attack in the linear lift coefficient region, decreasing this parameter even increases the critical onset velocity of the wind turbine airfoil. At structural angles of attack close to stall, changing the value of this parameters can either have a positive or a negative effect on the critical onset velocity.

These conclusions are used in answering the third research question:

3. How can the risk of self-exciting high-amplitude limit cycle oscillations of a wind turbine airfoil be reduced?

- Considering the conceptual designs of the XANT wind turbine airfoil, it is highly recommended not to replace the material of the skin with the flexible material in any lay-up as this will drastically increase the risk on aeroelastic instabilities. Practically, this comes down to a recommendation to not reduce the total torsional stiffness of the airfoil with more than 25%.
- In order to increase the aeroelastic stability of the airfoil, it is recommended to try to shift the location of the centre of gravity as much towards the leading edge of the airfoil. This is done by adding the mass to the leading edge of the airfoil or another option more specifically for the XANT-airfoil would be to increase the mass of the sparcaps and/or shear web.
- It is highly recommended to obtain in-depth knowledge about the structural angles of attack at which the airfoil operates in real life. As seen before, the operating structural angle of attack highly affects the critical onset velocity. When these operating ranges are studied, more can be said about the risk on self-excited aeroelastic behaviour.

7.2 Recommendations

Given the time constraints, available data and simplifications of real life situations not every aspect of the aeroelastic behaviour of a wind turbine airfoil has been solved. This section discusses the recommendations made for improving the modelling procedure and for further research on the topic of aeroelasticity of flexible wind turbines and is divided accordingly.

Numerically Modelling of Aeroelastic Behaviour of an Airfoil

As the aeroelastic behaviour of the airfoil has been studied numerically, simplifications are inherent to modelling the actual physics of what happens in the real life case. Recommendations on how to improve capturing of the actual physics by a model, based on observations made during this thesis, are listed below:

- In order to provide a more realistic aeroelastic study on a wind turbine airfoil, it is recommended to incorporate the varying loads during a rotation of a wind turbine rotor. This means including the tower shadow, turbulence and gravitational effects into the numerical simulations.
- In order to provide a more representable model for a flexible wind turbine, it is recommended to perform the parametric study with 3D aeroelastic tools, such as HAWC2 [76], FAST [77], Bladed [78] or other software packages. Performing aeroelastic simulations on a 2D airfoil provides a fast and easy method of acquiring insight in the dynamic behaviour and interaction between the fluid and structure. However, this 2D representation introduces some uncertainty compared to the real life case as the interaction with other parts of the blade or tower and other 3D effects are not taken into account.
- In order to improve the capability of the semi-empirical dynamic stall model to capture the lift- and moment coefficients, it is recommended to include a formulation which includes the shedding of the LEV and the attachment of the flow into more detail. However, this will give rise to some great challenges as this formulation would introduce additional airfoil dependent parameters.
- In order to improve the numerical simulations of the aeroelastic behaviour, in-depth knowledge of the non-linear behaviour of the damping coefficient and stiffness is required. State-of-the-art research focusses on the non-linear behaviour of certain structures at high deflections and rotations. The non-linear behaviour often results in an increase in structural damping and stiffness. However, no clear theory has been developed yet about the non-linear behaviour.
- Eventually, it is desired to perform fluid-structure interaction simulations with high-fidelity methods of solving the Navier-Stokes equations, such as DES, on a complete wind turbine with a flexible FEM structural model. In this way, the complete dynamics and interaction of the fluid on the structure and vice-versa can be captured with high-fidelity in order to obtain a detailed insight in the resulting behaviour of

the wind turbine. With the ever increasing computational speed of processors, these simulations have become more and more feasible in the last years. However, the computational power- and time required for such simulations still make it practically uninteresting for most industry applications nowadays.

Further Research in the Field of Aeroelasticity

This part discusses some recommendations in further research in the field of wind turbine aeroelasticity with the focus on a more flexible design.

- As no major aeroelastic instabilities have been observed in wind turbine applications nor many aeroelastic experiments on wind turbines have been performed, it is difficult to validate aeroelastic codes with real life data. Therefore, it is recommended to perform aeroelastic experiments on wind turbine blades or on the complete wind turbine, especially considering the fact that the increasing diameters and flexibility of the blades lead to an increase in risk on aeroelastic instabilities.
- In order to avoid jeopardizing the aeroelastic stability of the wind turbine blade by incorporating flexible materials, other techniques than changing the material or redistributing the mass to ensure aeroelastic stability are available. Some of these techniques are: piezo-electric trailing edge flaps, plasma actuated flow control or boundary layer suction could offer some possibilities in controlling the dynamics of the flow.
- Incorporating new materials in the flexible blade design and using a passively deforming blade might introduce some additional fatigue problems during the lifetime of the wind turbine. In order to avoid these type of problems, in-depth knowledge about the behaviour of the materials on the long term are required.

References

- [1] European Wind Energy Association et al. *The economics of wind energy*. EWEA, 2009.
- [2] MathWorks. *MATLAB Primer*. Inc, 2015.
- [3] OpenCFD. Openfoam - the open source cfd toolbox - user's guide. www.openfoam.org, 28th September 2013.
- [4] M.H. Hansen. Aeroelastic instability problems for wind turbines. *Wind Energy*, 10: 551–577, 2007.
- [5] Jesper Winther Larsen, Søren RK Nielsen, and Steen Krenk. Dynamic stall model for wind turbine airfoils. *Journal of Fluids and Structures*, 23(7):959–982, 2007.
- [6] Walter D Pilkey and Deborah F Pilkey. *Peterson's stress concentration factors*. John Wiley & Sons, 2008.
- [7] Jing Li. *Experimental investigation of the low speed stall flutter of an airfoil*. PhD thesis, Manchester, 2007.
- [8] Jean-Christoph Veilleux. Optimization of a fully-passive flapping-airfoil turbine. Master's thesis, Université Laval, 2014.
- [9] A.R. Collar. The expanding domain of aeroelasticity. *Royal Aeronautical Society Journal*, 50:613–636, 1946.
- [10] J.G. Holierhoek. *Aeroelasticity of Large Wind Turbines*. Ph.D. Thesis, TU Delft, Delft, The Netherlands, 2008.
- [11] N.A. Razak, T. Andrienne, and G. Dimitriadis. Flutter and stall flutter of a rectangular wing in a wind tunnel. *AIAA Journal*, 49:2258–2271, 2011.
- [12] Maziar Arjomandi-Richard Kelso Amanullah Choudhry, Ryan Leknys. An insight into the dynamic stall lift characteristics. Available on ScienceDirect, 2014.

- [13] Youssef Bichiou, Abdessattar Abdelkefi, and Muhammed R Hajj. Nonlinear aeroelastic characterization of wind turbine blades. *Journal of Vibration and Control*, page 1077546314529986, 2014.
- [14] Dominique Poirel and Francisco Mendes. Experimental investigation of small-amplitude self-sustained pitch–heave oscillations of a naca 0012 airfoil at transitional reynolds numbers. In *50th AIAA aerospace sciences meeting. American Institute of Aeronautics and Astronautics, Reston, Virginia*, [http://dx. doi. org/10.2514/6.2012-40](http://dx.doi.org/10.2514/6.2012-40), 2012.
- [15] Jean-Christoph Veilleux. Private communication. March 2015.
- [16] Morten Hartvig Hansen, Mac Gaunaa, and Helge Aagaard Madsen. *A Beddoes-Leishman type dynamic stall model in state-space and indicial formulations*. 2004.
- [17] Ansys. Introduction to ansys, fluent. Presentation, Lecture 6 - Turbulence, 2012.
- [18] URL http://www.cfd-online.com/Wiki/Two_equation_turbulence_models.
- [19] Olivier A Bauchau. Dymore users manual. *Georgia Inst. of Technology, Atlanta*, 2007.
- [20] Eric Lantz, R Wiser, and M Hand. Iea wind task 26: The past and future cost of wind energy, work package 2. Technical report, National Renewable Energy Laboratory (NREL), Golden, CO., 2012.
- [21] R.L. Bisplinghoff, H. Ashley, and R.L. Halfman. *Aeroelasticity*. Addison-Wesley Publishing Company, Inc., 1957. ISBN 0486691896.
- [22] Martin Otto Laver Hansen, Jens Nørkær Sørensen, S Voutsinas, Niels Sørensen, and H Aa Madsen. State of the art in wind turbine aerodynamics and aeroelasticity. *Progress in aerospace sciences*, 42(4):285–330, 2006.
- [23] E.H. Dowell, R. Clark, D. Cox, H.C. Curtiss Jr, J.W. Edwards, K.C. Hall, D.A. Peters, R. Scanlan, E. Simiu, F. Sisto, and T.W. Strganac. *A Modern Course in Aeroelasticity*. Kluwer Academic Publisher, 2005. ISBN 1-4020-2106-2.
- [24] Rajeev Baran. Aeroelastic analysis and classical flutter of a wind turbine using blademode v.2.0 and phatas in focus 6. Master’s thesis, TU Delft, 2013.
- [25] Gregory Politakis, Wouter Haans, and GJW Van Bussel. Suppression of classical flutter using a smart blade. In *2008 American Society of Mechanical Engineers Wind Energy Symposium Proceedings, AIAA*, volume 1301, page 16, 2008.
- [26] Roelend de Breuker. Reader for the course ae4w21 wind turbine aeroelasticity. TU Delft, 2014.
- [27] Theodore Theodorsen. General theory of aerodynamic instability and the mechanism of flutter. 1949.
- [28] Don W Lobitz. Flutter speed predictions for mw-sized wind turbine blades. *Wind Energy Vol*, 7:211–224, 2004.

- [29] R.L. Halfman, H.C. Johnson, and S. Haley. Evaluation of high-angle attack aerodynamic-derivative data and stall-flutter prediction techniques. Technical Report TN 2533, NACA and Massachusetts Institute of Technology, 1951.
- [30] Norizham Abdul Razak, Thomas Andrianne, and Grigorios Dimitriadis. Flutter and stall flutter of a rectangular wing in a wind tunnel. *AIAA journal*, 49(10):2258–2271, 2011.
- [31] JG Leishman and TS Beddoes. A semi-empirical model for dynamic stall. *Journal of the American Helicopter Society*, 34(3):3–17, 1989.
- [32] C.T. Tran and D. Petot. Semi-empirical model for the dynamic stall of airfoils in view of the application to the calculation of responses of a helicopter blade in forward flight. *Vertica*, 5(1):35–53, 1981.
- [33] Andrea Arena, Walter Lacarbonara, and Pier Marzocca. Nonlinear aeroelastic formulation and postflutter analysis of flexible high-aspect-ratio wings. *Journal of Aircraft*, 50(6):1748–1764, nov 2013. doi: 10.2514/1.c032145. URL <http://dx.doi.org/10.2514/1.C032145>.
- [34] Jeremy Beedy, George Barakos, KJ Badcock, and BE Richards. Non-linear analysis of stall flutter based on the onera aerodynamic model. *Aeronautical Journal*, 107(1074):495–510, 2003.
- [35] S Sarkar and H Bijl. Nonlinear aeroelastic behavior of an oscillating airfoil during stall-induced vibration. *Journal of Fluids and Structures*, 24(6):757–777, 2008.
- [36] S Sarkar, JAS Witteveen, A Loeven, and H Bijl. Effect of uncertainty on the bifurcation behavior of pitching airfoil stall flutter. *Journal of Fluids and Structures*, 25(2):304–320, 2009.
- [37] U Galvanetto, J Peiro, and C Chantharasenawong. An assessment of some effects of the nonsmoothness of the leishman–beddoes dynamic stall model on the nonlinear dynamics of a typical aerofoil section. *Journal of Fluids and Structures*, 24(1):151–163, 2008.
- [38] Song Shao, Qinghua Zhu, Chenglin Zhang, and Xianping Ni. Airfoil aeroelastic flutter analysis based on modified leishman-beddoes model at low mach number. *Chinese Journal of Aeronautics*, 24(5):550–557, 2011.
- [39] Xiaoguang Li and Sanford Fleeter. Dynamic stall generated airfoil oscillations including chaotic responses. *AIAA Paper 97*, 1022, 1997.
- [40] Jiunn-Chi Wu, K.R.V Kaza, and L.N. Sankar. Technique for the prediction of airfoil flutter characteristics in separated flow. *Journal of Aircraft*, 26:168–177, 1989.
- [41] Sacha Yabili, Marilyn Smith, and Grigorios Dimitriadis. Unsteady navier–stokes simulation of low-reynolds stall flutter. *AIAA Paper*, 37, 2012.
- [42] EA Dean. Atmospheric effects on the speed of sound. Technical report, DTIC Document, 1979.

- [43] B.E. Thwaites. *Incompressible Aerodynamics*. Cambridge University Press, 1961.
- [44] JC Butcher. A history of runge-kutta methods. *Applied numerical mathematics*, 20(3):247–260, 1996.
- [45] Leonardo Bergami, Mac Gaunaa, , and Joachim Heinz. Indicial response function for finite-thickness airfoils, a semi-empirical approach. In *Conference Proceedings, 49th AIAA Aerospace Sciences Meeting*, pages 1–11, 2011.
- [46] Y.C. Fung. *An Introduction to the Theory of Aeroelasticity*. Courier Dover Publications, 2002. ISBN 0486469360.
- [47] Ricardo Pereira, Gerard Schepers, and Marilena D Pavel. Validation of the beddoes–leishman dynamic stall model for horizontal axis wind turbines using mexico data. *Wind Energy*, 16(2):207–219, 2013.
- [48] Murat Mert. Optimization of semi-empirical parameters in the ffa-beddoes dynamic stall model. *FFA TN*, 37, 1999.
- [49] TJ Berdowski. Investigation of dynamic stall and performance models with emphasis on vawt-design. 2014.
- [50] Davinder Rana, Sandeep Patel, Amit Kumar Onkar, and M Manjuprasad. Time domain simulation of airfoil flutter using fluid structure coupling through fem based cfd solver. 2011.
- [51] Thi Tuyet Nhung Le, Chi-Cong Nguyen, and Hoang Nam Vang. Design of aeroelasticity bench test for naca0012 wing model in the low speed wind tunnel: Influence of wings parameters on flutter speed. 2015.
- [52] D.J. Inman. *Engineering Vibration*. Prentice-Hall, Englewood Cliffs, New Jersey, 1st edition, 1994.
- [53] Hrvoje Jasak. Error analysis and estimation for the finite volume method with applications to fluid flows. 1996.
- [54] Suhas Patankar. *Numerical heat transfer and fluid flow*. CRC Press, 1980.
- [55] Raad I Issa. Solution of the implicitly discretised fluid flow equations by operator-splitting. *Journal of computational physics*, 62(1):40–65, 1986.
- [56] George Keith Batchelor. *An introduction to fluid dynamics*. Cambridge university press, 2000.
- [57] Jean Donea, S Giuliani, and JP Halleux. An arbitrary lagrangian-eulerian finite element method for transient dynamic fluid-structure interactions. *Computer methods in applied mechanics and engineering*, 33(1):689–723, 1982.
- [58] John Charles Butcher. *The numerical analysis of ordinary differential equations: Runge-Kutta and general linear methods*. Wiley-Interscience, 1987.

- [59] Richard Courant, Kurt Friedrichs, and Hans Lewy. Über die partiellen differenzgleichungen der mathematischen physik. *Mathematische Annalen*, 100(1):32–74, 1928.
- [60] Inc. Ansys. Introduction to cfx - transient simulations, 2009.
- [61] Osborne Reynolds. On the dynamical theory of incompressible viscous fluids and the determination of the criterion. *Proceedings of the Royal Society of London*, 56 (336-339):40–45, 1894.
- [62] F.R. Menter. Zonal two equation k-omega turbulence models for aerodynamic flows. *AIAA*, 93-2906, 1993.
- [63] Jacob A Freeman and Christopher J Roy. Verification and validation of reynolds-averaged navier–stokes turbulence models for external flow. *Aerospace Science and Technology*, 32(1):84–93, 2014.
- [64] M Pasandideh-Fard F. Rezaei, E. Roohi. Numerical study comparing rans and les approaches on a circulation control airfoil. In *Conference on Fluid Dynamics, Iran*, 2013.
- [65] Farshad Rezaei, Ehsan Roohi, and Mahmood Pasandideh Fard. Stall simulation of flow around an airfoil using les model and comparison of rans models at low angles of attack. *Hydrology Research*, 2013.
- [66] A. Harhad O. Guerri, K. Bouhadef. Turbulent flow simulation of the nrel s809 airfoil. *Wind Engineering*, 05, 2006.
- [67] Douvi C Eleni, Tsavalos I Athanasios, and Margaris P Dionissios. Evaluation of the turbulence models for the simulation of the flow over a national advisory committee for aeronautics (naca) 0012 airfoil. *Journal of Mechanical Engineering Research*, 4 (3):100–111, 2012.
- [68] Rumsey. The menter shear stress transport turbulence model. URL <http://www.cfd-online.com/Tools/turbulence.php>.
- [69] Herrmann Schlichting, Klaus Gersten, and Klaus Gersten. *Boundary-layer theory*. Springer Science & Business Media, 2000.
- [70] Bram Lof. Openfoam simulations of the xant-21 wind turbine.
- [71] Pointwise. Pointwise - user manual. www.pointwise.org, 14th March 2015.
- [72] Mark J Lutton. Comparison of c-and o-grid generation methods using a naca 0012 airfoil. Technical report, DTIC Document, 1989.
- [73] John W. Slater. Examining spatial (grid) convergence. Online, July 2008. URL <http://www.grc.nasa.gov/WWW/wind/valid/tutorial/spatconv.html>.
- [74] DM Somers. The s819, s820, and s821 airfoils. *Airfoils, Inc*, 1993.
- [75] H. Aagaard Madsen and F. Rasmussen. Prediction of dynamic loads and induced vibrations in stall - stallvib, 1998.

- [76] Anders Melchior Hansen Torben Juul Larsen. How 2 hawc2, the user's manual.
- [77] Jason M Jonkman and Marshall L Buhl Jr. Fast users guide. *Golden, CO: National Renewable Energy Laboratory*, 2005.
- [78] EA Bossanyi. Gh bladed theory manual. *GH & Partners Ltd*, 2003.
- [79] The Menter Shear Stress Transport Turbulence Model, howpublished = <http://turbmodels.larc.nasa.gov/sst.html>, note = Accessed: 2010-01-15.

Appendix A

Classical Flutter Analysis

This Appendix explains the linear method of obtaining the critical classical flutter speed of 2D airfoil. A two-degrees-of-freedom blade section mounted on a heaving- and pitching spring as depicted in Figure 2.10 is considered. Linearisation of the aerodynamic modelling yields:

$$L = qbc \frac{\delta C_l}{\delta \theta} \quad (\text{A.1})$$

$$M = eL \quad (\text{A.2})$$

where q is the dynamic pressure ($q = 0.5\rho U_\infty^2$) and e is the distance from the aerodynamic centre to the rotational centre (rotational centre aft the aerodynamic centre means a positive e). The $\frac{\delta C_l}{\delta \alpha}$ -term indicates the linearised lift-coefficient around $\theta = 0$ which is 2π [rad^{-1}] according to thin airfoil theory. Neglecting structural damping leads to the following equations of motion:

$$m_h \ddot{h} + S \ddot{\theta} + k_h h + qbc \frac{\delta C_l}{\delta \theta} = 0 \quad (\text{A.3})$$

$$S \ddot{h} + I_{rc} \ddot{\theta} + k_\theta \theta - e(qbc \frac{\delta C_l}{\delta \theta}) = 0 \quad (\text{A.4})$$

These set of equations can be solved by assuming solutions of the following form:

$$y = \bar{y} e^{pt} \quad (\text{A.5})$$

$$\theta = \bar{\theta} e^{pt} \quad (\text{A.6})$$

Solving the problems comes down to finding the value for p . If the real part of p is positive, the system is assessed to be unstable and flutter might occur. This is done by rearranging the problem into matrix form:

$$\begin{bmatrix} m_h p^2 + k_h & S p^2 + qbc \frac{\delta C_l}{\delta \theta} \\ S p^2 & I_{rc} p^2 + k_\theta - e(qbc \frac{\delta C_l}{\delta \theta}) \end{bmatrix} \begin{bmatrix} \bar{y} e^{pt} \\ \bar{\theta} e^{pt} \end{bmatrix} = \begin{bmatrix} 0 \\ 0 \end{bmatrix} \quad (\text{A.7})$$

Non-trivial solutions require that the determinant of the coefficient matrix is zero. This leads to the following equation:

$$Ap^4 + Bp^2 + C = 0 \quad (\text{A.8})$$

where

$$A = m_h I_{rc} - S^2 \quad (\text{A.9})$$

$$B = m_h \left[k_\theta - e \left(qbc \frac{\delta C_l}{\delta \theta} \right) \right] + k_h I_{rc} - S \left(qbc \frac{\delta C_l}{\delta \theta} \right) \quad (\text{A.10})$$

$$C = k_h \left[k_\theta - e \left(qbc \frac{\delta C_l}{\delta \theta} \right) \right] \quad (\text{A.11})$$

Now these terms are known, p can be obtained as follows:

$$p = \pm \sqrt{\frac{-B \pm \sqrt{B^2 - 4AC}}{2A}} \quad (\text{A.12})$$

Here A must be positive in order to be physically representative and C is positive when the dynamic pressure q is smaller than the divergence dynamic pressure:

$$q_{div} = \frac{k_\theta}{e bc \frac{\delta C_l}{\delta \theta}} \quad (\text{A.13})$$

As stated in [Dowell et al. \[23\]](#), at dynamic pressures higher than the divergence dynamic pressure, a so-called zero-frequency flutter occurs: divergence. Physically this means that when the critical divergence velocity is reached, the restoring moment of the pitch spring is not able any more to overcome the aerodynamic moment. When divergence has not reached yet ($C > 0$), the following four cases are considered to evaluate the stability of the typical section:

1. $B > 0$ and $B^2 - 4AC > 0$:

The values of p are purely imaginary which is associated to a neutrally stable system.

2. $B > 0$ and $B^2 - 4AC < 0$:

At least one solution of p has a positive real part which is an indication of a dynamic unstable solid and flutter might occur. The flutter boundary is defined as $B^2 - 4AC = 0$.

3. $B < 0$ and $B^2 - 4AC > 0$:

This condition is only reached for relatively very high values of dynamic pressure. In practice, the flutter boundary is reached before $B < 0$.

4. $B < 0$ and $B^2 - 4AC < 0$:

This condition is only reached for relatively very high values of dynamic pressure. In practice, the flutter boundary is reached before $B < 0$.

Analysing Case 2 further, some valuable information concerning the onset of flutter can be extracted. An important characteristic of the flutter boundary criterion is that the static imbalance, $S = ml$, must be positive or zero for flutter to occur. Furthermore, as the distance between the centre of gravity and rotational centre is increased (l increases), the critical flutter velocity, U_{cr} is reduced. This leads to the fact that the mass distribution of an airfoil plays an important role in the onset of flutter. If the rotational centre coincides with the centre of gravity, the onset of flutter can be predicted solely by considering the distance between the aerodynamic centre and rotational centre, e , and the ratio of uncoupled natural heave- and pitch frequencies:

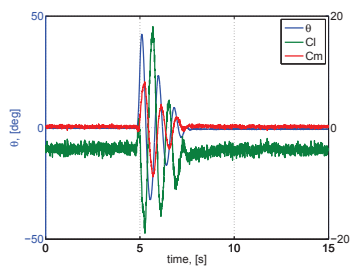
$$\frac{\omega_h}{\omega_\theta} = \frac{\sqrt{k_h/m_h}}{\sqrt{k_\theta/I_{rc}}} \quad (\text{A.14})$$

Flutter will in that case not occur when the following two criteria are met:

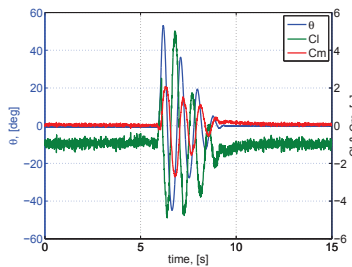
- The aerodynamic centre is ahead of the rotational centre ($e > 0$) and $\frac{\omega_h}{\omega_\theta} > 1$
- The aerodynamic centre is aft the rotational centre ($e < 0$) and $\frac{\omega_h}{\omega_\theta} < 1$

Appendix B

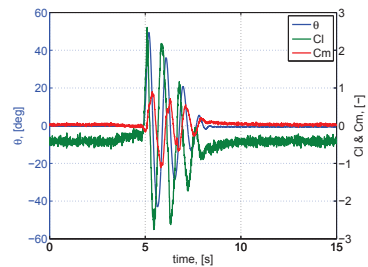
Dynamic Experimental Motion and Force Coefficients for all Wind Speeds from Li [7].



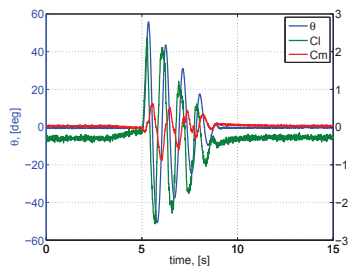
(a) $U_\infty = 1\text{ m/s}$



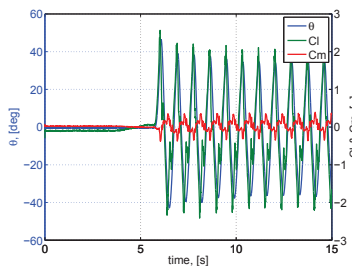
(b) $U_\infty = 2\text{ m/s}$



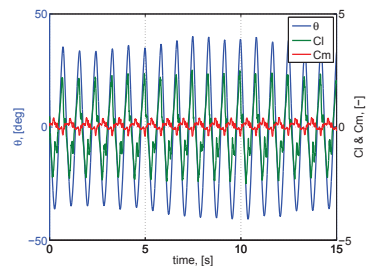
(c) $U_\infty = 3\text{ m/s}$



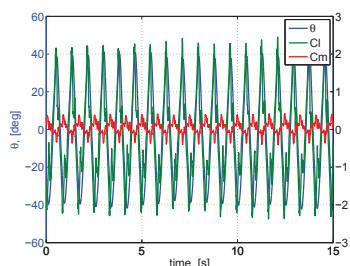
(d) $U_\infty = 3.9\text{ m/s}$



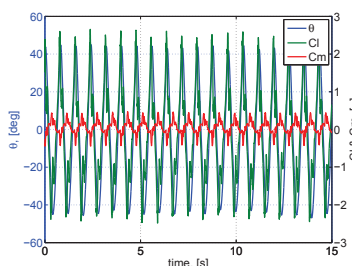
(e) $U_\infty = 9.3\text{ m/s}$



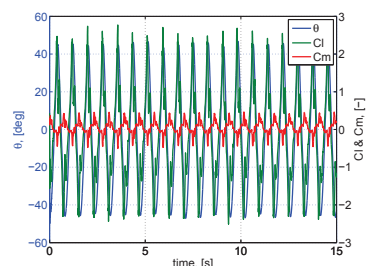
(f) $U_\infty = 9.9\text{ m/s}$



(g) $U_\infty = 11.1\text{ m/s}$



(h) $U_\infty = 12.9\text{ m/s}$



(i) $U_\infty = 14.1\text{ m/s}$

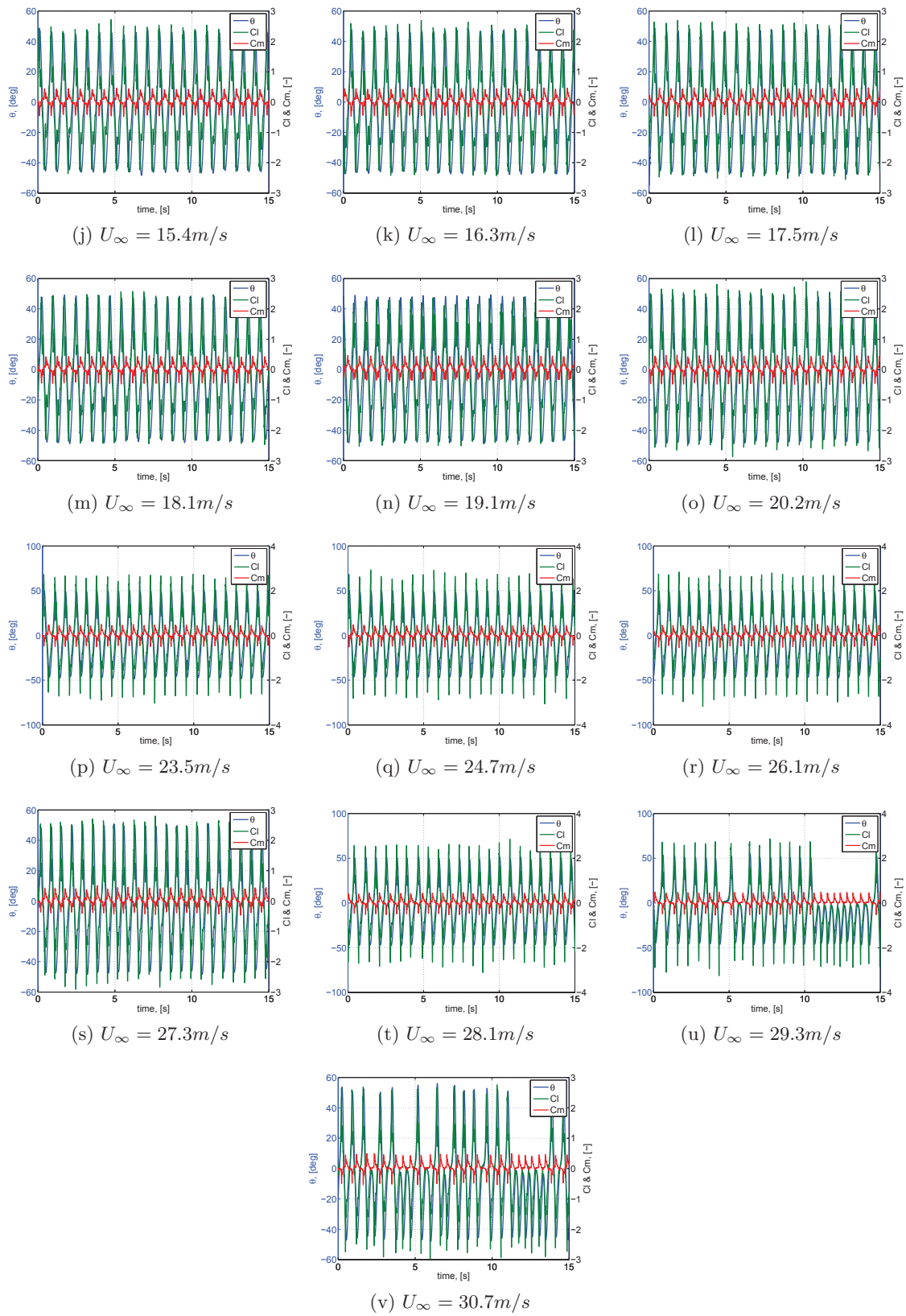


Figure B.1: Pitch Angle and Lift- and Moment Coefficients for all Wind Speeds from Li [7]

Sensitivity Analysis of the Viscous Lag Coefficient.

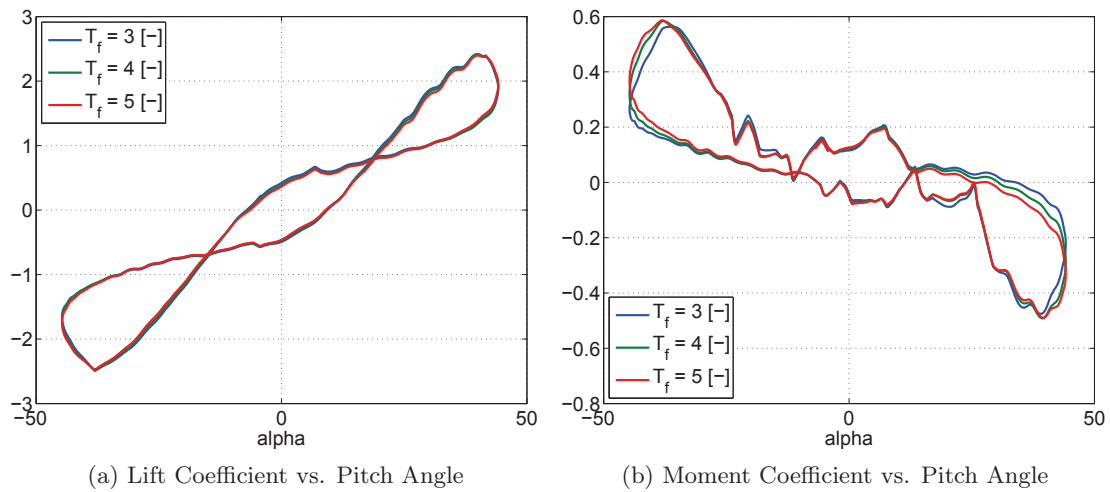


Figure C.1: Sensitivity Analysis of the Viscous Lag Coefficient, T_f , on the prescribed Motion as explained in Section 3.3.

Appendix D

Engineering Model Flowchart.

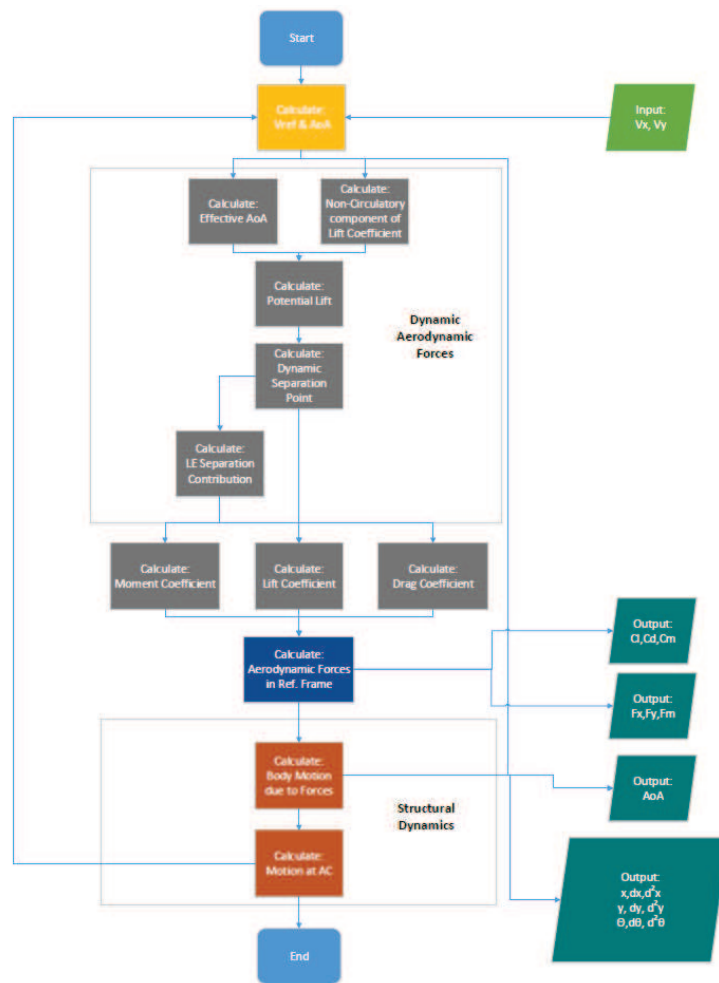


Figure D.1: Flowchart of the Engineering Model

OpenFOAM Algorithms

In this part, the solution methods implemented in the RANS simulations are explained following the formulations from [Jasak \[53\]](#).

E.1 SIMPLE-algorithm

The *Semi Implicit Method for Pressure Linked Equations* (SIMPLE)-algorithm is a method which is used to solve the Navier Stokes equations iteratively in a steady-state problem. The algorithm used in incorporating the SIMPLE loop in the CFD code is given below.

The SIMPLE Algorithm:

1. Set the boundary conditions.
2. Discretize and solve the momentum equation to calculate the velocity field.
3. Calculate the mass fluxes at the cells faces
4. Solve the pressure equation and apply under relaxation.
5. Apply correction to the mass fluxes.
6. Apply correction to the velocity field.
7. Update the boundary conditions.
8. Repeat till convergence.

E.2 PISO-algorithm

The *Pressure Implicit with Splitting of Operators* (PISO)-algorithm is an extension of the SIMPLE-algorithm. The algorithm eliminates the need for iterations, but uses a pressure-velocity coupling calculation procedure. It involves one predictor step and two corrector steps. The algorithm consists of the following steps:

The PISO Algorithm:

1. Set the boundary conditions.
2. Discretize and solve the momentum equation to calculate the velocity field.
3. Calculate the mass fluxes at the cells faces
4. Solve the pressure equation.
5. Apply correction to the mass fluxes at the cell faces.
6. Apply correction to the velocity field with the new pressure field.
7. Update the boundary conditions.
8. Repeat from step 2 till convergence.
9. Increase the time step and repeat from 1.

E.3 PIMPLE-algorithm

The PIMPLE-algorithm uses a hybrid method is the SIMPLE- and PISO-algorithm.

The PIMPLE Algorithm:

1. Set the boundary conditions.
2. Solve the discretized momentum equation to compute an intermediate velocity field.
3. Compute the mass fluxes at the cells faces.
4. Solve the pressure equation and apply under relaxation.
5. Correct the mass fluxes at the cell faces.
6. Correct the velocities on the basis of the new pressure field.
7. Update the boundary conditions.
8. Repeat from step 2 for the prescribed number of times.
9. Increase the time step and repeat from 1.

Appendix F

Parameters of the k - ω SST Turbulence Model

In this Appendix, the variables used in the definitions for the k - ω SST turbulence model, Equation 4.11 and 4.13, are defined. The formulations are taken from [79].

$$P = \tau_{ij} \frac{\partial u_i}{\partial x_j} \quad (\text{F.1})$$

$$\tau_{ij} = \mu_t \left(2S_{ij} - \frac{2}{3} \frac{\partial u_k}{\partial x_k} \delta_{ij} \right) - \frac{2}{3} \rho k \delta_{ij} \quad (\text{F.2})$$

$$S_{ij} = \frac{1}{2} \left(\frac{\partial u_i}{\partial x_j} + \frac{\partial u_j}{\partial x_i} \right) \quad (\text{F.3})$$

The turbulent eddy viscosity is computed from:

$$\mu_t = \frac{\rho a_1 k}{\max(a_1 \omega, \Omega F_2)} \quad (\text{F.4})$$

Each of the constants is a blend of an inner (1) and outer (2) constant, blended via:

$$\phi = F_1 \phi_1 + (1 - F_1) \phi_2 \quad (\text{F.5})$$

where ϕ_1 represents constant 1 and ϕ_2 represents constant 2. Additional functions are given by:

$$F_1 = \tanh(\arg_1^4) \quad (\text{F.6})$$

$$arg_1 = \min \left[\max \left(\frac{\text{sqrt}(k)}{\beta^* \omega d}, \frac{500\nu}{d^2 \omega} \right), \frac{4\rho\sigma_{\omega 2} k}{CD_{k\omega} d^2} \right] \quad (\text{F.7})$$

$$CD_{k\omega} = \max \left(2\rho\sigma_{\omega 2} \frac{1}{\omega} \frac{\partial k}{\partial x_j} \frac{\partial \omega}{\partial x_j}, 10^{-20} \right) \quad (\text{F.8})$$

$$F_2 = \tanh(arg_2^2) \quad (\text{F.9})$$

$$arg_2 = \max \left(2 \frac{\text{sqrt}(k)}{\beta^* \omega d}, \frac{500\nu}{d^2 \omega} \right) \quad (\text{F.10})$$

The constants are defined here:

$$\begin{aligned} \gamma_1 &= \frac{\beta_1}{\beta^*} - \frac{\sigma_{\omega 1} k^2}{\sqrt{\beta^*}} & \gamma_2 &= \frac{\beta_2}{\beta^*} - \frac{\sigma_{\omega 2} k^2}{\sqrt{\beta^*}} \\ \sigma_{k1} &= 0.85 & \sigma_{\omega 1} &= 0.5 & \beta_1 &= 0.075 \\ \sigma_{k2} &= 1.0 & \sigma_{\omega 2} &= 0.856 & \beta_2 &= 0.0828 \\ \beta^* &= 0.09 & k &= 0.41 & a_1 &= 0.31 \end{aligned}$$

Appendix G

RANS Time Step Study Results.

This appendix shows the fields of the several physical quantities involved in the time step study of the RANS simulations at one particular time. The time steps are indicated in the lower left corner of the figures.

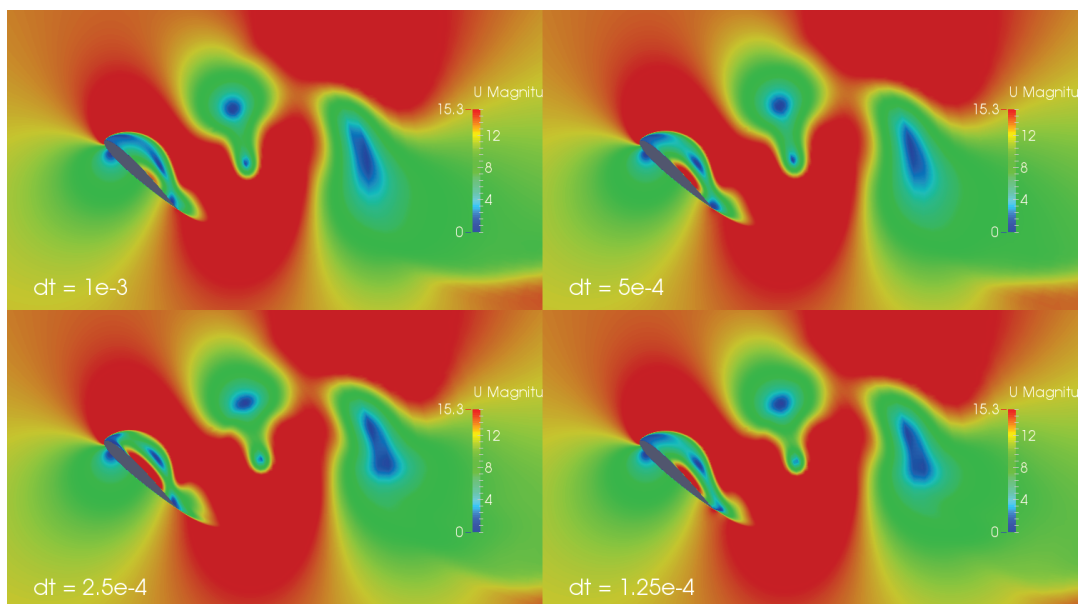


Figure G.1: Instantaneous Time Step Study Results: Velocity, U

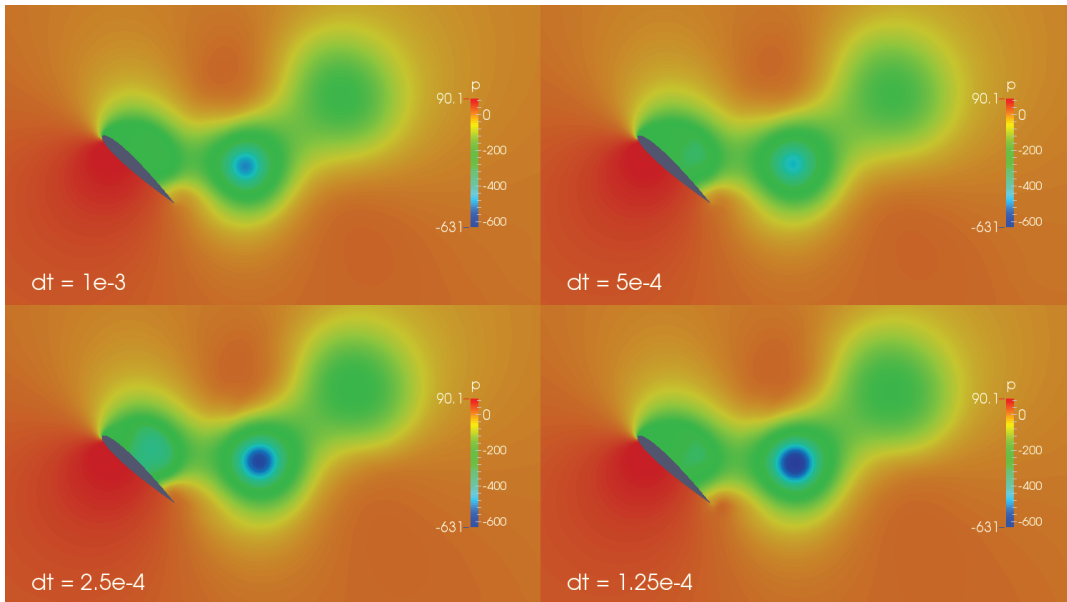


Figure G.2: Instantaneous Time Step Study Results: Pressure, p

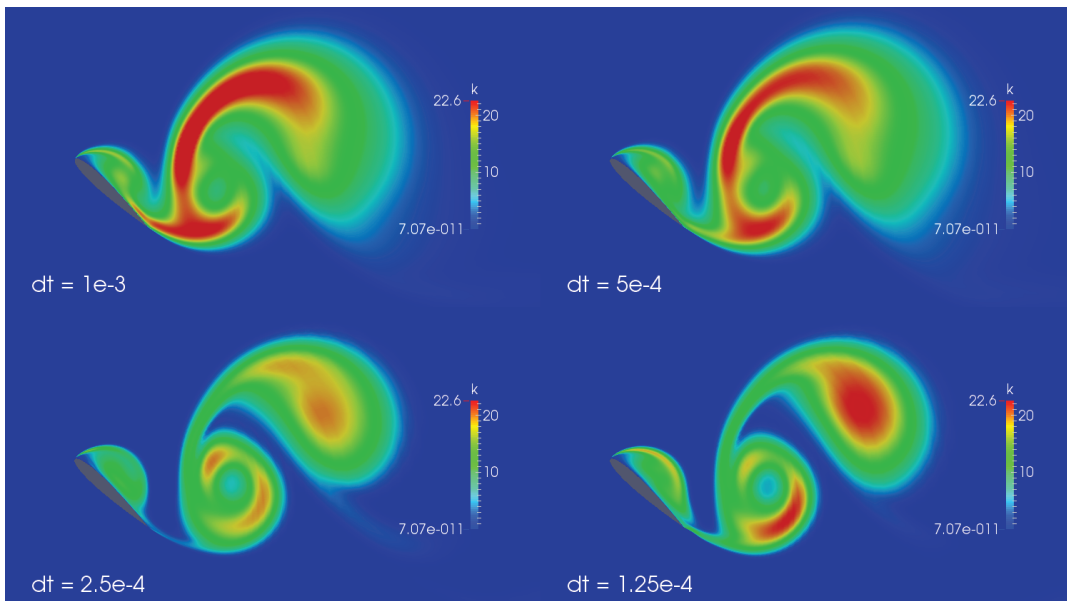


Figure G.3: Instantaneous Time Step Study Results: Turbulent Kinetic Energy, k

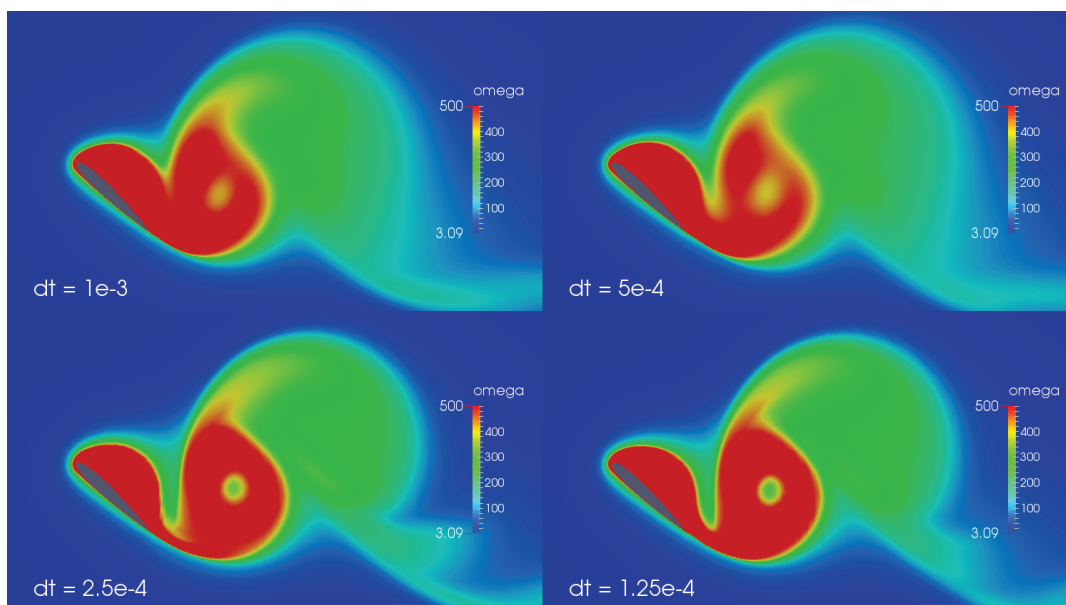


Figure G.4: Instantaneous Time Step Study Results: Turbulent Specific Dissipation, ω

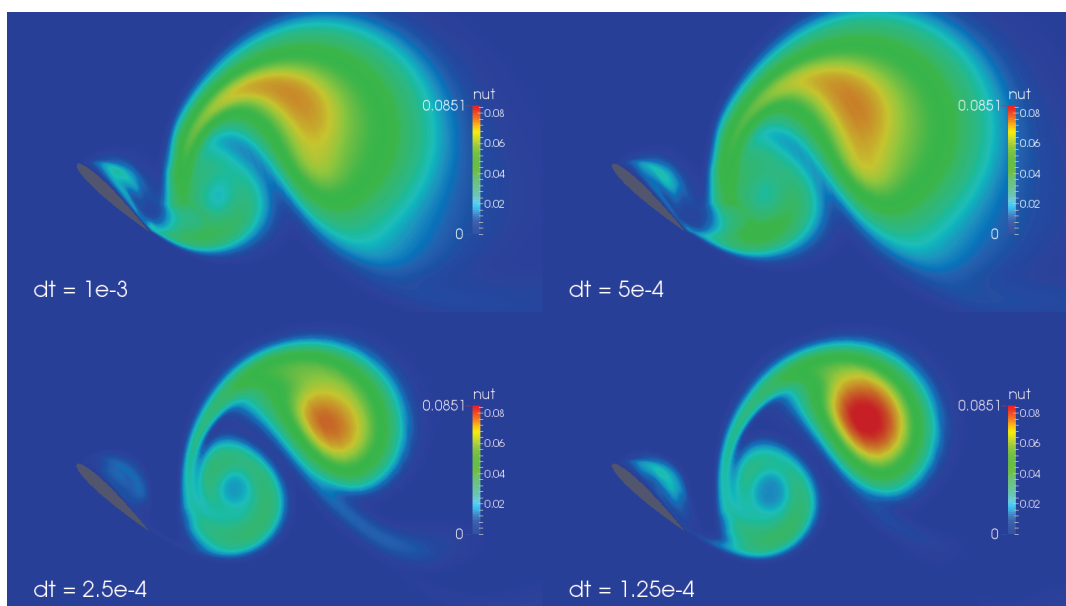


Figure G.5: Instantaneous Time Step Study Results: Turbulence Eddy Viscosity, ν_t

